8-2021

Characterization Techniques and Cation Exchange Membrane for Non-aqueous Redox Flow Battery

Kun Lou
University of Tennessee, Knoxville, klou@vols.utk.edu

To the Graduate Council:

I am submitting herewith a dissertation written by Kun Lou entitled "Characterization Techniques and Cation Exchange Membrane for Non-aqueous Redox Flow Battery." I have examined the final electronic copy of this dissertation for form and content and recommend that it be accepted in partial fulfillment of the requirements for the degree of Doctor of Philosophy, with a major in Energy Science and Engineering.

Thomas A. Zawodzinski, Major Professor

We have read this dissertation and recommend its acceptance:

Jagjit Nanda, David L. Wood, III, Mark Dadmun

Accepted for the Council:

Dixie L. Thompson

Vice Provost and Dean of the Graduate School

(Original signatures are on file with official student records.)

Characterization Techniques and Cation Exchange Membrane for Non-aqueous Redox Flow Battery

A Dissertation Presented for the
Doctor of Philosophy
Degree
The University of Tennessee, Knoxville

Kun Lou
August 2021

ACKNOWLEDGEMENTS

I would like to thank my advisor Dr. Thomas Zawodzinski for providing me the opportunity to conduct research under his guidance. I appreciate that I had the luxury to conduct my research with unbelievably amount of freedom, resources and patience. The non-aqueous science was unexpectedly tough but my experience here was as enjoyable as proton conduction. I am very proud that I am able to graduate from Zgroup with the appreciation of fundamentals and the motivation to explore in-depth science. I want to thank my committee members for their time to advice to make this work better. I appreciate all current and former Zgroup members for their help along the way, especially Gabriel, Ramez, Reed and Jing. Most importantly, although non-aqueous system was proved to be a whole new universe, this work is inspired by Tang's previous work in aqueous system which has been a bible and guideline throughout my research.

I can't thank Energy Storage group at ORNL more for the research capabilities available to me. Nancy, Gabe, Jagjit and all group members have made the group is a top-notch place for energy material research. I want to thank Frank, Robert, Ethan, Amaresh, Yiman and Guang for countless discussions. Also, all the good laughs in 'the office' contributed by whoever stopped by were greatly appreciated!

Everything above would not be possible without the efforts and vision of Bredesen Center, especially Dr. Lee Riedinger. The decision to come to East Tennessee turned out to be a wise one. The mindset of interdisciplinary study can

be seen throughout this work. This journey also would be incomplete without all the help from a lot of people I have worked with in the past. A lot of thanks go to Dr. Jonathan Lovell, Dr. Dong Zhang, Dr. Jijun Qiu, Dr. Fuwei Zhuge and more.

I want to thank my family for the support throughout my whole life and their belief that education makes a difference. I am happy this work is something they are proud of.

ABSTRACT

The motivation of this work comes from one of the major problems of emerging non-aqueous flow battery (NAFB) that a separator or membrane which facilitates conductivity and blocks redox species crossover does not exist. Although many aspects of principles can be mirrored from mature fuel cell and aqueous flow battery, it is found that some well-defined membrane properties in aqueous systems such as swelling, transport and interactions are different in non-aqueous solvents to some extent. However, the approach of this work does follow the way perfluorosulfonate ion exchange membrane (PFSA) facilitated development of fuel cell and aqueous flow battery in the past. The aim of the work is not to identify or suggest one or one type of membrane that fits the non-aqueous flow battery. This is quite impossible based on the extremely diverse scope of published non-aqueous redox species. Thus, effort to understand and establish fundamentals of transport and interactions within membrane is the goal of the work to bridge the polymer design/synthesis and practical flow battery development is the goal of this work.

The highlight of this work includes observation of high ionic conductivity of tetraalkylammonium form PFSA of high organic solvent swelling as well as, solvation and interactions among the cation, organic solvent and membrane, low swelling but high ionic conductivity of asymmetric organic cation as a charge carrier for non-aqueous flow battery from an interaction perspective.

In terms of techniques, advanced Fourier-transform infrared spectroscopy (FTIR) and Nuclear Magnetic Resonance (NMR) methods beyond simple material characterization are designed in order to probe interactions and solvation. Although the methodologies involved here have long been used to study aqueous or non-aqueous electrolytes dating back to the 50s and 60s, this work aims to push these methods to another level inside of the membrane, a non-homogeneous and non-aqueous environment. Local information is separated from bulk property to understand transport dynamics and reveal membrane properties.

TABLE OF CONTENTS

LIST OF TABLES

LIST OF FIGURES

CHAPTER 1 INTRODUCTION

1.1 BACKGROUND

We have been witnessing the successful industrialization of many renewable energy technologies during the past decade, headlined by solar and wind. While we enjoy these technologies coming to fruition from decades of research, they are still tagged as an intermittent source of energy to compete with fossil fuel. To date, flow battery is regarded as one of the most promising energy storage technologies to capture intermittent wind and solar energy for stable storage and reliable output[1]. This technology has a key feature by allowing power and energy of redox flow battery to be scaled up or down independently by as 'decoupling' these two aspects.[2–10]. Figure 1.1 is an illustration diagram of a typical vanadium flow battery. The power of the system can be tuned by changing the electrode size and the amount of redox species (in a tank) determines the energy capacity[11].

The pioneering work on flow batteries was done in the 70s when NASA developed the first of idea of a flow cell using Fe^{2+}/Fe^{3+} and Cr^{2+}/Cr^{3+} pairs[12]. New development has since followed based on variations of redox material, solvent system and cell architecture. The majority of these efforts are still on-going because each of the suggested approaches involve various trade-offs compared to all-vanadium flow battery. The all-vanadium flow battery as of today still remains the state-of-art configuration of flow battery and has been commercialized worldwide[13].

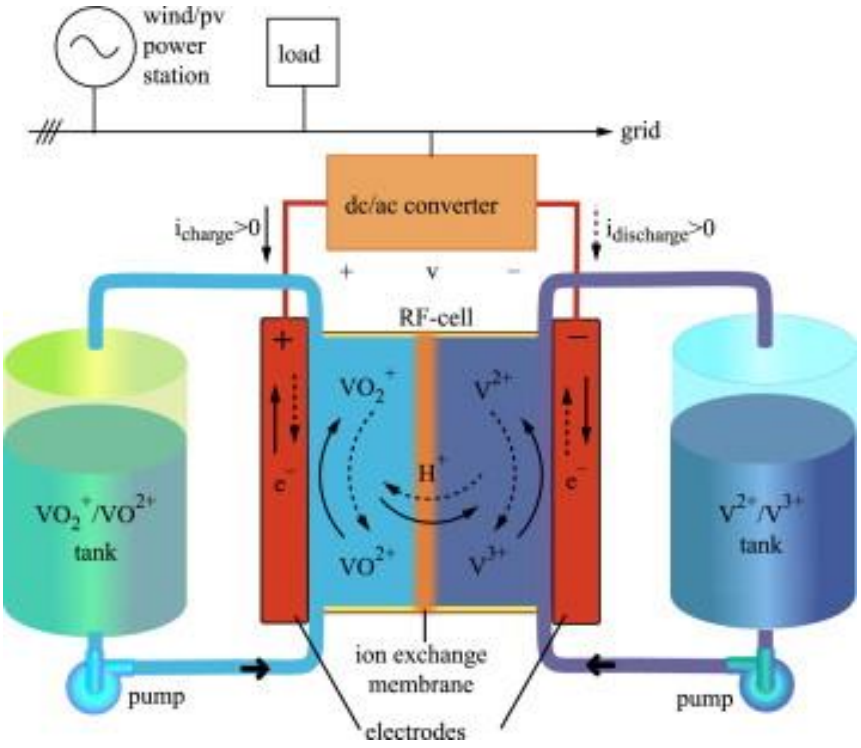

Figure 1. 1 Schematic of a vanadium redox flow battery[14]

Catholyte and anolyte solutions are stored separately and are pumped into the cell past the electrode. Catholyte refers to an electrolyte containing specified redox molecules at oxidized state and are to be reduced during the discharge process or at reduced state and to be oxidized during the charging process[15] while the 'anolyte' is the reverse. During a typical discharging process, catholyte and anolyte undergo the following electrochemical half reactions:

$$\text{Anolyte}^{n} - e^{-} \rightarrow \text{Anolyte}^{n+1} \quad (1.1)$$

$$\text{Catholyte}^{n+1} + e^{-} \rightarrow \text{Catholyte}^{n} \quad (1.2)$$

A membrane or separator is sandwiched between catholyte and anolyte to provide electrical insulation and ideally limit the ability of redox couples (anolyte and catholyte) at all states of charge to reach the opposite compartment while allowing non-reactive ions transport to balance the charge to maintain electroneutrality and electrolyte balance.[11,16]. These two functions are closely related to the permeability and conductivity which will be extensively studied in this work. Other important figures of merit regarding flow battery performance are voltage efficiency (η_V), coulombic efficiency (η_C), energy efficiency (η_E) and power efficiency (η_P):

$$\eta_V = \frac{V_{discharge}}{V_{charge}} \quad (1.3)$$

$$\eta_C = \frac{Q_{discharge}}{Q_{charge}} \quad (1.4)$$

$$\eta_E = \frac{E_{discharge}}{E_{charge}} \quad (1.5)$$

$$\eta_P = \frac{IV_{discharge}}{IV_{charge}} \quad (1.6)$$

Where I is current, $V(Q, E)_{discharge}$ and $V(Q, E)_{charge}$ are discharge and charge voltage, charge and energy of a cell operated at a certain state of charge[11]. When same current is applied in both charging and discharging process, the coulombic efficiency equals to the ratio between discharge time and charge time[17].

A decrease in ionic conductivity correspondingly decreases voltage efficiency, whereas increase of redox species permeability compromises coulombic efficiency. Although it is desired that zero redox species cross the membrane during operation, leading to maximum coulombic efficiency, it remains to be seen if such a scenario is possible without sacrificing ionic conductivity[18]. Self-discharge induced by active species' undesired crossover is one major obstacle in flow battery development. While all-vanadium flow battery might get away with cross-contamination by deploying a symmetric (vanadium species on both sides) setup, other aqueous and non-aqueous systems that have asymmetric setup must face irreversible contamination in addition to capacity decay.

The emerging non-aqueous flow battery, however, does have some advantages over its aqueous counterpart. The energy density of an aqueous battery is limited by the electrochemical window of water (~1.5V). Many organic solvents naturally bear a wider voltage window, allowing higher voltage cells. Another important aspect of energy density is the concentration of active species. The solubility of organic species in non-aqueous solvents, in theory, can surpass that of vanadium species in water (~2M). However, most existing redox couples for non-aqueous flow batteries are limited in solubility. Even though solubility issues can be solved with emerging synthesis efforts, the resulting high

viscosity and modest conductivity of non-aqueous electrolyte remains a huge drawback. Another disadvantage with the non-aqueous system is the cost of organic materials compared to aqueous-based flow battery. However, from a techno-economic perspective, the non-aqueous system is surprisingly projected to cost equivalently compared to aqueous system. The trade-offs on the non-aqueous side are between high voltage window and low current densities[19,20].

The most underdeveloped part of non-aqueous battery is probably the membrane/separator. The majority of research today focus on exploring or synthesizing new redox couples. Even though proof of concept remains the primary goal, significant species crossover even under limited cycle numbers is observed[21]. A recent membrane screening study has indicated that the existing membranes are unable to serve the emerging technology[22]. The first and foremost problem associated with moving from aqueous to non-aqueous is stability (chemical and mechanical). For the classic aqueous-based vanadium flow battery, sulfuric acid is considered as the major threat against chemical stability. Typically, fluorination is the answer to strong acid compared to some hydrocarbon-based membranes. Since membranes designed exclusively for non-aqueous system is glaringly lacking[23], most membranes utilized today have been designed for aqueous system but will have to stand against attack from organic molecules. Although it is not within the scope of this work, it is important to note that poor resistance against some common organic solvent such as ACN and propylene carbonate at room or elevated (< 100 °C) temperature has been noticed with both fluorinated and hydrocarbon membranes in this study. Anion exchange membranes (AEMs) also have

been reported to have chemical stability issue and low conductivity in non-aqueous environment[17]. On the other hand, perfluorinated cation exchange membrane such as Nafion have been tested and are stable in a variety of organic solvents[24,25]. To keep the research focus on transport and interaction, most of the data presented here are acquired with a commercial PFSA from 3M, 825 equivalent weight.

Although in-depth investigation of PFSAs used in a non-aqueous environment has been lacking, the development of proton dynamics in PFSA combined with the understanding of solvation in organic solvents provides some guidance. In this work, we combine the knowledge from these two fields and manipulate parameters to probe the PFSA in non-aqueous environment for NAFB.

(1) While the proton conducting has been a default dynamics mode studied in previous aqueous-based systems, various organic cations are introduced to PFSA in light of transport in non-aqueous media. In fact, we show that the cation type is a useful parameter that dictates membrane properties in density, conductivity and interactions, to be discussed in detail throughout this work.

(2) Taking the dielectric and transport properties into consideration, we have selected ACN and PC as model solvents. They represent the volatile and non-volatile solvents, respectively. This consideration also plays an important role behind some novel experimental designs that are presented in this work. These two solvents are ‘spectroscopy friendly’ molecules that provide some surprising advantages over water in terms of observability.

(3) In addition to the chemical nature of the non-aqueous system that differs from the aqueous one, the transport phenomena at low solvent content are given much emphasis in various characterization techniques to probe the cation and solvent dynamics.

Overall, this work has been inspired by the lack of a benchmark membrane for NAFB and aims to contribute to the fundamental understanding of membrane behavior in non-aqueous media that can lead to advanced designs of such membranes.

1.2 MOTIVATION

1.2.1 Lack of fundamental understanding of transport in non-aqueous system

There is a need to probe membrane properties in non-aqueous system beyond conductivity values. Such studies undoubtedly can benefit membrane design strategy and synthesis. The current status of membrane development for non-aqueous flow battery is that we do not have a membrane and yet we do not know what specific scientific parameters are desired other than general descriptions such as ‘high conductivity’ and ‘low permeability’. Questions such as what parameters contribute to ‘non-aqueous’ conductivity? How is transport within the membrane in non-aqueous solvent differ from aqueous system? Is there any existing membrane can be used as a ‘plug and play’ component in a non-aqueous system without sophisticated modification? should be addressed. There is an absolute necessity to have a deeper understanding of membranes in non-aqueous system. So far, unfortunately, previous experience with aqueous system represents the best knowledge in this matter. Early experiments in this work observed high swelling of organic solvent with tetraalkylammonium as membrane cation. To date,

classic water swelling data is still being borrowed and assumed to reflect non-aqueous solvent uptake behavior[26,27].

1.2.2 To develop membrane characterization methodology in non-aqueous solvent.

One of practical experimental difficulties throughout this work has been 'dehydration'. It is well known that the proton ionic conductivity of PFSA can be as high as 0.1 S/cm in water[28]. Thus, even a trace of water trapped in the hygroscopic membrane can give an artificial boost in conductivity. One of the common characteristics of some organic solvent is high volatility compared to water. This is especially troublesome in measuring solvent uptake, swelling and conductivity which are simplest means of characterization for membrane with aqueous system. Non-invasive characterization methods are required. The success story of aqueous vanadium flow battery and fuel cells definitely benefit from the ultrafast kinetics in aqueous system. However, this might be a problem for spectroscopy enthusiasts since the proton exchange is too fast to track at room temperature. The non-aqueous characteristic opens up opportunities to discern chemical information within the system to allow advanced characterizations, especially since fast exchanging protons are generally not used.

1.2.3 Permeability is key.

Although conductivity is generally more important in terms of membrane evaluation, the natural disadvantage of comparably slow transport in organic solvent is inevitable. However, the crossover can be deadly to non-aqueous flow battery system in terms of capacity decay. Although it is well-known that selectivity is crucial to prevent

crossover, porous separators are currently widely employed. The reason of this choice is very complicated and is associated with other components of the battery system. First of all, the conductivity in non-aqueous system is too low, both in the electrolyte AND within membrane. Thus, to demonstrate a proof-of-concept redox species without unreasonably high resistance, a porous separator is preferred. This is also the very same reason behind low redox species concentration in flow battery demonstrations as a sufficient supporting electrolyte concentration has to be prioritized to ensure decent electrolyte conductivity. The side effect, however, is that membrane with limited or no ion exchange capability have been proved to have extremely serious crossover issue. This greatly hinders the current development of non-aqueous flow battery[29–31]. The second reason comes from the 'size-exclusion' strategy in membrane development. Focus has been put on the size of active species versus pore size of the membrane. Although careful engineering efforts have been made to improve selectivity of the membrane, the sophistication leads to high cost, making it economically unfavorable and nearly impossible to scale up. The size-exclusion methodology also limits the development of redox materials. Unless there is an organic version of 'vanadium', membranes with various pore size have to be developed to meet the demands. From a transport perspective, size-exclusion also applies to solvent molecules. It is very likely that the solvent transport could also be limited and this usually correlates to poor ion transport. This makes the size-exclusion membrane fall into the conductivity-permeation trade-off again.

THIS THESIS IS BASED ON THE HYPOTHESIS THAT THE KEY ELEMENTS TO understand in DEVELOPING A HIGH PERFORMANCE MEMBRANE FOR NAFB based on a PFSA-type ion exchange membrane include:

1. In Chapter 2, we introduce the Cation typ. The cation-sulfonate interaction is presented in Chapter 2 and Chapter 3.

2. The role of solvent in dissociation of cation from the sulfonate site is investigated in Chapter 3.

3. In Chapter 4 and Chapter 5, we investigate the role of solvent in promoting intermediate range transport from the site.

4. Any changes in morphology or other polymer behavior induced by the cation are covered in Chapter 2.

5. The discussion in Chapter 6 focuses on the role of the cation and polymer in controlling uptake of solvent and redox active species, and thereby permeation of the redox active species.

These elements are systematically investigated in the thesis.

CHAPTER 2 WHY DOES TETRAALKYLAMMONIUM ION MOVE FASTER THAN LITHIUM ION?

In-depth understanding of membrane behavior when swollen with a non-aqueous solvent is necessary to facilitate membrane design for a non-aqueous flow battery. In this work, tetraalkylammonium form perfluorinated sulfonic acid (PFSA) membranes are studied and found to have acceptably high ionic conductivity/diffusion with a maximum of 18.1 mS/cm for tetrabutylammonium form membrane in acetonitrile (ACN). We find that the size of cation incorporated into PFSA is related to the membrane density/porosity which leads to difference in swelling and conductivity. Cation dissociation and solvation within PFSA in ACN are elucidated by FTIR to explain a surprising inverse relationship between cation size and conductivity. We reveal that by using cation as a variable parameter, we can induce significant membrane swelling which leads to higher mobility.

2.1 INTRODUCTION

The emerging non-aqueous flow battery (NAFB) inherits the versatility of decoupling independently scalable energy content and power output from its aqueous counterpart[32]. Most NAFB research in recent years aim at organic redox species for higher solubility and wider potential window[33] from an energy density perspective. However, the high cell resistance poses as a major scientific[34] and economic[20] bottleneck to overcome. Current conductance values (on the order of mS/cm or less) makes it impossible to practically implement NAFB[34]. Among all battery parts that contribute to the overall cell resistance, the membrane is usually found to constitute most of it by comparing the cell area specific resistance (ASR) and equivalent ASR of the membrane[35]. While many published NAFB

works have been calling for better membranes, in reality, a membrane design strategy dedicated to NAFB does not exist, let alone a success story in finding the 'Nafion' for NAFB. The fundamental understanding of membrane in non-aqueous system is obviously lacking. The diversity of NAFB chemistries today adds more significance to the fact that a bottom-up understanding of fundamentals is more favorable than screening membranes for one certain redox system. In fact, Nafion or PFSA remains one of the few familiarities as we transition from fuel cell/vanadium flow battery to NAFB as the transport-structure relationship of PFSA in aqueous system has been well-documented[36–39]. In NAFB, wider voltage window is potentially a greater threat to non-fluorinated membrane while commercial anion exchange membrane (AEM) has lower ionic conductivity in non-aqueous system[17] and porous separators are not ideal candidates due to the lack of ion-selectivity[40]. Thus, the PFSA was chosen as the target membrane in this work. As for the solvent, acetonitrile (ACN) is used because (1) ACN has been the most utilized solvent for NAFB to date, (2) We envision the aprotic ACN will allow acceptable conductivity due to its superior viscosity (0.34 cP) and solubility of redox active species/supporting electrolyte[41], (3) ACN is a simple molecule for spectroscopy study, (4) To benchmark membrane characterization with volatile organic solvent and (5) We can build from the abundance of in published fundamental work regarding dynamics, transport and solvation.

Previous studies of PFSA membrane behavior in non-aqueous solvents focused on selection of organic solvent[24,42] , conducting alkali cations[24,25,43–45], selectivity[45] and structure change[46]. Interestingly, there was no direct correlation observed between conductivity of the classic Li^+ form Nafion 117 and a single bulk solvent property (solvent

type, viscosity and dielectric properties)[25]. By switching counterions (metallic cations), it was found that alkali ions can yield at most a ~15% difference in swelling[43]. Given the total arrangement of ion size and surface charge, organic cations might behave differently. Since tetraethylammonium (TEA^+) /tetrabutylammonium (TBA^+) salts are common supporting electrolytes in nonaqueous electrochemistry in general and in some work in NAFB[26,47,48], we report a systematic study of PFSA membranes using tetraalkylammonium cations as charge carrier. In this work, interactions among cations, membrane (sulfonate group) and solvent (ACN) are presented in addition to bulk properties. Our results not only showed promising non-aqueous ionic conductivity value but also some interesting ways by which organic cations affect the membrane performance. Organic cations were found to induce morphology changes, which in turn affect uptake and ionic conductivity. We aim to benchmark this organic cation effect which has not been reported in aqueous system. The cation effect we found opens up a new membrane design strategy for low cell resistance NAFB by taking the cation selection into consideration.

2.2 EXPERIMENT AND METHODS

2.2.1 Membrane pretreatment

Membranes with an equivalent weight of 825 (3M Ionomer) provided by 3M were pretreated following our previous work[28,49]. The as-received membranes were treated at 85°C for an hour in 3% hydrogen peroxide (Fisher Scientific), followed by deionized water (DI) (Milli Q, 18.2MΩ/cm), 1M sulfuric acid (Alfa Aesar) and DI water. Membranes were exchanged to tetramethylammonium (TMA^+), tetraethylammonium (TEA^+),

tetrabutylammonium (TBA^+) or Li^+ form by being soaked in the respective hydroxide solutions (1 M for organic species, 0.1 M for lithium hydroxide, Sigma). The ion exchange efficiency confirmed by NMR and ICP in our previous work was > 98%[50]. Membranes were then dried over phosphorus pentoxide (P_2O_5) for at least 14 days prior to experiments.

2.2.2 Membrane conductivity measurement

Membrane resistance was measured with a typical four-point Teflon conductivity cell soaked in ACN with a Bio-logic SP200 potentiostat from 200 KHz to 1 HZ in the Argon-filled glove box. The high frequency intercept of the Nyquist plot was taken to calculate the ionic conductivity.

$$\Sigma = \frac{L_e}{RW\alpha} \qquad (2.1)$$

R is the resistance value read from high frequency intercept with the real impedance between two sensing electrodes separated by a distance of L_e. W and α are membrane width and thickness swollen in ACN derived from swelling measurement above based on dry width and thickness measured beforehand. Conductivity measurements in water were done following our previous reported method[28].

2.2.3 Membrane diffusion coefficient measurement

Dry membrane (> 50 mg) was inserted into a 5 mm NMR tube in the glove box. Deuterated ACN (99.8 atom %, Sigma) was added to ensure the membrane was completely immersed. The sample was taken to a Varian 500 NMR spectrometer with a

60 G/cm gradient coil after 3 days of equilibrium. A DOSY bipolar pulse pair stimulated echo pulse sequence was selected to measure the ^{1}H diffusion coefficient of the organic cations. The pulse-field-gradient (PFG) measurement of molecular translational motion involves two gradient pulses. The first one diphase the magnetization, followed by a delay Δ, then the magnetization is refocused. Because of molecular motion between two gradient pulses, we will not be able to restore the (random) phases of the transverse magnetization and a reduced signal intensity is observed due to the average molecular displacement. The distribution of the displacement can be described as a Gaussian function to represent the diffusion process[51]. The data is fit exponentially into Stejskal-Tanner equation[52,53] (Equation 2.2) to derive D, diffusion coefficient,

$$I = I_0 * e^{-D(\gamma g \delta)^2\left(\Delta - \frac{\delta}{3}\right)} \quad (2.2)$$

Where I is relative signal strength, I_0 is the corresponding strength without gradient, γ is the gyromagnetic ratio of nucleus, g is the gradient strength and Δ is the diffusion delay described above.

2.2.4 Membrane swelling and uptake measurement.

The widths and thickness of dry membrane were measured by a Fisher Scientific digital caliper and a Mitutoyo micrometer. ACN swollen membranes were sandwiched between two transparent glass slides and excess ACN was injected between glass slides to keep membranes fully soaked. Widths of swollen membranes were quickly measured through transparent glass slides by the caliper. For the swollen thickness, membranes were soaked in ACN in a flat glass dish. A micrometer probe is positioned in perpendicular

to the membrane to measure the swollen membrane thickness. All values were averaged from five readings. Swelling volumetric expansion was calculated by:

$$x = \frac{W_s L_s \alpha_s - W_{dry} L_{dry} \alpha_{\mathrm{dry}}}{W_{dry} L_{dry} \alpha_{\mathrm{dry}}} \times 100\% \quad (2.3)$$

W_{dry}, L_{dry} are dry membrane width and length. α_{dry} is dry membrane thickness. W_s, L_s and α_s are corresponding ACN swollen membrane width, length and thickness.

For ACN uptake, the dry membrane was weighed in the glove box and then soaked in ACN for at least three days. The equilibrated membrane was taken out of the ACN solution, quickly blotted and weighed. Similar to water uptake, ACN uptake, λ, is defined as molecular ratio of ACN to cation within the membrane.

$$\lambda = \frac{(m_{wet} - m_{dry}) \times \mathrm{EW}}{m_{dry} \times \mathrm{M}_{ACN}} \quad (2.4)$$

$$\mathrm{EW} = 825 - \mathrm{M_H} + \mathrm{M}_{Cation} \quad (2.5)$$

Where m_{wet} and m_{dry} are wet and dry mass of membrane and M_{ACN} is molecular weight of ACN. EW is the adjusted equivalent weight of membrane from original EW of proton form based on the molecular weight of H and cation, M_H and M_{Cation}, respectively.

2.2.5 Membrane density measurement

Density was measured by AccuPyc 1340 pycnometers at room temperature. The membrane was quickly packed into a 1 cm^3 sample cup and be loaded into the instrument. Helium gas was brought into the sample chamber until a certain pressure is reached. The

gas was then released, and the pressure was measured. Boyle's Law was applied to calculate the relationship between volume and gas pressure[53].

2.2.6 Membrane FTIR measurement

Attenuated total reflection (ATR) data were recorded on an Agilent Cary 600. At least 128 scans from 400 to 4000 cm^{-1} with a resolution of 2 cm^{-1} chosen. For dry membrane measurement, a piece of 0.5 cm x 0.5 cm polymer was pressed onto the IR crystal within a sealable cell in the glove box. For membrane + ACN measurements, the membrane was pre-equilibrated in ACN for at least three days before loaded in the cell. Extra ACN was injected into the cell to mimic the situation where the membrane is soaked in ACN.

2.2.7 SAXS experiment

Small-angle X-ray Scattering (SAXS) data was acquired at the Center for Nanophase Materials Sciences (CNMS) in Oak Ridge National Laboratory on an Anton Paar SAXSess mc^2. The scattered beam was recorded on a CCD detector (PI-SCX, Roper) with a pixel resolution of 2084 × 2084 and pixel dimensions of 24 × 24 μm^2. The data collection time was 20 min. For the measurements, X-rays were generated at 40 kV/50 mA at a beam wavelength of λ = 1.541 Å (Cu Kα radiation). The generated X-ray beam was slit-collimated using Kratky camera giving rise to a beam size of 18 mm (length) × 0.4 mm (width), and the collected SAXS data were desmeared and expressed as intensity versus q, after subtraction of detector dark current and background scattering. Here $q = (4\pi \sin \theta)/\lambda$ with θ and λ being the half of the scattering angle and X-ray beam wavelength, respectively.

2.3 RESULTS AND DISCUSSION

2.3.1 Ionic conductivity and diffusion

Ionic conductivity values from this work and literatures were listed in Table 2.1. In a previous report[26], both TMA^+ and TBA^+ form Nafion 1035 showed higher ionic conductivity than lithium but note that the membrane was equilibrated in vapor phase saturated ACN. In the similar case of Nafion equilibrated in vapor phase, proton conductivity was always lower than that of membrane equilibrated in liquid water although in theory water content under vapor phase of RH=100% could eventually match 100% water uptake value[54–56]. To our best knowledge, the ionic conductivity of membrane equilibrated in ACN vapor for a week is roughly an order of magnitude lower than membrane being swollen in ACN. Thus, to mimic a real working environment in a flow battery, conductivity tests were carried out with membrane soaked in the solvent in this work. We did observe that the ionic conductivity of tetraalkylammonium form membrane was higher than that of the lithium form membrane. The surprise came as ascending ionic conductivity from the smallest cation, TMA, to largest, TBA. as the radius (r) of cations are r (TBA^+) = 0.415 nm, r (TEA^+) =0.343 nm, r (TMA^+) =0.283 nm and r (Li^+) =0.076 nm[57], respectively. Although it was reported that the conductivity of tetraalkylammonium salts in ACN can be higher than lithium salts, the conductivity pattern observed in this work is truly surprising, especially in light of the findings of Moore and co-workers in which the large cations appeared to strongly ion pair and ‘cloak’ the sulfonates in aqueous systems. The highest conductivity value of 18.1 mS/cm from TBA^+ form membrane not only was over an order of magnitude higher than that for Li^+ form but it also surpassed the suggested ionic

conductivity of 7.7 mS/cm for a non-aqueous flow battery electrolyte set by a previous report[45] which is crucial to make NAFB viable to compete other means of energy storage technology.

This interesting finding was confirmed by diffusion coefficient measurement by pulse-field-gradient (PFG) NMR method. PFG-NMR has been a developed technique to investigate water diffusivity through Nafion[58]. The diffusion coefficient is a measure of molecular displacement or translational motion[59]. A proton exchange membrane with a 10^{-1} S/cm conductivity and 1 M proton concentration yields a proton diffusion coefficient on the order of 3×10^{-5} cm^2/S, compared to a 10^{-4} cm^2/S diffusion coefficient of proton in water[39].

Thanks to the fluorinated nature of PFSA, protons from tetraalkylammonium cations within membrane are the only proton source and can be easily used to measure ionic diffusion coefficient (Figure 2.1). This feature was an improvement from studying PFSA in aqueous system where the proton mobility was an average of cation (proton) and solvent (water). All primary, secondary and tertiary protons from respective tetraalkylammonium cations are clearly resolved. Thus, PFG-NMR is a much more powerful tool to serve fundamental studies in NAFB than aqueous system. The diffusion coefficient of TMA^+, TEA^+ and TBA^+ are 2.38×10^{-11}, 3.33×10^{-10} and 3.54×10^{-10} m^2/S, respectively (Table 2.1). This agrees with the trend of ionic conductivity data measured by impedance that $\Sigma(TBA^+) > \Sigma(TEA^+) > \Sigma(TMA^+)$. Apart from diffusion information, PFG-NMR helps to eliminate ‘artificial boost’ in conductivity/diffusion due to water existence.

Barring any proton from residual water, protons of a molecule should have same diffusion properties.

Ion diffusion in non-aqueous media is naturally a slower process compared to Grotthus hopping, which is based on the hydrogen bonding in aqueous system[58]. Given that bulky tetraalkylammonium cations have extremely low aqueous ionic conductivity (Table 2.1) and ionic conductivity of alkali cations of Nafion 117 have been proved to decrease with increasing ion size in organic solvents[25] and water[60], it would be hard to expect that these alkyl ammonium cations somehow overcome size disadvantage in non-aqueous environment.

However, the underlying part of cation transport within PFSA is the prerequisite that the cation is dissociated from the fixed sulfonate group. The dissociation of Li^+ from sulfonate group (Nafion) in non-aqueous systems was studied in terms of conductivity measurements[24] and simulation[61]. In this work, not only is the study of the interaction between cation and membrane extended to tetraalkylammonium, the interaction under the existence of organic solvent (ACN) is also investigated in the context of emerging NAFB.

2.3.2 Vibrational study

The interaction between cations and sulfonate group of PFSA can be characterized by looking at the S-O stretching peak of dry PFSA exchanged with different cations[60]. Li^+ and other alkali cations bind tightly to sulfonate group, exerting a strong polarization effect on the S-O bond[61]. This leads to the frequency of the S-O stretching shifting to higher

wavenumber (δ) as shown in Figure 2.2(a). A significant difference in S-O stretching is seen between Li^+ form and tetraalkylammonium form. Tetraalkylammonium cations have weak electrostatic interaction with the electronegative sulfonate group due to the size. Among S-O stretching associated with tetraalkylammonium cations, δ (S-O/TMA) > δ (S-O/TEA) > δ (S-O/TBA), which also follows the trend that smaller cation tends to have stronger interaction with sulfonate group and the corresponding S-O stretching shifts to higher wavenumber.

In aqueous system, the cation polarizing effect was found to be shielded by water [60]. In the case of ACN, in Figure 2.2(b), the S-O stretching of Li^+ form PFSA shifted back to a wavenumber as low as tetraalkylammonium forms. The strong electrostatic interaction between Li^+ and sulfonate groups was alleviated by ACN molecules while the S-O stretching peak shift of tetraalkylammonium form membrane was barely observable. Thus, the interaction between tetraalkylammonium and sulfonate group of PFSA is naturally weak, a significant advantage in the sense that the mobility of cation within PFSA requires its dissociation.

Following dissociation from sulfonate group, ion transport is a solvent-aided process. Thus, the interaction between cation and non-aqueous solvent is also crucial to understand the conductivity/diffusion results. Numerous studies on solvation of alkali salts in ACN are provided a good strategy to follow. Alkali cations being solvated in ACN are spectroscopically revealed in the C≡N stretching area as a new peak shows up at a relatively higher wavenumber compared to C≡N stretching of neat ACN [62,63].

Table 2. 1 Ionic conductivity, diffusion coefficient, λ, and solvent uptake in ACN and H_2O

[a]λ is defined as moles of ACN molecules uptake per mol sulfonate group.

Cation	Membrane	Ionic Conductivity (mS/cm)	Solvent	Diffusion Coefficient (m^2/S)	λ[a]	Solvent Uptake (g/g dry membrane)	Reference
H^+	3M Ionomer 825EW	106	H_2O				
Li^+	3M Ionomer 825EW	23.86	H_2O			0.619 (0.03)	
Li^+	Nafion 212	1.19	ACN				
Li^+	Nafion 1035	0.7	ACN				
Li^+	3M Ionomer 825EW	1.1	ACN		3.31 (0.468)	0.164 (0.023)	
TMA^+	3M Ionomer 825EW	2.43	ACN	2.38×10^{-11}	4.086 (1.787)	0.203 (0.088)	
TMA^+	3M Ionomer 825EW	1.39	H_2O			0.271 (0.019)	
TEA^+	Nafion 212	10.79	ACN				
TEA^+	Nafion 1035	10.7	ACN				Bang[29], Escalante-García[26]
TEA^+	3M Ionomer 825EW	11.4	ACN	3.33×10^{-10}	16.2 (1.985)	0.806 (0.098)	
TEA^+	3M Ionomer 825EW	11.6	H_2O			0.245 (0.038)	
TBA^+	Nafion 1035						
TBA^+	3M Ionomer 825EW	18.1	ACN	3.54×10^{-10}	22.126 (2.561)	1.1 (0.127)	
TBA^+	3M Ionomer 825EW	10.8	H_2O			0.085 (0.007)	

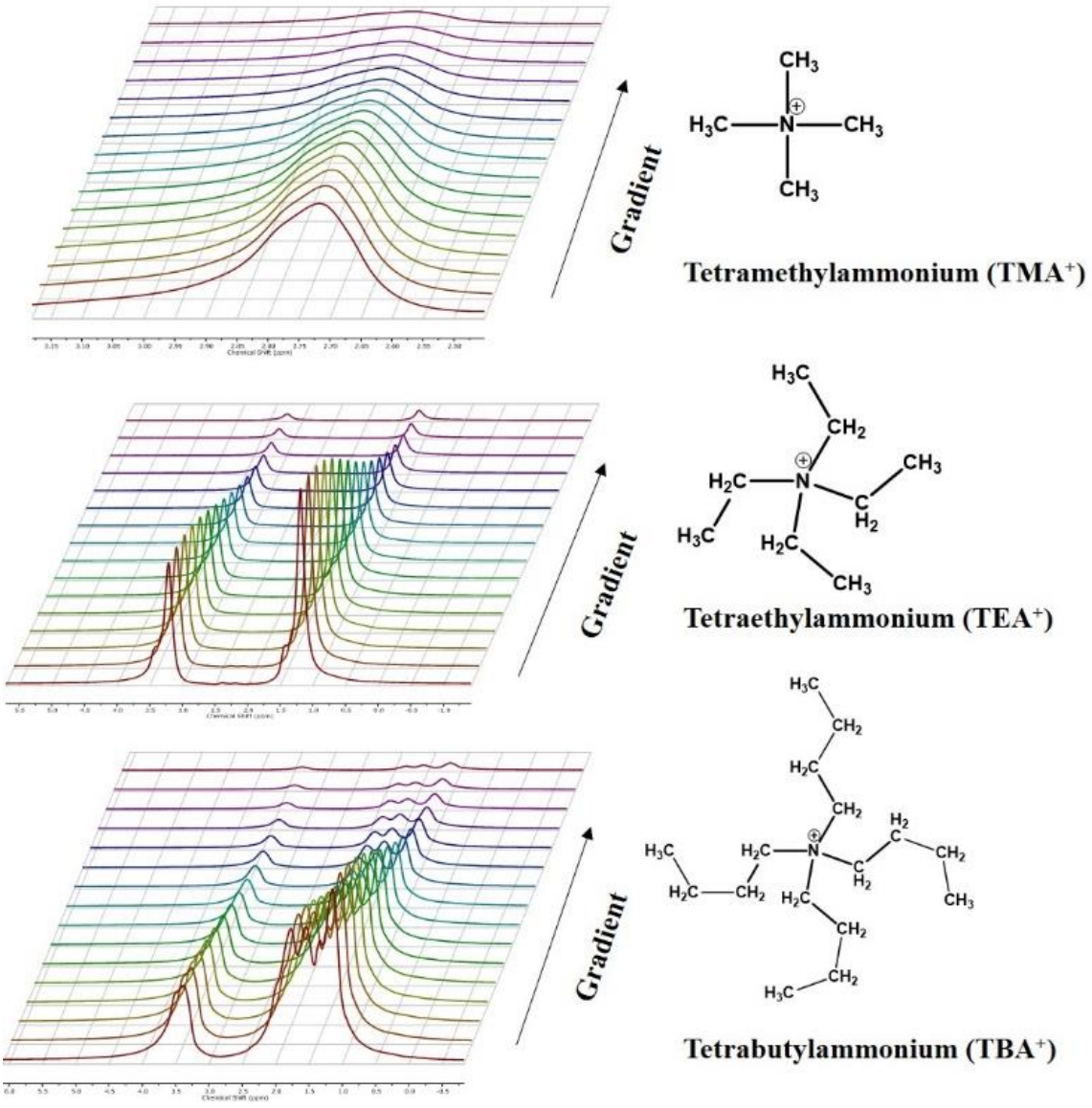

Figure 2. 1 PFG-NMR ^{1}H spectrum of TMA^{+}, TEA^{+} and TBA^{+} form PFSA in deuterated ACN.

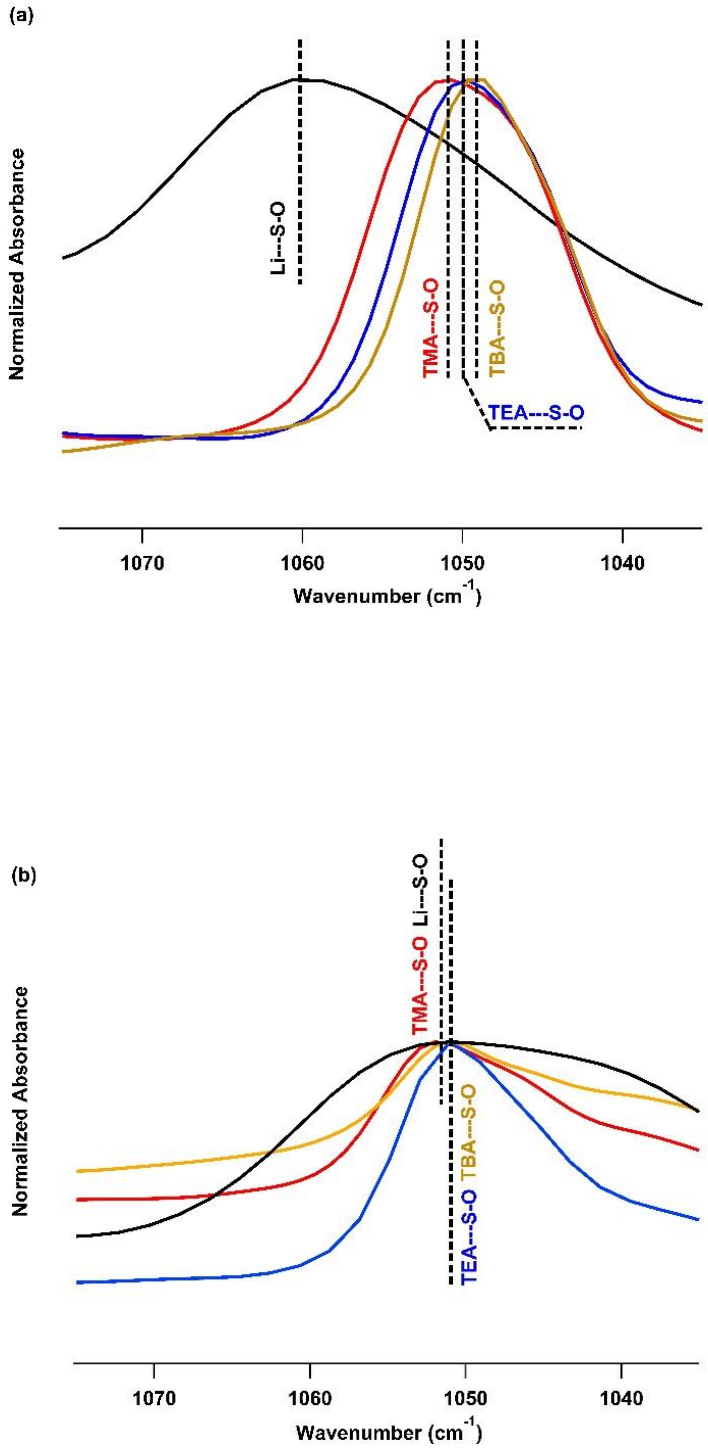

Figure 2. 2 (a) FTIR spectrum of S-O stretching region of dry Li^+, TMA^+, TEA^+ and TBA^+ form PFSA. (b) FTIR spectrum of S-O stretching region of Li^+, TMA^+, TEA^+ and TBA^+ form PFSA swollen in ACN.

We also found this solvation signal from Li^+ form membrane in ACN. In Figure 2.3, a broad peak between 2270 cm^{-1} and 2280 cm^{-1} indicates the interaction of Li^+ and C≡N. It is important to remember that this solvation signal truly represents the interaction within the membrane because Li^+ is only present within the membrane while excess ACN molecules in the IR cell also contribute to C≡N peak at ~2250 cm^{-1}. Tetraalkylammonium forms did not show any solvation peak even when excess ACN was present. This was what we expected from the fact that tetraalkylammonium salts were used to study the *anion* solvation in ACN because they were believed to be extremely weakly solvated[64,65]. Thus, although Li^+ enjoys the advantage of being a small cation to diffuse, its transport within the membrane is in the form of a $[Li^+\text{-}C{\equiv}N]_n$ complex while tetraalkylammonium cations move with less 'electrostatic drag' from the solvent. This is also reflected on the limiting molar conductivity (Λ_m) of cations in ACN solution[41]: Λ_m (TMA^+) > Λ_m (TEA^+) > Λ_m (Li^+) > Λ_m (TBA^+) where ion pairing plays a bigger role than cation size. However, combing the measured conductivity and the fact that a portion of the ACN molecules are needed to shield Li^+ from the sulfonate group while tetraalkylammonium cations are naturally weakly associated with sulfonate group, we can see that cation dissociation from the sulfonate group in PFSA is the dominating factor for cation dynamics. Another question yet to be answered here is the reason behind TBA^+, as the largest cation, showing the highest conductivity while the classic Nernst-Einstein relationship indicates the mobility is inversely proportional to the size. In an aqueous membrane system, the water content determines the proton mobility because water is responsible for the proton transport28. Thus, it is necessary to compare the swelling/uptake of all cation-form membranes in

ACN. Figure 2.4 shows the volumetric change of membranes upon equilibration in ACN. TBA^+ form membrane exhibited the highest volumetric expansion upon swelling while the trend is in agreement with the corresponding ionic conductivity. To our best knowledge, this is the first time such abnormal swelling/uptake behavior is reported. Herein, we want to clarify that careful measurement of ACN uptake/swelling in PFSA is absolutely necessary and cannot be estimated from water uptake[26,27]. In fact, we observed similar uptake results from propylene carbonate (not reported here). Values of membrane swelling widths and thickness are crucial in calculation of ionic conductivity as well.

2.3.3 Membrane swelling/uptake and microstructure

Another question yet to be answered here is the reason behind TBA^+, as the largest cation, showing the highest conductivity while the classic Nernst-Einstein relationship indicates the mobility is inversely proportional to the size. In an aqueous membrane system, the water content determines the proton mobility because water is responsible for the proton transport[28]. Thus, it is necessary to compare the swelling/uptake of all cation-form membranes in ACN. Figure 4 shows the volumetric change of membranes upon equilibration in ACN. TBA^+ form membrane exhibited the highest volumetric expansion upon swelling while the trend is in agreement with the corresponding ionic conductivity. To our best knowledge, this is the first time such abnormal swelling/uptake behavior is reported. Herein, we want to clarify that careful measurement of ACN uptake/swelling in PFSA is absolutely necessary and cannot be estimated from water uptake[26,27].

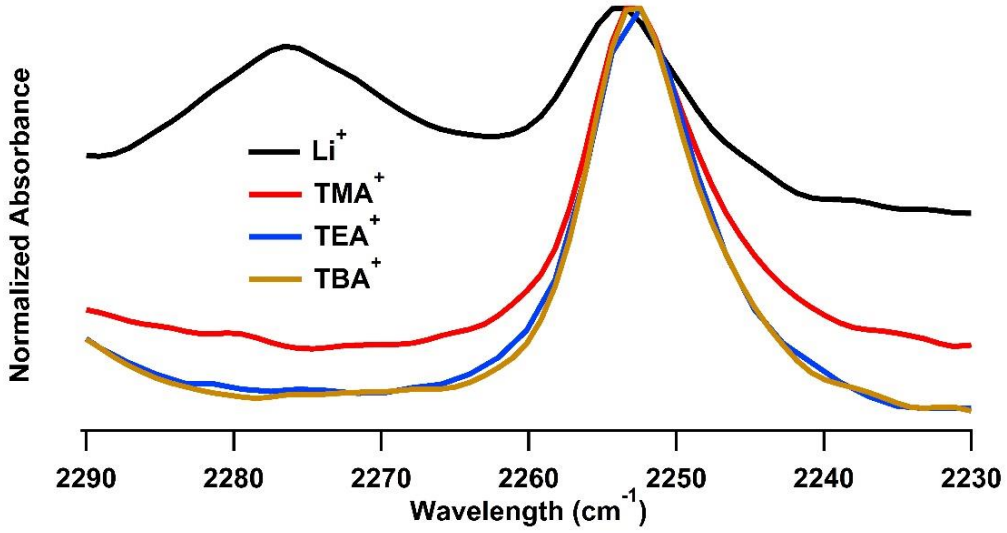

Figure 2. 3 FTIR spectra of C≡N stretching region of Li^+, TMA^+, TEA^+ and TBA^+ form PFSA swollen in ACN.

To further understand the reason behind the difference in swelling, dry membrane density (d) of various cation forms was measured. Although Li^+ is the representation of alkali cations in this work, density of Na^+ and K^+ form PFSA were also included in Figure 2.5. Density-size relationship between alkali and tetraalkylammonium cations are totally different. While the density pattern of alkali cation form PFSA can be explained as increased molecular weight ($K^+ > Na^+ > Li^+$), the pattern among tetraalkylammonium cations must be connected to the morphology change brought by themselves. Previous XRD[66] , SAXS[67], SANS[68] and vibrational study[61] of Nafion indicated that tetraalkylammonium cation's existence within membrane changes the ionic domain due to weaker electrostatic interaction[61]. Compared to alkali form PFSA, the polarity of the ionic cluster is disturbed due to the lower surface charge density[61], a reflection of cation size. Our density measurement also agrees with decreased density in the ionic domain of tetraalkylammonium form PFSA characterized by SAXS[67]. Thus, larger tetraalkylammonium cation essentially provides more 'space' or 'porosity' within the membrane. It is interesting to note that tetraalkylammonium ions were found to alter the thermodynamic relaxation as an 'electrostatic crosslinker' [69]so that ionomer films can be melt-processed[66]. We studied this ordered orientation induced by tetraalkylammonium cation by SAXS. In SAXS, the total scattered intensity (area under peak) is directly proportional to the population of crystal domain (crystallinity) or ionomer domains[70]. We compared SAXS total scattered intensity in Figure 2.6 and found that the order in crystallinity or the population of ionomer domain was $Li^+ < TMA^+ < TEA^+ < TBA^+$.

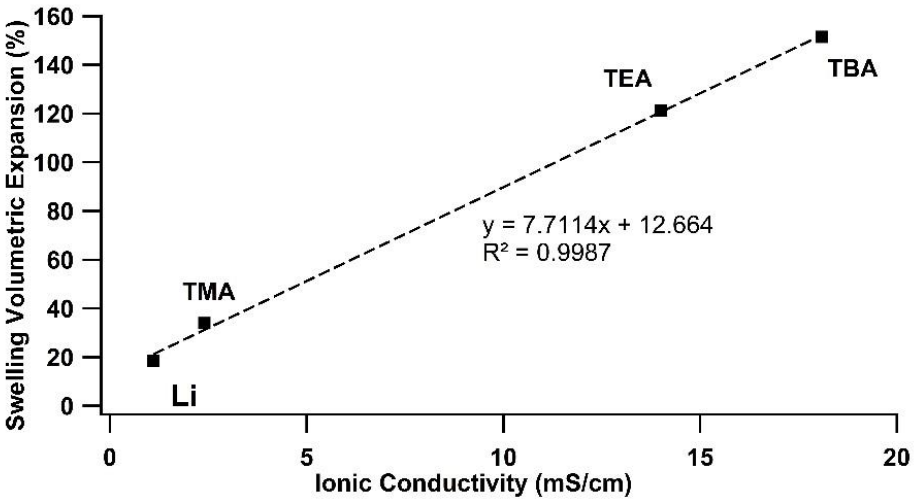

Figure 2. 4 Membrane swollen expansion versus ionic conductivity in ACN with different cations

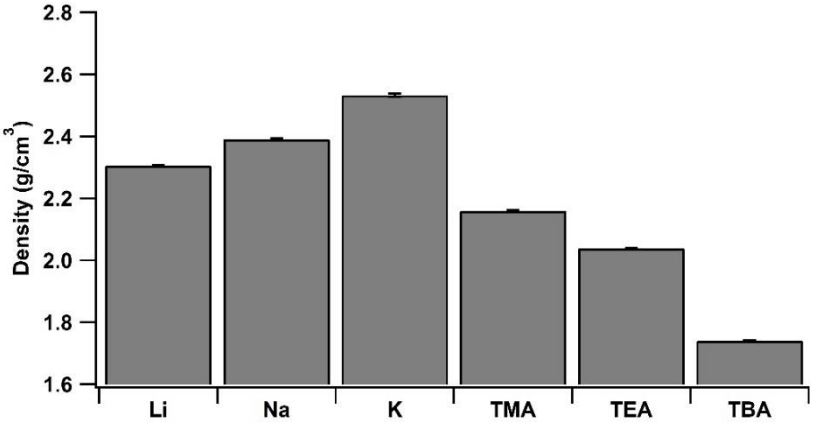

Figure 2. 5 Density of dry Li+, Na+, K+, TMA+, TEA+ and TBA+ form PFSA

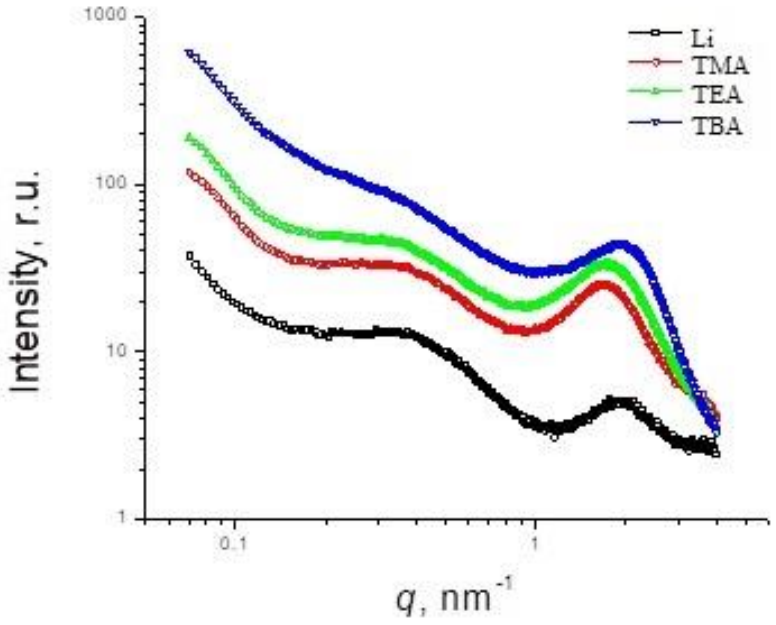

Figure 2. 6 SAXS intensities of membranes as a function of the scattering vector (q).

From the SAXS profiles, it can be seen that the membranes exhibit two clear characteristic peaks at lower and higher *q*. If the peaks at higher *q* are associated with the average distances of the spherical ionic domain, the broad peaks detected at lower *q* correspond to the average distances between the crystalline lamellar stacks of PFSA. Irrespective of the different tetraalkylammonium cations, the peak position of crystalline lamellar stack, q=0.383 nm^{-1} remained unchanged. The *q*=0.383 nm^{-1} indicated that the average spacing of crystalline lamellae is 32.8 nm.

However, we want to emphasize that the 'porosity' does not necessarily lead to high solvent uptake. Table 2.1 lists corresponding ionic conductivity and swelling in water. In aqueous systems, the trend of both swelling and conductivity goes as Li^+ > TMA^+ > TEA^+ > TBA^+. The interaction between cation and solvent is as important as the morphological change induced by cation. Although it seems straightforward that the results are in accordance with the hydrophobicity (tetraalkylammonium) and hydrophilicity (water) of involved species, more detailed interactions are under investigation.

2.4 CONCLUSION

In this work, a systematic study of transport within tetraalkylammonium form PFSA was provided. We observed the following phenomena in PFSA (1) High ionic conductivity/diffusion of tetraalkylammonium compared to Li^+, (2) An unexpected trend of ACN uptake/swelling: TBA^+ > TEA^+ > TMA^+ > Li^+ (3) An unexpected density pattern among tetraalkylammonium form PFSA: d (TMA^+) > d (TEA^+) > d (TBA^+). We conclude that cation type determines its (1) dissociation from the sulfonate group (2) density of the

membrane, (3) uptake, based on its interaction with solvent molecule and (4) subsequent mobility.

Although there are some unexplored aspects in this work, for example, equivalent weight[71] and side chain[72] were believed to impact Nafion behavior in water, it was found that the cation introduced the most dramatic change in terms of transport phenomena from aqueous system to non-aqueous environment. Issues of capacity fade and high internal resistance call for efforts to focus on bridging practical NAFB application with the membrane study. We believe this contribution benchmarked the interaction-oriented study of membrane for NAFB and paves the way for deeper understanding.

CHAPTER 3 COMBINATION OF *IN-SITU* FTIR AND IMPEDANCE MEASUREMENT OF PFSA EQUILIBRATED WITH ACETONITRILE

We report an experimental design of coupling *in-situ* Fourier-transform infrared spectroscopy (FTIR) and impedance measurements to probe the interactions among acetonitrile (ACN), cation and sulfonate group within Perfluorsulfonate Ion Exchange Membrane (PFSA). The goal is to correlate transport behavior within the membrane (conductivity) to non-aqueous redox flow battery (NRFB) conditions. Li^+ and TEA^+ are selected as two models that represent alkali and organic cations. The combined results suggest ACN efficiently dissociates Li^+ cation from sulfonate group and subsequent strong solvation between Li^+ and ACN. Vibrational bands indicating TEA^+ associating with sulfonate group is not observable. Combined with conductivity data, this finding suggests energetics advantage of TEA^+ transport within PFSA compared to Li^+.

3.1 INTRODUCTION

As a model separator for the proton-exchange membrane (PEM) fuel cell and chlor-alkali electrolyzer[36,73], the physicochemical property of Perfluorsulfonate Ion Exchange Membrane (PFSAs) is well-documented. Given that the PFSA is subject to an aqueous environment in most applications, the physical chemistry regarding its interaction between membrane and water is fundamentally important to further elucidate. To date, almost all research contributions have been under the umbrella of a 'cluster-network' of hydrated PFSA[38,74,75]. The consensus describes a hydrophilic ionic cluster (water phase) embedded in a hydrophobic perfluorocarbon phase (perfluoro-phase)[76]. However, the reliability of the model could be questionable in a scenario where water is

swapped with non-aqueous solvent. Alternatively speaking, the transport within the PFSA in non-aqueous system needs to be investigated in more depth.

The Non-aqueous Redox Flow Battery (NRFB) is an emerging application that has been calling for a similar success story to that of PFSA in PEM fuel cell and vanadium flow batteries. There is no doubt that membrane has been a huge factor in the inferior technology readiness of NRFBs. Compared to aqueous counterparts, in-depth study of transport within the membrane is rare beyond its conductivity[24,45,77,78] though PFSAs have been implemented in NRFB[26,27,29,79,80]. Although a complete elucidation of a transport model in a non-aqueous environment is not the goal of this work, we aim to reveal the interactions among membrane (sulfonate group), charge carrier (cation) and solvent by retooling in-situ Fourier-transform infrared spectroscopy (FTIR) to capture transport evidence within PFSA. In detail, Li^+ and TEA^+ cation exchanged PFSAs equilibrated with ACN vapor were carefully monitored by *in-situ* FTIR along with real-time impedance measurement to determine conductivity. ACN has favorable dielectric properties as an NRFB solvent and the volatile nature that a lot of organic solvents share. Li^+ and TEA^+ are typical alkali and organic cations that have been utilized as conducting cation in NRFB study[26,45,78]. However, we believe the transport mechanism between these two types of cations in ACN is fundamentally different. The goal of the study is to create a ‘slow-motion picture’ of how ACN molecules behave upon being imbibed into the membrane to examine the role ACN-ion interactions in membrane swelling by taking advantage of volatility of ACN. The vapor equilibration nature of the experimental design also creates conditions of low solvent content (λ). Similar to a practical PEM fuel cell in which the

membrane is not always subject to 100% theoretical water uptake, solvent uptake in NRFB can also be limited due to high redox species and/or supporting electrolyte concentration, which are needed to improve energy density and conductivity. The addition of a simultaneous impedance measurement helps to correlate the interactions within the membrane to the conductivity value. Additionally, comparison of results at various 'ACN humidity' states with fully swollen state will also be made to give insights into transport within the membrane.

The *In-situ* FTIR is a successful tool to study water absorption[81] , interactions within the PFSA[82,83] and Nafion-Pt interface in fuel cells[84]. The 'in-situ' part is usually fulfilled by exposing membrane to a controlled humidity environment. The versatility of FTIR has long been fully displayed in the study PFSA-water interactions. Proton dissociation or protonation state of sulfonate group is readily distinguishable under conditions of variable humidity[76,85–91] and type of cations[76,87,92]. However, the naturally broad peak of the classic O-H stretching bend is challenging to deconvolute behind reasonable physical meanings with low water content (low signal intensity). This piece of information is crucial to understand the solvation and dynamics. ACN is a relatively simple organic molecule that has an easily observable C≡N stretching bend that contains solvation information[93].

3.2 EXPERIMENT AND METHODS

3.2.1 Materials

3M ionomer PFSA (825EW, ~50) was used both FTIR and impedance measurement. Proton from the original membrane was exchanged to Li^+ and

tetraethylammonium (TEA^+) in their respective hydroxide solutions as reported earlier[50]. Membrane was dried over P_2O_5 for 14 days and kept in argon filled glove box before being cut into 0.5 x 0.5 cm pieces for FTIR and 1 x 5 cm strips for impedance measurement. For ACN (Sigma) was dried over molecular sieve.

3.2.2 Experiment setup

The schematic design of the experiment is shown in Figure 3.1. A home-made cell was placed to on top of the Bruker Alpha instrument to cover the IR diamond crystal in the argon filled glove box. Within the cell, a piece of dry 0.5 x 0.5 cm membrane was pressed on the crystal without extra pressure so that access to ACN vapor would not be blocked. A four-point impedance cell[58] was suspended over the membrane. Data collection (both IR and impedance) started when a tiny cup containing ACN was placed next to the membrane. For IR, a background spectrum of ATR crystal was collected before membrane loading. Each scan is comprised of 32 scans at a resolution of 2 cm^{-1}. The degree of solvation of Li^+ form PFSA (λ) was normalized based on the peak area of respective C-O-C stretching band[94] and ACN uptake. As for impedance measurement, the suspending four-point Teflon conductivity cell was wired to a Bio-logic SP200 potentiostat outside the glovebox. Measured from 200 KHz to 1 HZ, the high frequency intercept of the Nyquist plot was taken to calculate the ionic conductivity.

$$\Sigma = \frac{L_e}{RW\alpha} \qquad (3.1)$$

R is the resistance value read from high frequency intercept with the real impedance between two sensing electrodes separated by a distance of Le. W and α are membrane width and thickness [28]. The experiment was carried out at ambient temperature.

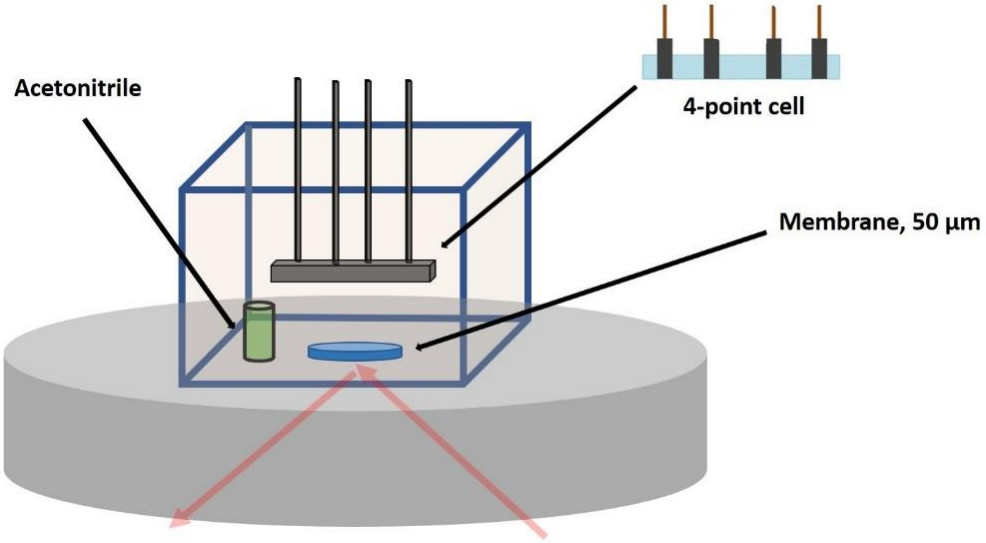

Figure 3. 1 Schematic illustration of in-situ FTIR/impedance setup.

3.3 RESULTS AND DISCUSSION

The $-SO_3^-$ stretching band (~1050 cm^{-1}) of PFSA is a focal point for studying vibrational information of cation association and/or dissociation from the sulfonate group. It does not overlap with C-F bands and reacts to dipole interaction due to cation affinity changed by state of solvation or type of cation. In a non-aqueous situation, this feature still serves as an indicator of degree of cation association. The experiment starts with dry membrane; thus, a strong association between Li^+ and sulfonate group is expected. Upon the introduction of ACN vapor, the peak started shifting to lower frequency, shown in Figure 3.2(a). This blue shift indicates the loosening of Li^+ impact on S-O dipole due to the ACN perturbation. The is the same phenomenon as observed in classic hydration of dry PFSA[76]. Meanwhile, the presence of ACN, indicated by C≡N stretching area, was not recognizable until ~ 10 min into the experiment in Figure 3.3(a). It is quite interesting to observe the ACN triggering the dissociation between Li^+ and sulfonate group even before sufficient accumulation of its content to be observed in one spectrum. Even at this very early stage of dynamic evolution within the polymer, it is evident that ACN is very efficient in 'releasing' Li^+ from the sulfonate group.

In an analogy to OH stretching as a probe of water-ion interaction, C≡N stretching yields information on ACN-ion interaction. As mentioned above, OH stretching can be complicated and needs extensive analysis to sort out[88]. In contrast, C≡N stretching bands of neat ACN and solvating ACN are straightforward and well-documented in studies of aprotic electrolyte solution. While the C≡N stretching band of pure ACN stands at ~2252 cm^{-1}, a new band emerges at higher wavenumber (~ 2275 cm^{-1}) when cation interacts

with the electron-rich N atom of C≡N group[64]. The peak position and intensity of this signal of solvating ACN depend on the type and concentration of cation[65]. The original C≡N stretching band shifts slightly to lower wavenumber and reduces in intensity as solvating ACN builds up[93]. These phenomena observed for solvation in solution also hold true within the PFSA. ACN-swollen Li^+ form PFSA is shown in Figure 3.3(a). The peak shift of the -SO_3^- stretch accelerated after 10 min (Figure 3.4) and was accompanied by the intensity build-up in C≡N stretching area (Figure 3.5). The peak position of this solvated ACN band showed up at even higher wavenumber compared to the same membrane swollen in ACN (Figure 3.3(a)). Given that ACN molecules were overwhelmingly outnumbered by Li^+ at this stage, it is understandable that every ACN was 'wanted' and the resulting interaction was extremely strong.

From a spectroscopy perspective, this scenario (ultra-high cation-to-ACN ratio) has never been reported in even saturated solutions where there is a ceiling of salt solubility. Another very interesting observation is that no signal corresponding to a neat ACN C≡N stretching band is visible (Figure 3.3(a)). Combining this with the previous results of - SO_3^- stretching, we have a rather complete picture of initial ACN entering the membrane. The solvation shell of Li^+ rearranges immediately in favor of being solvated by ACN. Although this early process seems like local dynamics, the corresponding conductivity measurement in Figure 3.4 shows it was responsible for the majority conductivity boost from dry membrane.

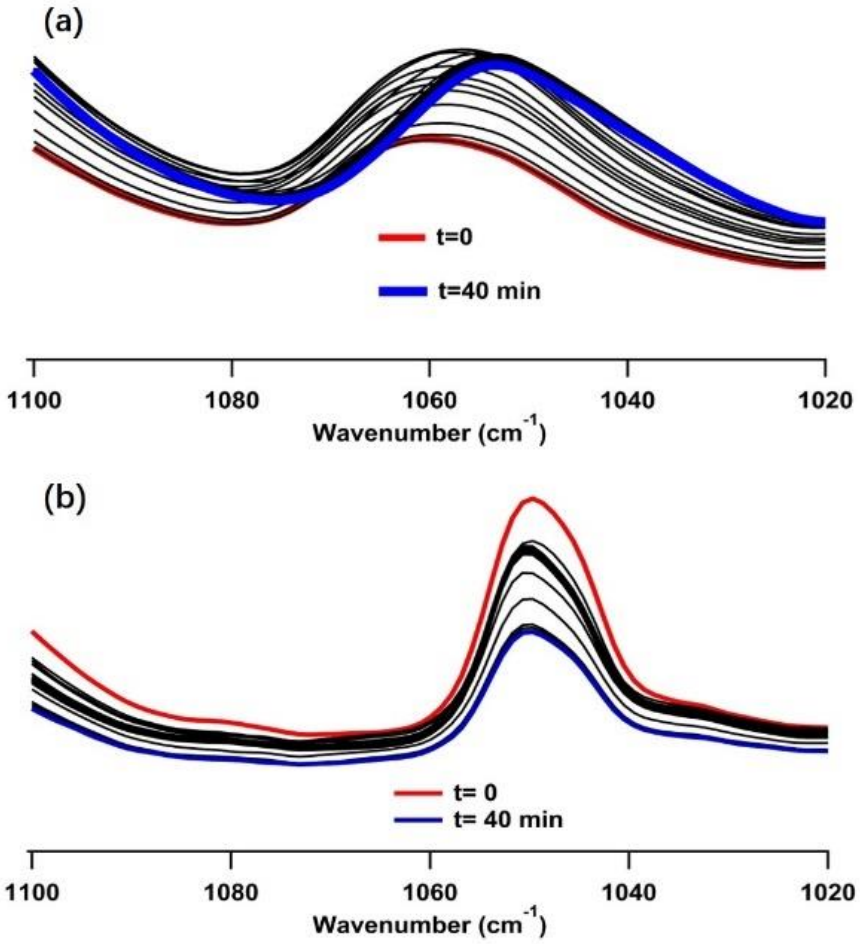

Figure 3. 2 -SO_3^- stretching of Li^+ form (a) and TEA^+ form (b) PFSA over time. Red and blue represents starting and ending spectrum, respectively.

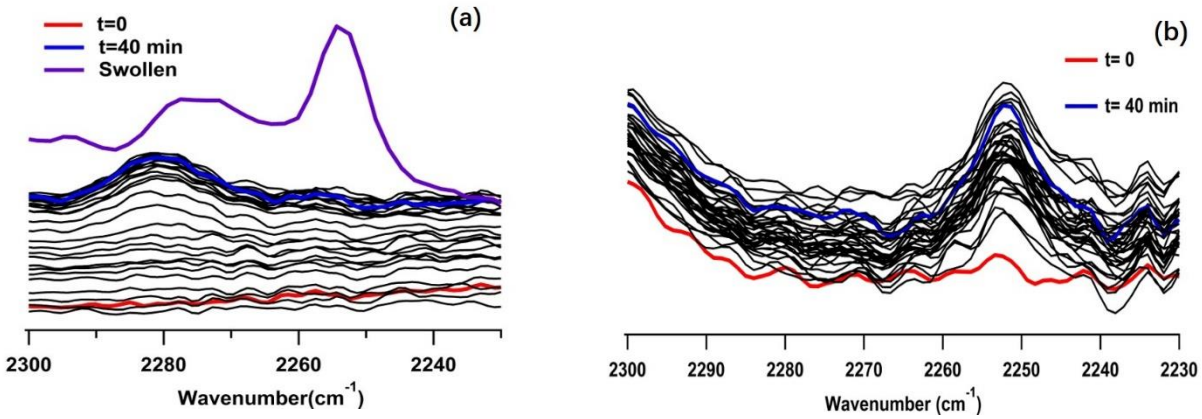

Figure 3. 3 C≡N stretching of Li^+ form (a) and TEA^+ form (b) PFSA over time. Red and blue represents starting and ending spectrum, respectively.

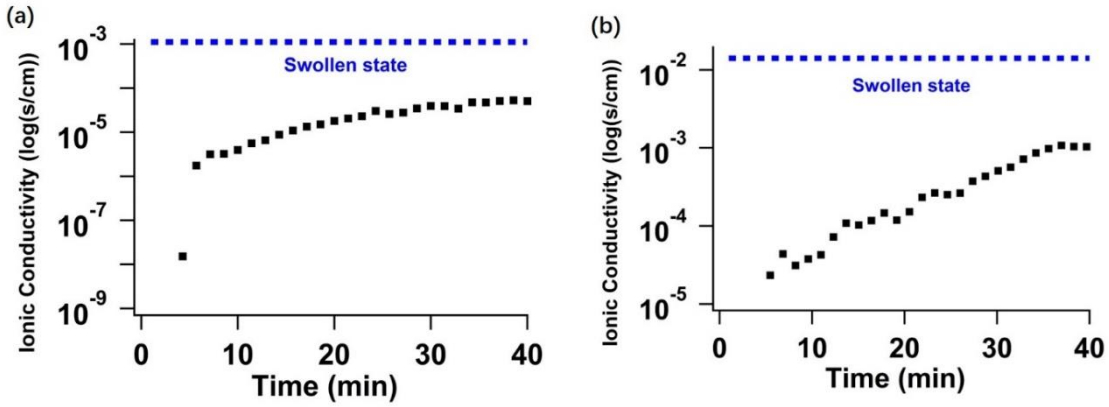

Figure 3. 4 Ionic conducticity of Li^+ form (a) and TEA^+ form (b) PFSA compared with respective membrane in swollen state.

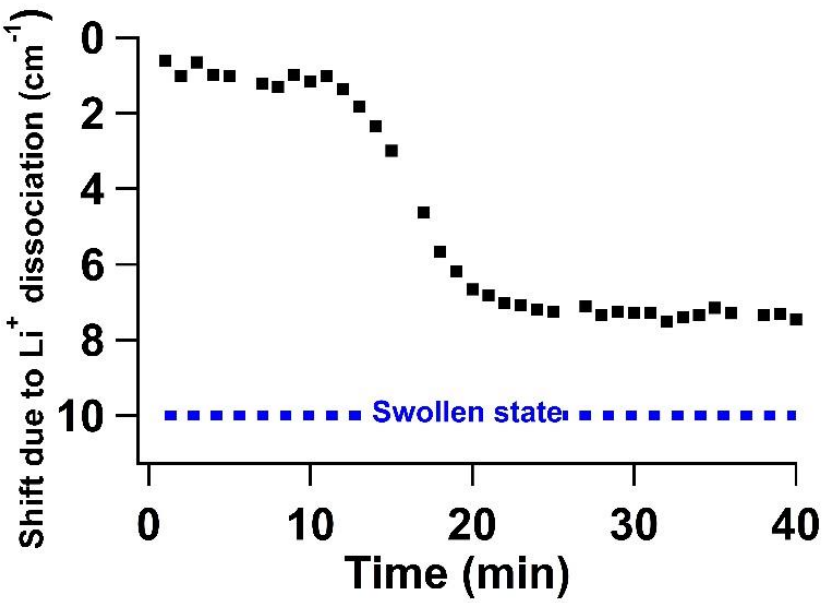

Figure 3. 5 Peak shifts of -SO_3^- stretching of Li^+ form PFSA over time compared with swollen state.

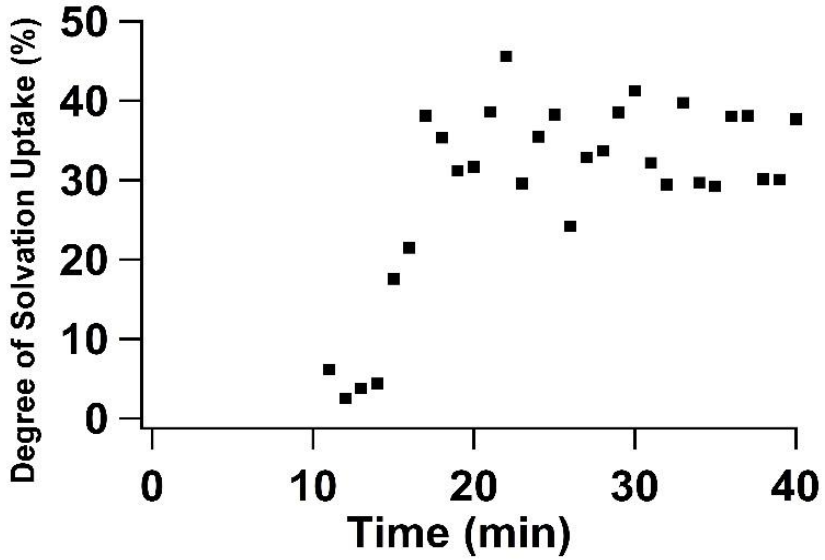

Figure 3. 6 Degree of solvation (∧) based on the C≡N solvation peak area of Li^+ form PFSA over time.

For comparison of different cations, TEA^+ form PFSA was added to this study, exhibiting only weak peak shifts in terms of both $-SO_3^-$ stretching and C≡N stretching band. It is understandable that bulky cations like TEA^+ have very modest surface charge density[61]. Practically, researchers have been using tetraalkylammonium cations as inert cations in electrolytes to probe anion solvation in ACN [65,93,95] and for a broad range of electrochemical studies. As mentioned above, since a unique (compositional) mismatch of cation/ACN ratio was enabled by this experimental design, we hoped to capture evidence that would indicate any solvation of TEA^+. We previously reported no significant $-SO_3^-$ band shift of TEA^+ form membrane in both dry and fully swollen states. It is not surprising that this is also the case for intermediate compositions as the peak position of $-SO_3^-$ stretching remained steady throughout the whole experiment (Figure 3.2(b)). The same trend was seen in the C≡N stretching region as peak shift was barely observed (Figure 3.3(b)). It is worth mentioning that the build-up of ACN in TEA^+ form membrane was significantly faster than in the Li^+ form. Although the kinetics of ACN uptake is not the aim of this study, the difference could stem from the thermodynamics of ACN as an diffusant breaking through membrane surface[82]. Additionally, we have found TEA^+ form PFSA has higher ACN uptake than Li^+ form.

The difference in transport behavior between two cations within PFSA comes from the fact that TEA^+ cations are naturally weakly ion-paired with the sulfonate group. This feature provides TEA^+ form PFSA a huge energetics advantage over Li^+ form because dissociation from sulfonate group is considerably more facile. We can see that this finding is also consistent with conductivity values. Only ~1% conductivity compared to swollen

state was achieved (Figure 3.4(a)) in the process while ~75% of Li^+ dissociation was already completed (Figure 3.5) and ACN participating in the solvation composed ~40% of that of swollen state (Figure 3.6). Although neither cation dissociation nor cation solvation were directly seen, TEA^+ form PFSA was able to retrieve ~10% of swollen conductivity under the same conditions (Figure 3.4(b)). The membranes of both cations had same theoretical ion exchange capacity (IEC) but the difference in dissociation leads to unequal effective mobile cation content within the membrane.

3.4 CONCLUSION

We tailored the technique of coupled in-situ FTIR and impedance measurements to probe the ACN interactions within PFSA. The experimental design made use of the volatility of ACN and took spectroscopic characteristics of all involved species into consideration. Spectroscopically, SO_3^- stretching and C≡N stretching served as an effective one-two punch to trace and track the interactions induced by the ACN introduction into the membrane for the Li^+-exchanged membrane case. Coupled with real-time impedance measurement, a complete picture connecting interaction and conductivity was revealed. We found that ACN molecules can efficiently dissociate Li^+ from sulfonated group and form Li^+/ACN solvation shell. The comparison between Li^+ and TEA^+ form PFSA again pointed to the significance of cation dissociation from membrane. This work also combined classic knowledge of hydration studies in PFSA with solvation studies in electrolyte solutions. The understanding of these topics paved the way for exploration of membrane fundamentals for a new technology like NRFB.

CHAPTER 4 FTIR INVESTIGATION OF MEMBRANE

4.1 SULFURIC ACID-WATER EQUILIBRIUM IN PFSA

4.1.1 Introduction

In previous chapters, we have established a complete analysis of interactions among the cation, solvent and sulfonate group of the PFSA. While the number of moles of the cation tethered to the polymer in a dry PFSA is a fixed value per gram of polymer weight determined by the polymer equivalent weight or ion exchange capacity, the content of solvent can be manipulated to achieve various uptake levels. Dry and swollen states were compared in Chapter 2 and conditions in between two boundary states with a focus on early-stage low solvent content (ACN) was the topic of Chapter 3. Based on this, it is worthwhile to revisit the classic aqueous system with a comprehensive understanding in the non-aqueous system.

The state-of-art vanadium redox flow battery (VRFB) uses sulfuric acid as its supporting electrolyte to boost solubility and provide extra proton source from strong dissociation. Experimentally, the sulfuric acid concentration in a typical VRFB can be as high as 2M, which exceeds the range of ideality used to develop classic theory defined in dilute electrolyte solution[28,96]. The complexity of the electrolyte also essentially voids the Donnan-exclusion mechanism, allowing ‘Donnan breakthrough.’ Thus, to understand the fundamentals within sulfuric acid equilibrated membrane, many efforts have been made in our group to experimentally establish relationships between uptake of ions, interactions in the PFSA[28,49,97–100] membrane and performance in a VRFB.

The relationship between proton transport and acid content within the membrane is the foremost focus in a flow battery. In Figure 4.1, the measure ionic conductivity of Nafion 117 is plotted against the concentration (molality) of sulfuric acid bathing solution in which the membrane is equilibrated[28]. The initial conductivity increases along with acid concentration until it peaks around 2 mole/Kg. This can be briefly explained by the addition of proton introduced by the sulfuric acid. However, the presence of acid molecules is also accompanied with decrease in water content, or de-swelling, as is shown in Figure 4.2.

Even in the non-aqueous systems presented in Chapter 2 and Chapter 3, the solvent content has been shown to determine the cation transport in almost every scenario. In this case, water content drops consistently as the acid concentration picks up. Although the trend of ionic conductivity versus acid concentration is usually explained as trade-off between suppressed water content and added protons (acid), both brought on by the sulfuric acid, the peaking ionic conductivity around 2 mole/Kg in Figure 4.1 is hard to match based on water content in Figure 4.2. In fact, the peak of ionic conductivity has been observed in multiple types of cation exchange membranes. Thus, the goal of this investigation is to extend the FTIR methodology established in previous chapters to explain the peak in the conductivity plot (Figure 4.1).

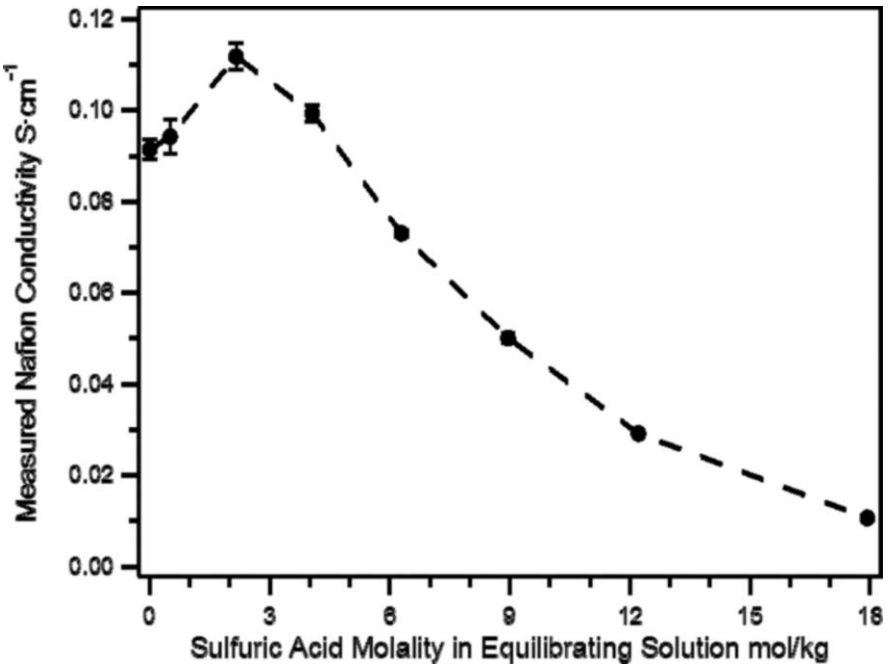

Figure 4. 1 Conductivity of Nafion 117 equilibrated with sulfuric acid[28].

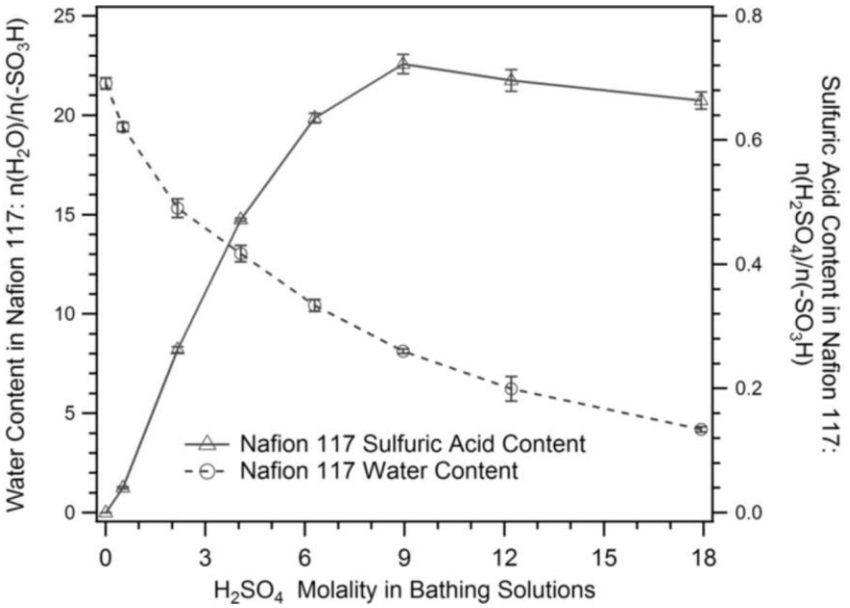

Figure 4. 2 Water content in Nafion 117 vs concentration of sulfuric acid bathing solution[28].

4.1.2 Experiment and Methods

3M PFSA pre-treatment was carried out as described in previous chapters. In brief, membranes were treated at 85°C for an hour in 3% hydrogen peroxide (Fisher Scientific), followed by deionized water (DI) (Milli Q, 18.2MΩ/cm), 1M sulfuric acid (Alfa Aesar). The membrane was then washed in extra DI to remove residual acid. The sulfuric acid bathing solution was made by carefully adding sulfuric acid to DI to make solutions of 0.5, 2.5, 4. 6.5 and 9 mole/kg. The washed membrane was soaked into respective acid solutions for three days. Another set of membranes in DI water was also prepared. After equilibration, each membrane sample was taken out and blotted dry using a Kimwipe.

FTIR measurements were done on an Agilent Cary 600 in ATR mode. At least 128 scans from 400 to 4000 cm^{-1} with a resolution of 1 cm^{-1} were chosen as the resolution. a piece of 0.5 cm x 0.5 cm membrane sample was quickly pressed onto the IR crystal with a sealable cell. The IR crystal and stage were carefully cleaned to remove residual acid.

The ionic conductivity measurement of sulfonated Diels-Alder polyphenylene membrane (SDAPP-136), Nafion 212, Nafion 117 and 3M PFSA (825EW) followed the 4-point probe method as mentioned in Chapter 1 and previous report[28].

4.1.3 Results and Discussion

As mentioned above, the peak of ionic conductivity around 2 mole/kg acid concentration has been observed in membranes of different ion exchange capacity (Nafion 117, Nafion 212) and even backbone chemistry (SDAPP-136, non-fluorinated hydro-carbon cation exchange membrane[97]). Ionic conductivity of Nafion 212, Nafion 117,

3M PFSA and SDAPP-136 were measured in the same manner as in Figure 4.1. Although the exact peaking concentration differs one from another, the general characteristic trend of ionic conductivity in all samples are very similar as shown in Figure 4.3.

As above, we started with observations of the S-O stretching of PFSA. Figure 4.4 shows S-O stretching comparison of membranes equilibrated with DI, 0.5, 2.5, 4. 6.5 and 9 mole/kg. Apart from the regular S-O stretching peak as studied in Chapter 2 and Chapter 3, there is a shoulder peak appears at lower wavenumber at around 1050 cm^{-1}. The peak grows in accordance with the acid concentration of the bathing solution. It represents S-O stretching of all S-O containing species of sulfuric acid derivatives. Note this shoulder was not visible with a resolution worse than 2 cm^{-1}. Although the exact composition of S-O containing species is always preferred to help quantify various components within the membrane, it is difficult to resolve it solely through FTIR. However, we could simply deconvolute the peak of fixed sulfonate group from all other S-O signals originating from sulfuric acid. Such a practice is detailed in Figure 4.5. From DI (a) to 9m (f), individual peak fittings, cumulative fittings and raw data were presented. In the case of DI water bathing solution, the peak can be easily fitted with two sub-peaks in Figure 4.5 (a). This serves a benchmark for comparison with samples equilibrated with acid.

From 0.5m to 9m. the shoulder around 1050 cm^{-1} gradually becomes more prominent. Moreover, the peak cannot be simply fitted into two sub-peaks satisfyingly. A third peak fit (purple, Fitted peak 2 in Figure 4.5 (b)-(f)) evolves along with the acid

concentration. This sub-peak seems to be responsible for the shoulder growth and likely represents the S-O stretching of S-O species of acid molecules.

As mentioned above, the shoulder was not quite observable when data acquisition resolution falls below 2 cm^{-1} (data not shown here). This results in the merging of S-O signals from membrane and sulfuric acid into an even wider peak. From the fittings of Figure 4.5, we can see that the fitted sub-peak at the highest wavenumber among all peaks (black, Fitted peak 3, Figure 4.5 (a)-(f)) maintains its peak position regardless of acid concentration. This information not only confirms the identity of this fit (S-O of fixed sulfonate group) but also indicates that the dissociation of protons from sulfonate groups remains effective since the peak position of Fitted peak 3 does not change even with the dramatic difference of acid concentration. The position of the shoulder, however, steadily shifts to lower wavenumber as acid concentration goes up. While the population increase is assigned to Fitted peak 2, Fitted peak 1 (red, Figure (b)-(f)) has a significant shift towards lower wavenumber, contributing to the overall shift of the shoulder. As we have studied in Chapter 2, this shift can be understood to be caused by a stronger interaction with the S-O containing species (hydration as an example). It is quite interesting that the acid uptake process is essentially a dehydration process (Figure 4.2). Thus, although both Fitted peak 1 and Fitted peak 2 undergo obvious transformation with change of acid concentration, Fitted peak 1 does not necessarily belong to acid based on its relatively stable peak area compared to Fitted peak 3. It is possible that Fitted peak 3 is combination of both acid and sulfonate group of PFSA.

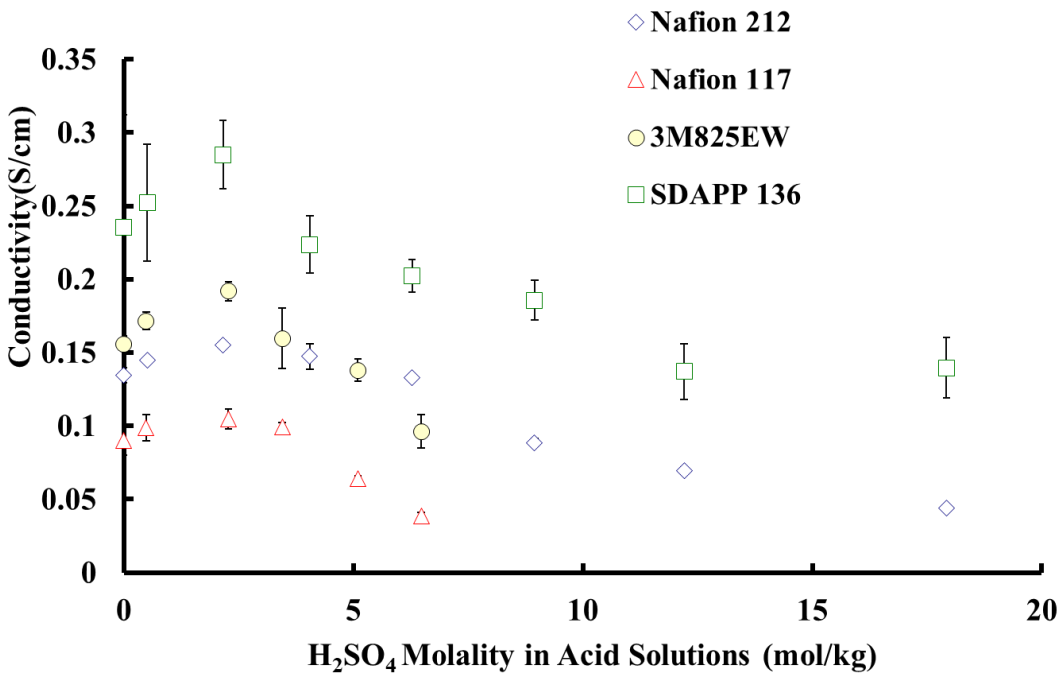

Figure 4. 3 Ionic conductivity of Nafion 212, Nafion 117, 3M PFSA and SDAPP 136 membranes equilibrated in different sulfuric acid concentration.

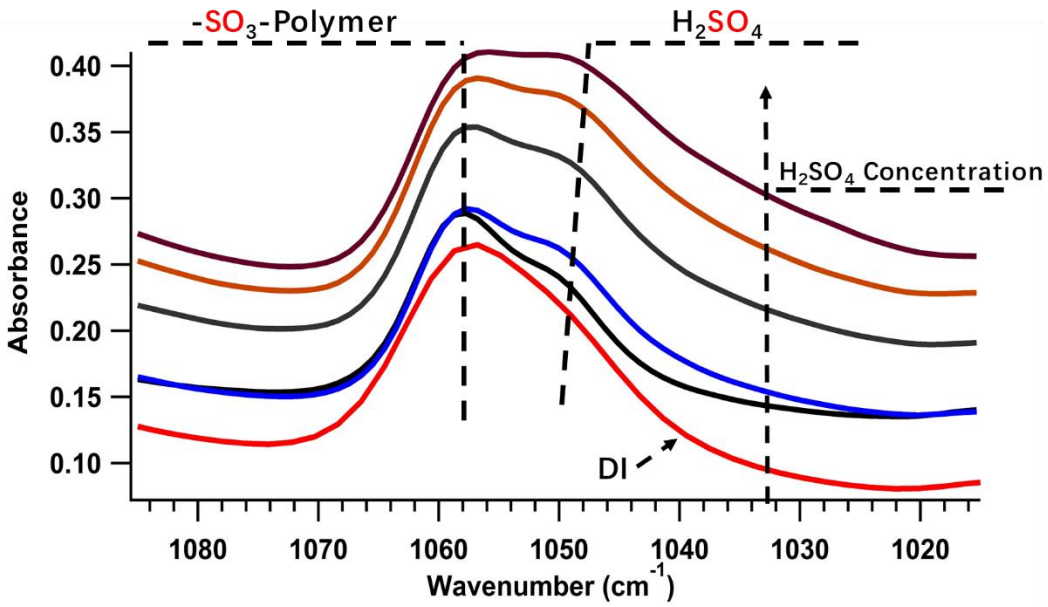

Figure 4. 4 FTIR of S-O stretching of PFSA and sulfuric acid of membranes equilibrated with different acid concentration.

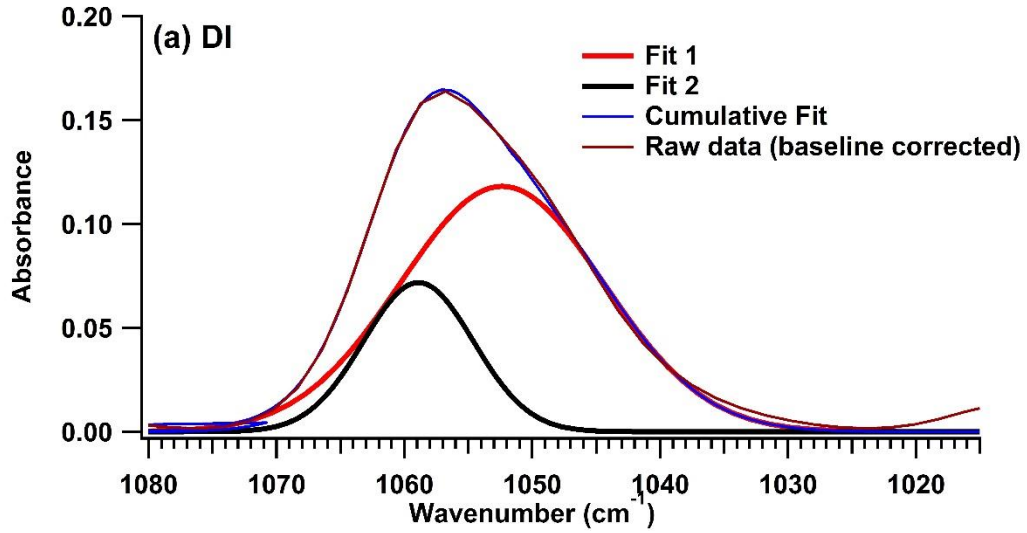

Figure 4. 5 Gaussian fitting of S-O stretching peak of PFSA equilibrated with (a) DI, (b) 0.5m, (c) 2.5m, (d) 4m. (e) 6.5m and (f) 9m sulfuric acid.

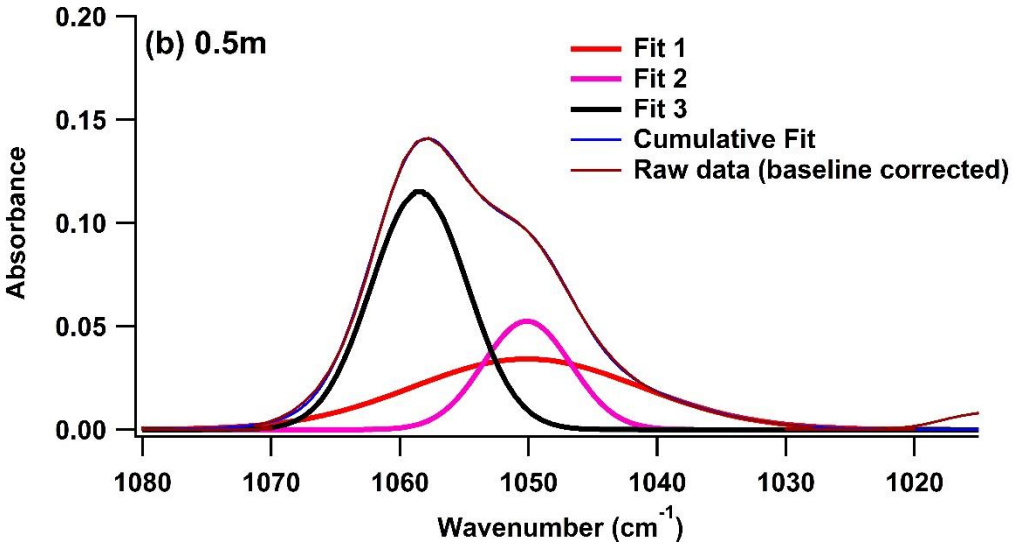

Figure 4.5 continued

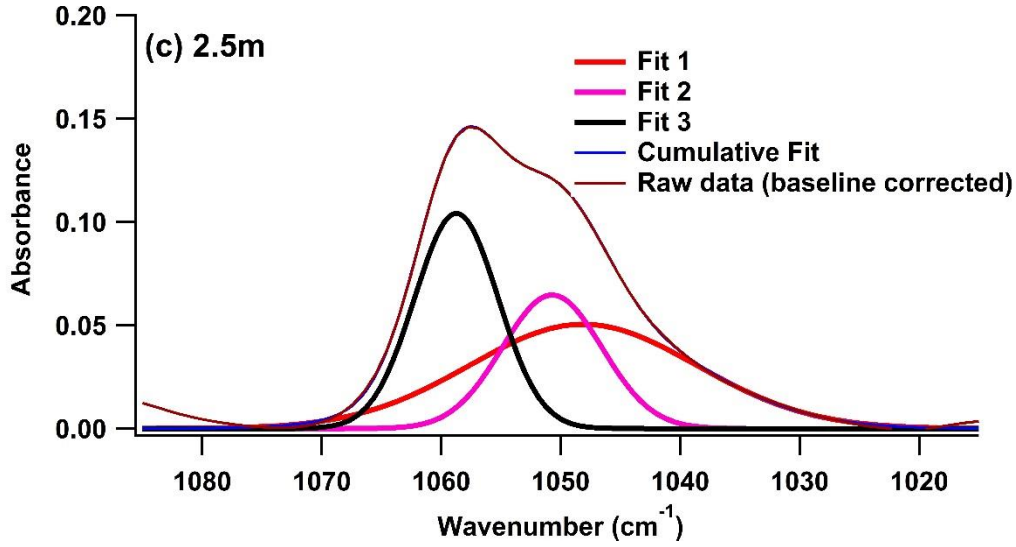

Figure 4.5 continued

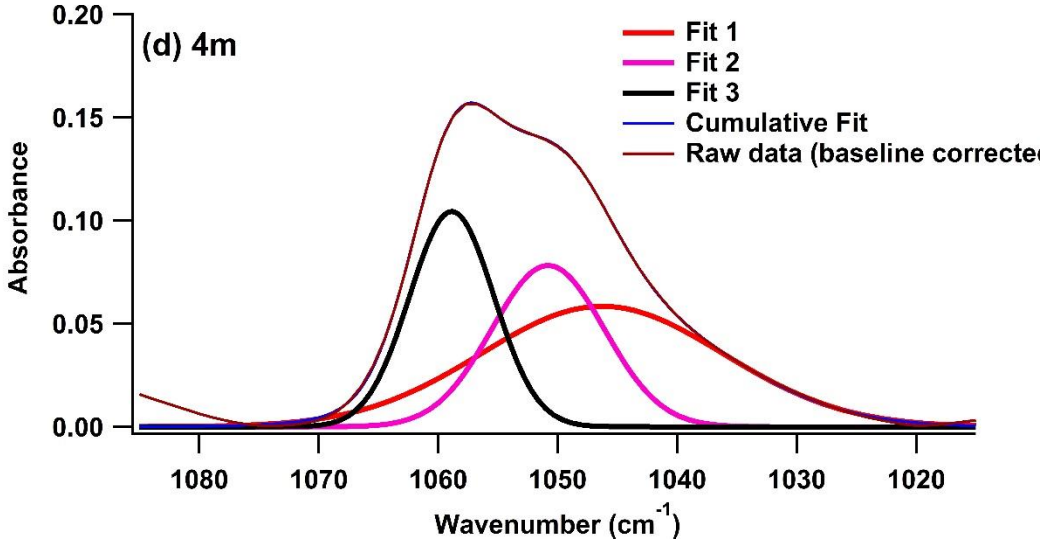

Figure 4.5 continued

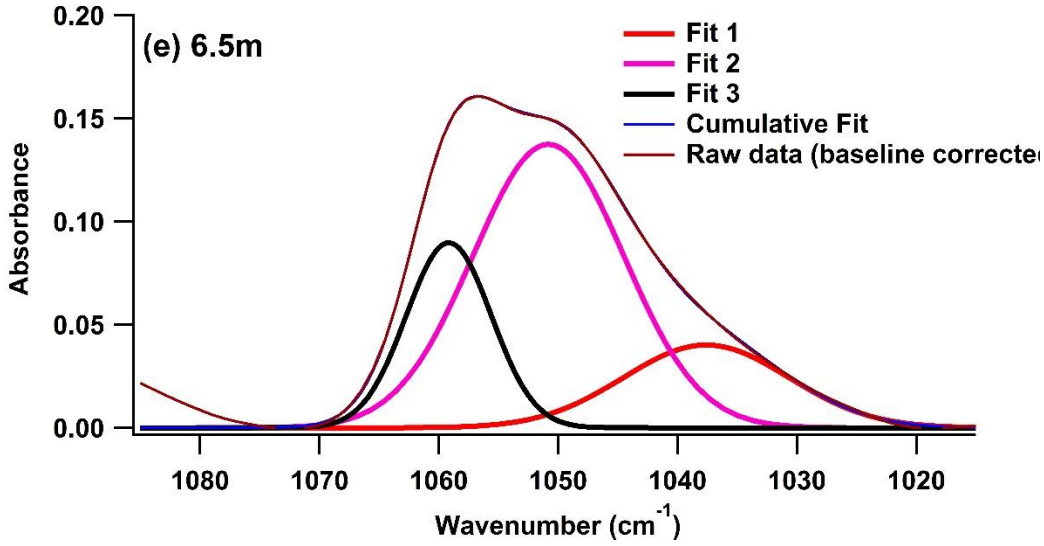

Figure 4.5 continued

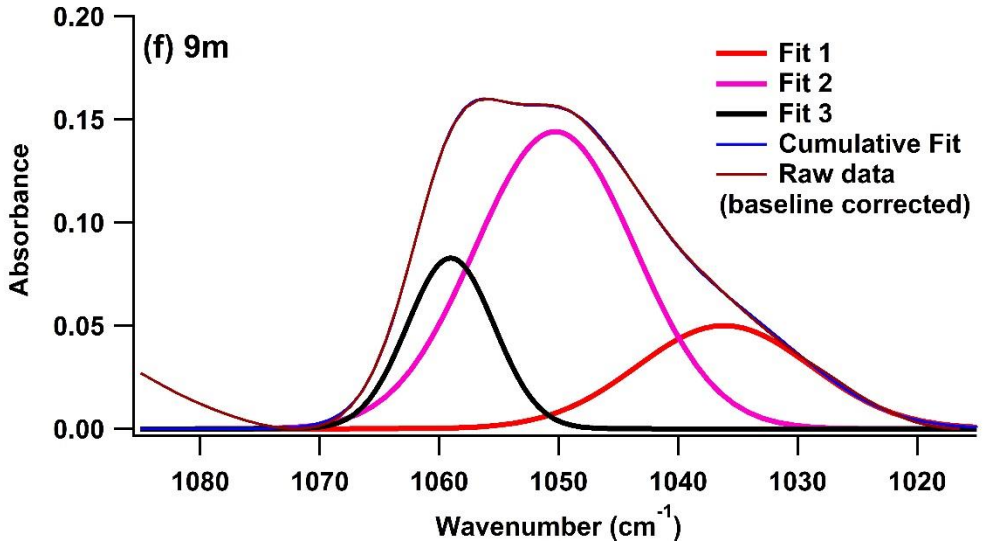

Figure 4.5 continued

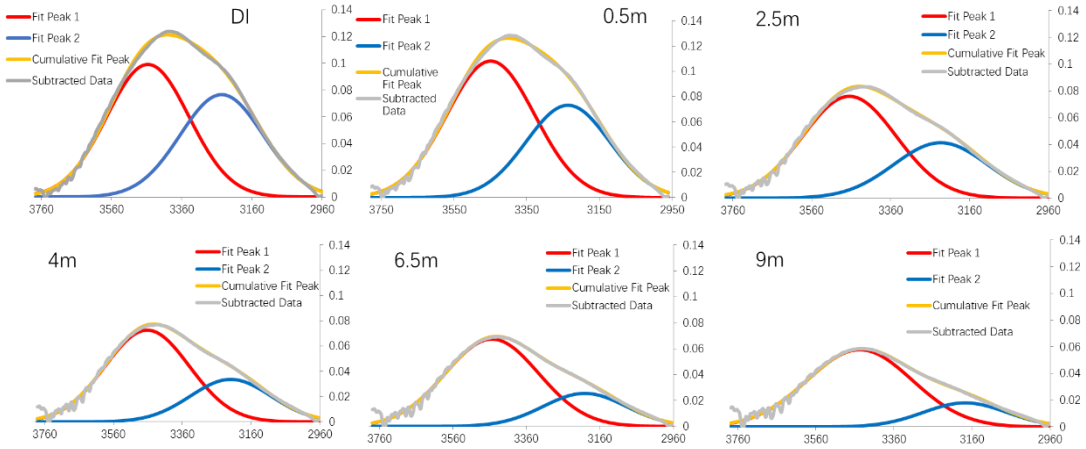

Figure 4. 6 Fittings of O-H stretching region.

We then turned to investigate the classic O-H stretching typically ranging from 3000-4000 cm^{-1}. This approach is similar to the C≡N stretching we have discussed in Chapter 2 and Chapter 3. The O-H stretching band exclusively reflects the bonding information of water molecules in this system. O-H stretching of membranes equilibrated with acid solutions plus that equilibrated with DI water is plotted in Figure 4.6. The diminishing peak area from DI to 9m acid concentration confirms the loss of water content measured by weighing methods. However, due to its broad range and width even in free solution form, obtaining information from the deconvoluted spectrum can be challenging for other than overall water content. In this effort, we were looking for information that can explain the peaking phenomena in Figure 4.1 and Figure 4.3. We simply deconvoluted the O-H signal into two sub-peaks to separate H-bonded O-H stretching and non-H-bonded O-H stretching, plotted in blue (Fitted peak 2) and red (Fitted peak 1) respectively in Figure 4.6. The method has been used in studying the methanol-water-Nafion interaction for Direct Methanol Fuel Cells[101,102]. This categorization aims to connect the vibrational information to effective proton concentration within the membrane. The integration of the non-H-bonded O-H stretching yields its composition among overall O-H stretching band and is plotted against acid concentration in Figure 4.7.

The population of non-H-bonded O-H stretching is directly related to the protons being free to contribute to conductivity and its magnitude broadly mirrors the trend of ionic conductivity. The peaking phenomena now can be attributed to the population of non-O-H bonded proton and corresponding proton mobility. This approach avoided the complicated environment within the membrane that might include

association/dissociation of sulfuric acid and acid autoionization. While protons or water has always been the focus of such studies, focusing on the O-H signal gives a clear view to explain peaking phenomena in conductivity measurements.

4.2 PROPYLENE CARBONATE

4.2.1 Introduction

The vibrational spectra of PFSA equilibrated with ACN have been discussed in detail in Chapter 2 and Chapter 3. The methodology and experimental design of FTIR involving ACN must take into account the volatility of the organic solvent. In the case of Propylene Carbonate (PC), such a precaution is no longer needed since PC is much less volatile. For example, a membrane sample with 100% PC uptake can be realized experimentally.

In this study, we will focus on the cation solvation in PC within the PFSA. The solvation in PC solution has been extensively studied, especially with lithium salts[103]. To compensate for the poor viscosity of PC, PC mixtures with lower viscosity solvents are often used and solvation studies of lithium salts dissolved in organic solvent mixtures have attracted a lot of attention in the field of lithium ion batteries[103–105]. PC is an important solvent for lithium batteries and therefore has been a popular object of interest in the discussion of preferential solvation. The quantification of such preference is based on the population of signal triggered by the solvation of salts in solvent. Although the molecular structure of PC is not as simple as ACN, its signature solvation signal is straightforward to observe and study.

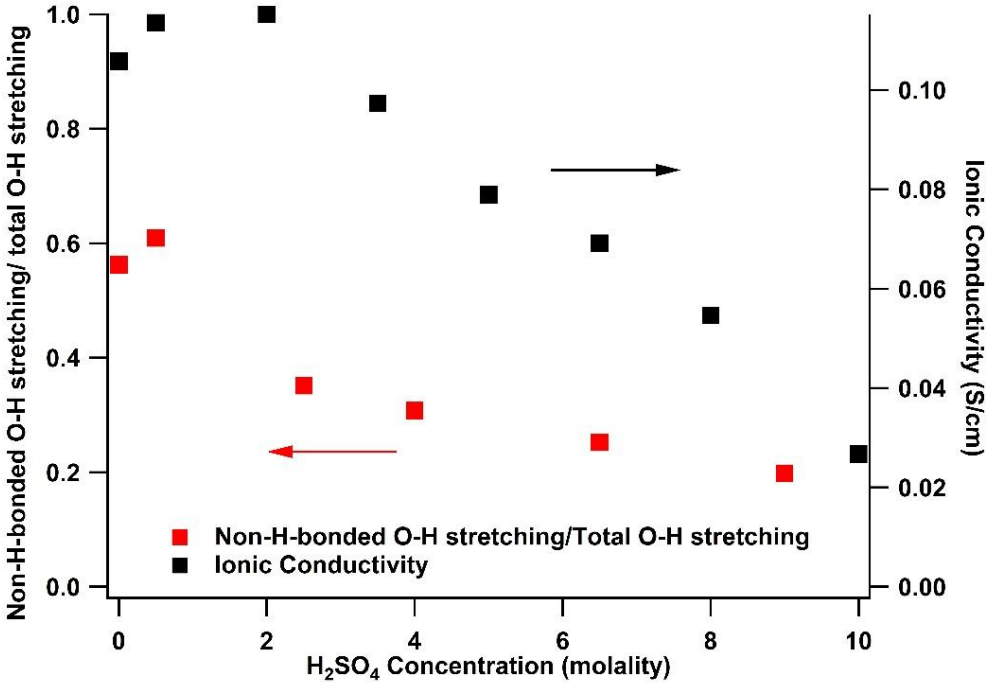

Figure 4. 7 Non-H-bonded O-H stretching composition among total O-H stretching versus sulfuric acid concentration.

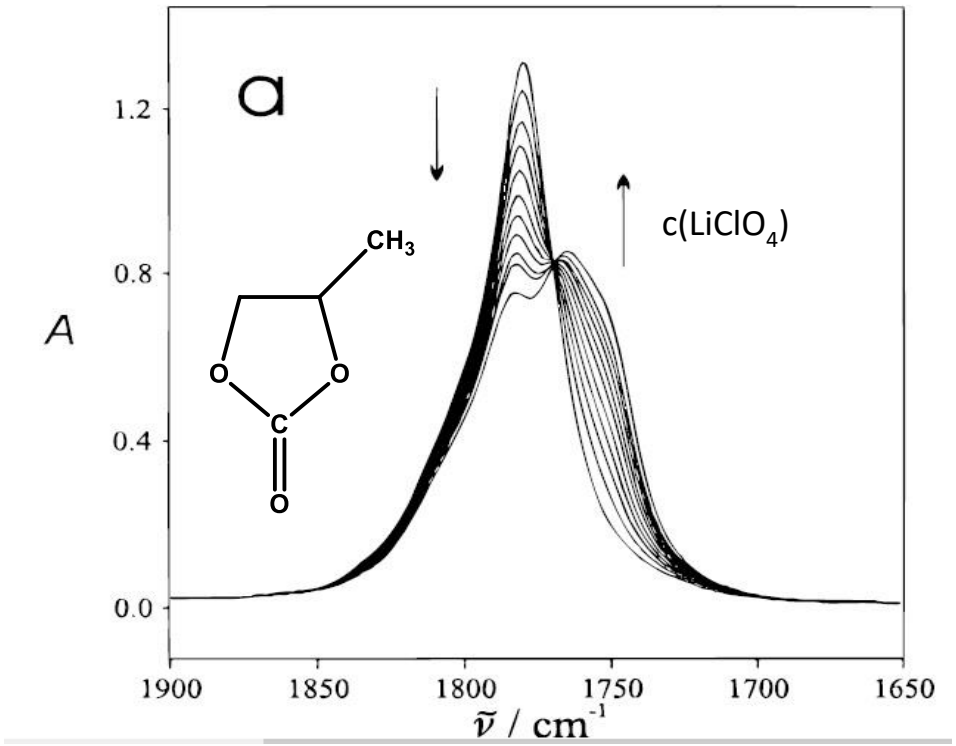

Figure 4. 8 FTIR of salt concentration dependent C=O stretching of PC solvating $LiClO_4$[62].

Figure 4.8 shows the FTIR data of C=O stretching of PC containing dissolved $LiClO_4$[62]. The C=O stretching band of neat PC features a single peak around 1785 cm^{-1}. The coordination between Li^+ and PC induces a peak shift of C-O to lower wavenumber, forming a shoulder on the original peak. The transformation is concentration (Li^+) dependent. Thus, the correlation can be used to calculate the solvation number[106]. Note that this state is difficult to realize with ACN discussed in Chapter 2 where 100% ACN uptake cannot be properly described in IR due to its volatile nature. Although repeating such experiment within PFSA or other confined environment has never been attempted from our best knowledge, the idea is to correlate solvated/unsolvated solvent to solvent uptake or membrane crossover that will be discussed in coming chapters.

4.2.2 Experiment and Methods

FTIR experiments involving PC require exclusion of moisture, similar to ACN. Membrane pretreatment and processing was described in previous chapters. 0.5 cm x 0.5 cm dry polymer strips were immersed in PC for 3 days. Membrane strips were then carefully blotted dry in the glove box before being loaded into IR cell. For experiments with various PC subsaturation quantities in the membrane, droplets of PC were dropped onto dry membranes before sample loading. Extra equilibration time was allowed. Attenuated total reflection (ATR) data were recorded on an Agilent Cary 600. Each data spectrum was averaged from 128 scans from 400 to 4000 cm^{-1} with a resolution of 2 cm^{-1}. The sample stage of cell was carefully cleaned with methanol to remove PC residue and then dried before next sample was loaded. PC uptake measurement was also carried

out in the glove box. 3-day equilibration was also allowed to reach maximum solvent uptake. Detailed measurement steps were described in Chapter 2.

2.3 Results and Discussion

Analogous to the C=N stretching peak of ACN, the C=O stretching peak of PC is targeted to study the solvation between Li^+ and PC within the membrane. In Figure 4.9, the C=O stretching area of different PC content is compared. As opposed to the data in Figure 4.8, the amount of Li^+ was fixed before adding PC and we can see the initial added PC molecules participate in solvation with Li^+. This phenomenon agrees with that observed with ACN in Chapter 3. As the Li^+ are 'satisfied' for solvation, extra PC molecules are introduced in its neat form with no shifts in the C=O stretch. Quantitative analysis of the 100% PC uptake sample allows comparison of the peak areas of solvated and unsolvated peaks in Figure 4.9. The amount of PC that does not participate in Li^+ solvation is overwhelming. Analogous to the C=N stretching peak of ACN, the C=O stretching peak of PC is targeted to study the solvation between Li^+ and PC within the membrane. In Figure 4.9, the C=O stretching area of different PC content is compared. As opposed to the data in Figure 4.8, the amount of Li^+ was fixed before adding PC and we can see the initial added PC molecules participate in solvation with Li^+. This phenomenon agrees with that observed with ACN in Chapter 3. As the Li^+ are 'satisfied' for solvation, extra PC molecules are introduced in its neat form with no shifts in the C=O stretch. Quantitative analysis of the 100% PC uptake sample allows comparison of the peak areas of solvated and unsolvated peaks in Figure 4.9. The amount of PC that does not participate in Li^+ solvation is overwhelming.

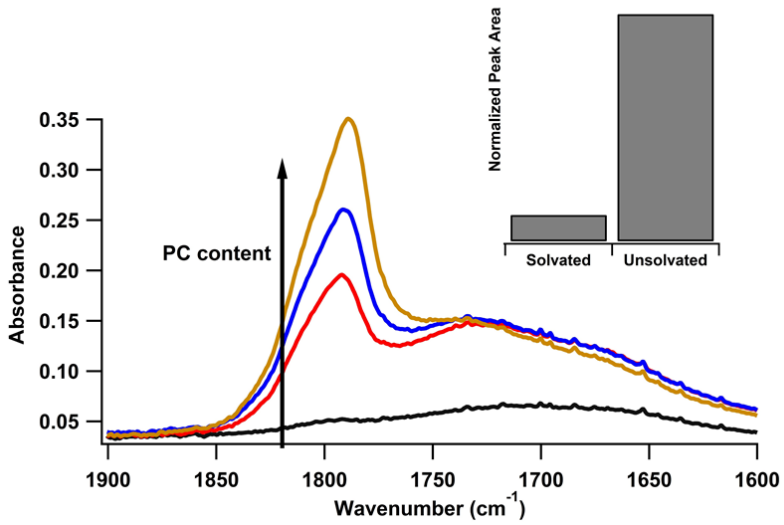

Figure 4. 9 FTIR of C=O stretching of Li^+ form PFSA equilibrated with PC. Signal intensity increases with PC content increase. The brown spectrum represents 100% PC uptake. The corresponding PC content Integration of solvated and unsolvated areas of C=O band are compared in inset.

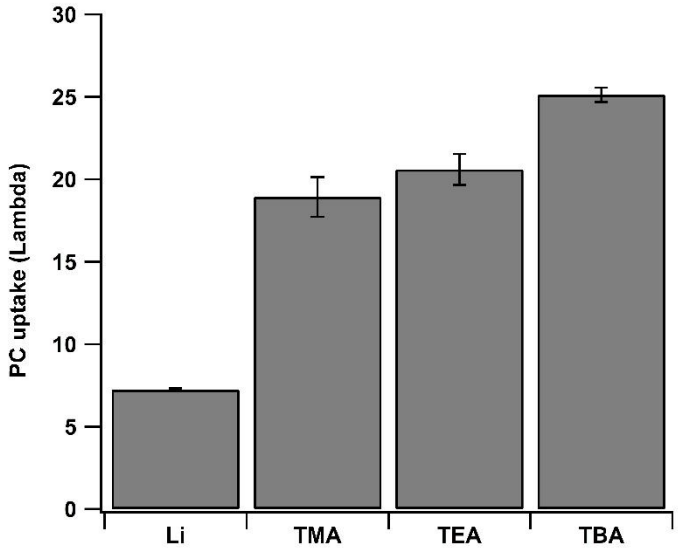

Figure 4. 10 PC uptake of Li^+ and tetraalkylammonium form PFSA.

The study of the behavior of Li^+-form PFSA is illustrated in this part partly due to our interest in the strong interaction Li^+ can trigger. The main motivation for this study, however, is to combine the calculation of unsolvated solvent with the PC uptake comparison among Li^+ and tetraalkylammonium form PFSA.

Figure 4. 10 compares PC uptake of PFSA ion-exchanged with different cations. Li^+ form membrane has the lowest amount of PC uptake among all cation forms. Although the solvation signal of tetraalkylammonium cation in PC is hard to acquire, it is reasonable to predict that the large amount of 'free' PC within the tetraalkylammonium form PFSA is potential contributor to high crossover in a flow battery. In the next chapter, we will also connect the ACN within membrane to species crossover that is assisted by solvent molecules.

4.3 CONCLUSION

Although sulfuric acid and PC are electrolytes of two different systems (aqueous vs. non-aqueous), the methodology of FTIR can be applied to both scenarios where in-membrane interactions were probed to reveal important fundamental properties.

Sulfuric acid, especially in high concentration within a membrane, represents a practical example as it is present in all-vanadium redox flow battery systems. Apart from bulk properties like water content and ionic conductivity, we investigated the effect of different acid concentration on S-O stretching of both PFSA and sulfuric acid itself to reveal molecular level interactions among components. The confusion was elucidated based on careful data fitting and description of an interaction-based peak shift covered in

previous chapter. In terms of the O-H stretching band, we borrowed the trick that has been used in Direct Methanol Fuel Cell and separated the non-H-bonded O-H band from rest of the signal. The composition of non-H-bonded O-H band was found to match the tendency of ionic conductivity found in previous studies. This finding filled the hole of trend of water content not being able to fully explain the peaking phenomena of conductivity around 2m molality of bathing sulfuric acid. We derived the degree of water dissociation by tracking the composition of non-H-bonded O-H band. The dissociation of water molecules provides protons that can effectively contribute to conductivity.

The FTIR study regarding PC was not just complementary to ACN work reported in previous work. The non-volatile nature of PC made it possible to calculate the ratio of solvating and unsolvating PC within the membrane. The results for Li^+-form PFSA gave us insight about free PC that exists in tetraalkylammonium form PFSA. We will bring this information with results in the next chapter that focuses on solvent diffusion to Chapter 6 for deep discussion of membrane crossover.

CHAPTER 5 ADVANCED CHARACTERIZATION METHODS OF PFSA BY NMR FOR NAFB

5.1 NMR RELAXATION AND SOLVATION WITHIN PFSA

5.1.1 Introduction

In terms of NMR techniques, the majority of the efforts in explaining the solvation process has been using chemical shift[107,108]. This is based on the fact that, in theory, the molecular electronic structure or geometry change introduced by solvation will induce resonance frequency changes. Ideally, 'free' or 'bound' nuclei could be simply separated spectroscopically. Comparison of respective chemical shifts within one molecule under one circumstance provides information on the preferred coordination site. ^{13}C chemical shift of carbonyl carbons of propylene carbonate, methyl propionate, ethyl methyl carbonate, N, N-dimethylacetamide and ethyl propionate all indicate that carbonyl oxygen is responsible for coordination to lithium ion dissolved in these solvents[105].

2D NMR is a common methodology in identifying chemical species although its use in interaction probing is limited. A good example is the Interaction between methanol and PEM for the purpose of direct methanol fuel cell (DMFC) It is important to understand the transport of both water and methanol molecules. Apart from examining methyl and proton resonances in simple 1D experiments, 2D NMR methods were also investigated. Figure 5.1 shows the ^{1}H-^{1}H correlation NOESY spectrum of Poly (phenylene ether ether sulfone) (sPEES) membrane with the presence of methanol [109]. The cross peak observed between the methyl proton around 3 ppm and phenyl proton around 7 ppm was clear evidence of spin diffusion between two resonances, indicating a close interaction. A cross peak is an

indication of proximity of two nuclei in space. For NOESY, the nuclei must be within 5 Å to produce cross peaks[110]. This piece of evidence helps clarify the spatial distribution of species of interest within the polymer membrane and is significantly more informative than merely chemical shift observation[109].

In the case of PFSA, water content dependent studies show that the 'water' ^{1}H signal shifts downfield in proton form while it shifts upfield for salt form membranes as the membrane is dehydrated[107]. However, it is not expected that a significant chemical shift can be observed in every case. For example, sp^3 carbon atoms are shielded from the surroundings by a stable coordination sphere[59]. In fact, not only other numerous factors can affect chemical shift as well, the rapid exchange of nuclei between 'free' or 'bound' yields 'averaged' spectrum at best on many occasions. In most cases, separate NMR signals from solvated species are not observable due to rapid exchange between species inside and outside the first coordination sphere[111]. Thus, most spectra obtained instead show an 'averaged' situation, especially at elevated temperature. While many studies of solvation using chemical shifts are done in solutions, a similar methodology is also practiced within confined environments (polymer and composite materials). Early NMR studies of Na^+ form Nafion® showed ^{23}Na underwent a huge chemical shift from saturation to very low water content (1% H_2O). This observation served as a solid evidence of strong and compact ion pair where the amount of water was far from sufficient to solvate sodium ions [112–114]. Resonance linewidths of ^{23}Na for saturated membrane was found to be an order of magnitude larger than ^{23}Na of CF_3SO_3Na aqueous solution with comparable

^{23}Na: H_2O ratio. Sodium cations within the Nafion® are clearly more restricted relative in motion due to the electrostatic interaction with sulfonate group.

Polymer membranes studied in this work are frequently subject to low organic solvent activity environment. Observation of very broad peaks is normal in this case, making interpretation based solely upon chemical shifts extremely difficult and inaccurate. It is important to develop NMR techniques that fits current subject.

Since solvation information is the target of the study, the Nuclear Overhauser Effect (NOE) effect must be brought up. The NOE reflects the cross-relaxation between a magnetically excited nucleus and its neighboring nucleus which is at equilibrium state[115]. It was observed long before in liquid solutions[116]. Because NOE is transmitted through space[117], it is an established technique to probe spatially close nuclei, especially protons, and has been widely applied in synthetic chemistry and biochemistry[118]. Despite its exceptional success in structure and conformation analysis, which usually requires deuterated solvents to be used to suppress intermolecular NOE, the utilization of this technique to study NOE between two or more molecules has been considerably less popular[119]. In this work, however, the spatial arrangement of spins from different molecules is key to understanding the interactions amongst polymer, solvent and cations. Thus, selection of solvent (deuterated vs undeuterated) becomes crucial to take advantage of this technique.

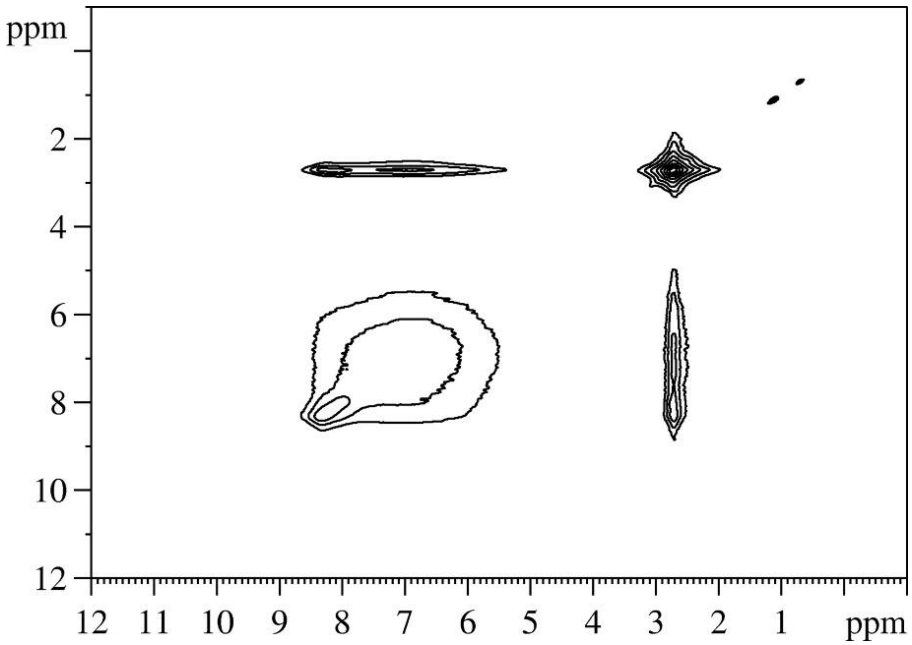

Figure 5. 1 2D NOESY spectrum of sPEES membrane absorbed with methanol, 30KHz spinning and 50ms mixing time[109].

To quantify the NOE effect, the relaxation rate is measurable to yield such information. The NMR relaxation time T_1 is basically the inverse of the rate constant of magnetization returning to equilibrium[59]. The evolution of the longitudinal (M_z) magnetization is characterized spin-lattice relaxation (T_1) while that of the transverse ($M_{x,y}$) magnetization is spin-spin relaxation (T_2). Spin-spin relaxation characterizes the loss of phase coherence of spin in the x, y plane and is associated with the linewidth of the spectrum. It is generally shorter than or equal to T_1. Considering the broad nature of polymer peaks in this work, T_2 is not extensively looked into in this work. However, T_2/linewidth has been used to analyze cation dynamics in polymer electrolytes[120]. The correlation time derived from the linewidth can express Arrhenius behavior to interpret ion motion. Use of T_1 in confined system is well-documented. Water molecules under different dynamics mode (bound or free) trapped in Nafion can be separated by NMR relaxation technique[121]. A similar approach was also applied to elucidate the ^{7}Li transport in lithium thioborate glasses by spin-lattice relaxation measurement[122].

Spin-lattice relaxation, T_1, is the interest of this work to generate a quantitative description of PFSA in non-aqueous system. The total relaxation rate of a nucleus is determined by joint contributions from various time modulated interactions: spin-rotation interaction, dipole-dipole interaction, chemical shift anisotropy and scalar interaction[123]. Spin-rotation mechanism is based on rotation of a molecule and its bonding electron spins. The rotation fluctuates local fields, contributing to relaxation[124]. Dipole-dipole interactions can take place between nuclei belong to same molecule or different molecules. It is the product of ‘interference’ between local magnetic field of two physically

close nuclei. NOE uses this dipole-dipole interaction to reveal such interactions based on spatial distance. The relaxation of proton-bonded carbon is one of the classic examples in this category. Chemical shift anisotropy comes from the anisotropic magnetic shielding of nuclei arising from neighboring electrons[124]. Note that this type of relaxation is negligible for the ^{13}C relaxation.

ACN was a popular subject for relaxation and NOE study when ^{13}C NMR was a rising analytic tool back in 60s and 70s[125–128]. Composed of a methyl and cyanide group, ACN provides a proton-rich methyl carbon and proton-free nitrile carbon in one simple molecule. The different chemical environments of the two carbons in ACN naturally generate two different relaxation mechanism. For methyl carbon, intramolecular dipole-dipole relaxation is dominant at low temperatures while spin-rotation is the dominant mechanism at high temperatures. The nitrile carbon, which is not directly attached to protons, is relaxed through the spin-rotation mechanism at high temperatures and both inter- and intramolecular dipole-dipole contribute at low temperatures[127,128]. Since most of the experiments in this work are carried out at room temperature and the cyanide group is more likely to be oriented toward positively charged cations of the membrane, the intermolecular dipole-dipole relaxation of nitrile carbon is the focus of relaxation study. Previous studies have suggested that nitrile carbon can serve to prove interaction between nitrogen end of ACN and tetraalkylammonium cations[129,130]. It is also important to note that care must be taken in designing the relaxation experiments so that the resulting data is controlled by a known, well-defined relaxation mechanism (intermolecular dipole-dipole relaxation in this work). One of example in the literature was

investigation of ^{13}C spin-lattice relaxation of both methyl and nitrile carbon of ACN in which various tetraalkylammonium salts were dissolved. T_1 of the nitrile carbon decreased as a function of salt concentration. The phenomenon was less pronounced for the methyl carbon. It is obvious that intermolecular dipole-dipole relaxation must be considered with respect to nitrile carbon's relaxation dependence of concentration[129](Table 5.1) while intramolecular dipole-dipole interactions (C-H) dominate the methyl group. Such a concentration dependence of the nitrile carbon relaxation rate was also found in this work where sulfonate group and PTFE polymer backbone together serve as a poly-anion. ^{13}C spin-lattice relaxation is known yields useful information about molecular motion and anisotropy[131].

It is understandable that symmetric tetraalkylammonium cations are not solvated or extremely weakly solvated based on the size. This general assumption of inertness of tetraalkylammonium cations have been proved by conductivity[132], ESR[133] and IR[64,65]. However, ^{13}C spin-lattice relaxation measurements of tetraalkylammonium salts in ACN has showed that the relaxation rate is dependent of alkyl chain length and salt concentration[134]. NOE, paired with viscosity data, was also used to access interaction with respect to tetraalkylammonium and ACN[135]. The alpha carbon of tetraalkylammonium cations is mainly relaxed by its directly bonded proton through dipolar interaction[136,137]

Table 5. 1 T1 relaxation time of nitrile carbon versus different salts concentrations[129].

Acetonitrile C≡N Carbon T_1 Relaxation Times (Seconds)[a]

	solute and NMR probe temperatures				
concn mol/L	TEAP 295 K	TPrAB 295 K	TBAB 300 K	TPeAB 300 K	THAB 295 K
0.01	54.9 ± 1.7	52.4 ± 2.7	53.8 ± 2.7	39.0 ± 2.8	50.4 ± 1.4
0.05	41.2 ± 1.5	54.4 ± 1.5	45.2 ± 1.1	37.6 ± 2.2	53.1 ± 1.6
0.10	39.5 ± 1.0	48.8 ± 2.2	35.0 ± 2.5	35.7 ± 2.2	49.1 ± 0.9
0.25	39.1 ± 2.0	48.5 ± 2.0			47.2 ± 2.0
0.50	38.4 ± 2.0	46.2 ± 1.0	31.0 ± 1.8	33.8 ± 1.7	48.2 ± 1.3
0.75	38.9 ± 1.1	37.3 ± 2.0			43.8 ± 3.5
1.00	36.4 ± 2.0	34.6 ± 1.0	28.0 ± 0.7	31.4 ± 0.7	36.3 ± 1.2
1.10	34.9 ± 2.2	36.3 ± 1.1	27.2 ± 0.7	30.0 ± 1.3	34.7 ± 0.6
1.20	*	*	28.1 ± 1.0	27.3 ± 1.3	32.8 ± 0.6
1.30	*	*	25.7 ± 2.0	27.2 ± 0.8	31.6 ± 1.3
1.40	*	*	23.8 ± 1.2	24.9 ± 1.4	*

[a] Deviations are calculated at the 90% confidence level. TEAP = tetraethylammonium perchlorate, TPrAB = tetrapropy ammonium bromide, TBAB = tetrabutylammonium bromide, TPeAB = tetrapentylammonium bromide, THAB = tetrahexylammonium bromide. * The highest concentration utilized is approximately the solubility limit of the salt in acetonitrile at 294 K.

5.1.2 Experiment and Methods

3M PFSA Membrane in proton form (825EW) was pre-treated as mentioned in previous chapters. The membrane was transformed to TEA^+ form by being soaked in 1M TEAOH aqueous solution for one week. Once TEA^+ cations were exchanged into the polymer, the membrane was washed and rinsed in adequate DI water to remove excess TEA^+ cations. The membrane was then dried over P_2O_5 for at least two weeks in an Ar filled glove box.

The membrane was carefully cut into strips small enough to be fit into standard 5mm NMR tubes. A trace amount of deuterated ACN (d-ACN) droplets were rapidly dispensed onto membrane strips. The number of droplets (amount of ACN) was controlled to intentionally create sets of strips with varied ACN uptake. In this section, 5 sets of samples were prepared. The strip surface was wiped down once the drops were quickly absorbed into the membrane strips. The strips were then carefully loaded into the bottom of NMR tubes. The NMR tube, NMR tube + membrane and NMR tube + membrane + ACN were all weighed carefully. The samples were kept in a glove box for 3 days before measurement to allow equilibration within the tube. A Varian 500 NMR spectrometer was used for the measurement at room temperature. VNMRJ was the software used to carry out the experiment and process the data. The inversion-recovery technique was used to acquire the spin-lattice relaxation time (T_1). ^1H decoupling was applied during signal acquisition. T_1 values were calculated based on the following equation:

$$M_z = M_0\,(1 - 2e^{-\tau/T_1}) \qquad (5.1)$$

where M_z is the Z magnetization at delay time τ, M_0 is the Z magnetization at thermal equilibrium. A set of raw data of partially relaxed ^{13}C acquired is illustrated in Figure 5.2. The molar ratio between TEA^+ and ACN in each sample, $\lambda_{TEA+/ACN}$ is calculated as follow:

$$\lambda_{TEA+/ACN} = \frac{\frac{m_P}{825EW}}{\frac{m_{Sample} - m_{Tube} - m_P}{41.05 g/mol}} \qquad (5.2)$$

Where, m_P, m_{Tube} and m_{Sample} are the masses of dry polymer, empty NMR tube and final sample with ACN droplets.

5.1.3 Results and Discussion

Results from T_1 relaxation measurements on TEA-form membrane with deuterated ACN are presented in Figure 5.3. The T_1 of primary carbon of TEA^+ (black) and nitrile carbon of ACN (red) were plotted against different molar ratios between TEA^+ and ACN in different samples. As mentioned above, the intermolecular dipole-dipole relaxation could contribute to the relaxation of nitrile carbon of ACN. It is worth mentioning that if ACN is deuterated within the membrane, the only proton source would be the hydrocarbon protons of TEA^+. This creates a unique scenario, enabling protons from the TEA^+ to be assessed contributions to the relaxation of the nitrile carbon without interference from other unwanted proton sources. In Figure 5.3, relaxation time of methyl carbon of TEA^+ is relatively stable compared to that of nitrile carbon of ACN. The intramolecular dipole-dipole relaxation of primary methyl carbon of TEA^+ is very effective and is the least sensitive to the surrounding environment[130]. However, the relaxation time

of the nitrile carbon decreased along with increased TEA^+ concentration (less solvent content within the membrane). Compared to relaxation of nitrile carbon in Table 5.1, it can be concluded that the increasing amount of TEA^+, or proton source, significantly relaxed the nitrile carbon of ACN. This observation can be further verified by executing another set of experiments with regular ACN as solvent. It would be expected that the relaxation time of nitrile carbon would be much less sensitive to the molar ratio between TEA^+ and ACN as there would be plenty of surrounding proton source to trigger relaxation.

5.2 DIFFUSION OF ACETONITRILE IN PFSA

5.2.1 Introduction

Proton self-diffusion coefficient value, as determined by NMR has been an important parameter, to complement traditional proton conductivity acquired by impedance measurement[53,56]. Self-diffusion originates from a species' thermal and random motion, which contains rich information concerning its aggregation, association and size[138]. Speaking of 'diffusion', it is natural to compare NMR diffusion with the general narratives such as 'A diffuses through B' or 'permeation'.

While all charged species could theoretically contribute to ionic conductivity, the NMR method pinpoints the motion of a certain nucleus, and indeed, chemically distinct environments for that nucleus. The drawback, however, is that the nucleus could represent more than one exchanging species in a typical (non-ideal) situation. Although it is normally difficult for NMR to read the difference between signals in solution and within the membrane, barring any significant chemical shift change, the overlap in signals can be mathematically solved[139] or can be differentiated via diffusion values[140].

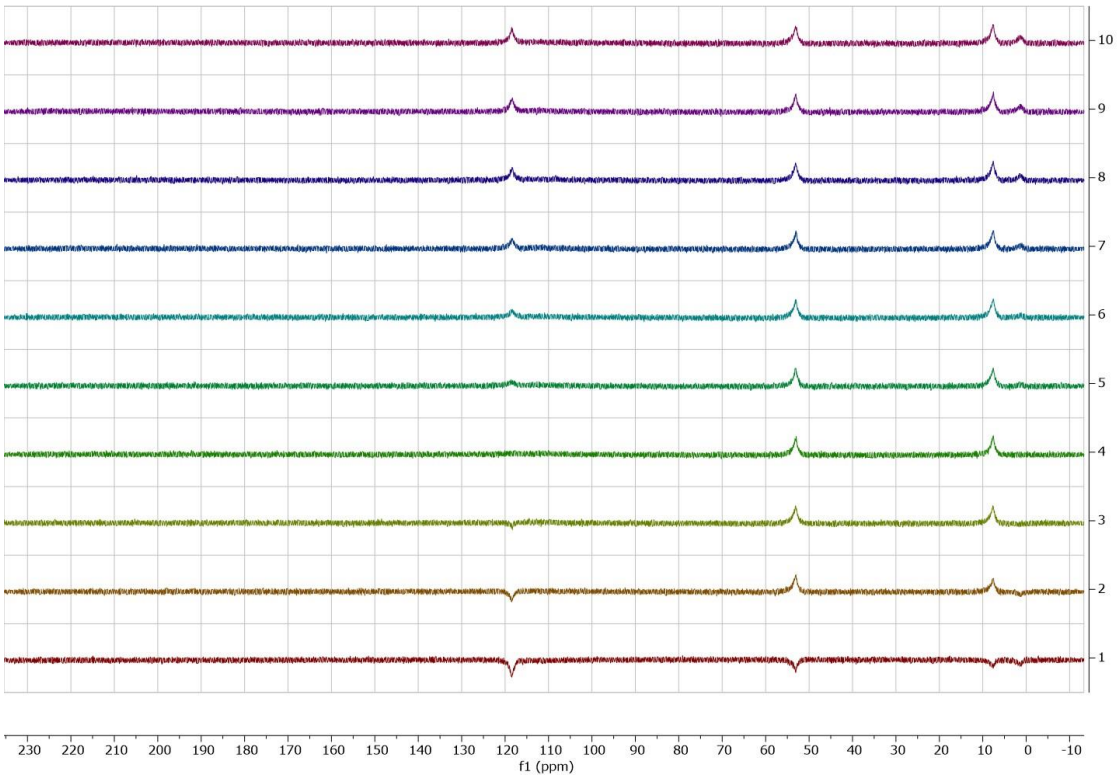

Figure 5. 2 A set of 10 NMR spectra of partially relaxed ^{13}C following 180-Γ-90 pulse sequences of TEA^+ PFSA sample with d-ACN. The X axis represents chemical shift (ppm).

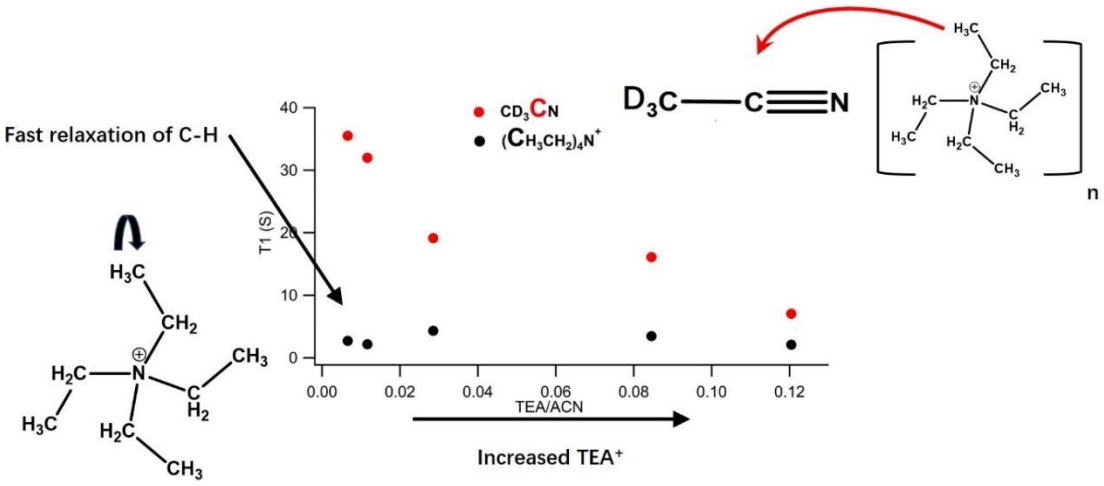

Figure 5. 3 T_1 relaxation of methyl carbon of TEA^+ and nitrile carbon of deuterated ACN versus different ratio between ACN and TEA^+

Proton diffusion within PFSA is technically an average of the diffusion of water molecules and protons. It is extremely difficult to spectroscopically overcome the fast proton exchange rate. The non-aqueous system in this work however provides a more favorable scenario where the NMR signal can be easily distinguished due to chemically-shifted nuclei. For example, tetraalkylammonium cations have protons in a different electronic environment than those in ACN or other organic solvent molecules. This feature creates an opportunity to not only identify but also quantify the diffusion of different species within the membrane.

In previous chapters, we have studied the interaction within PFSA via an approach that taking ACN content into consideration. While qualitative analysis has provided some of most insightful information, quantitative results are always desired if relationship between transport and solvent content is to be established. The combination of proton conductivity as a function of water content has been a classic to evaluate in-depth dynamics in membranes used in aqueous system[58,141–143]. However, this can be challenging for organic solvents that have very different properties than water. In this work, both ACN and PC are the subject of organic solvent to be investigated within the membrane. Although both solvents are common aprotic organic solvents, the discrepancy in volatility makes experiment design totally different between two solvent systems. In the case of ACN, extremely high volatility makes it difficult to manipulate the solvent content within the membrane. In Chapter 2, we measured the self-diffusion coefficient of cation by soaking the membrane in excess d-ACN just to ensure 100% solvent uptake can be achieved during measurement. While it is possible to measure ionic conductivity while

exposing the membrane to different ACN vapor pressures, the corresponding ACN content is difficult to be precisely measured and controlled by this traditional method.

Thus, an NMR setup that features in-situ vapor delivery capability was deployed to measure the diffusion coefficient within membrane while being equilibrated to ACN vapor, as shown in Figure 5.2[144]. In this setup, ACN molecules evaporate from a capillary tube and diffuse through porous separator to be absorbed by the dry membrane at the bottom the tube. The position of capillary tube inside the tube was positioned such that it is not detectable by the instrument. The diffusion coefficient of ACN was monitored over time. The ACN content of each sample was derived from the proton population ratio between cation and ACN. The ratio was then referenced to the 100% uptake value obtained in Chapter 2.

In this part of work, TEA^+, Choline and Trimethylbenzylammonium ($TMBA^+$) form PFSA were selected. While TEA^+ represents symmetric cations, both Choline and $TMBA^+$ forms use an asymmetric cation that will be discussed in Chapter 6.

5.2.2 Experiment and Methods

The membrane treatment method was reported in previous chapters. In short, the PFSA Membrane was exchanged to different cation form using the respective hydroxide solutions. Then the membrane was washed with DI, followed by drying over P_2O_5 for at least two weeks in an Ar filled glove box. The membrane was pre-cut into small strips to be loaded into a standard 5mm NMR tube in the glove box. A few pieces of dry porous separator (Celgard) were then loaded into the tube roughly halfway down. A small

capillary tube was then slowly placed on top of the separator. Dried ACN was carefully injected into the capillary tube before the NMR tube was securely capped and sealed. The reason regular ACN was used instead of d-ACN was that the proton of ACN molecules was the signal of interest for calculating its diffusion coefficient. The setup is illustrated in Figure 5.3.

The diffusion coefficient was measured in a Varian 500 NMR spectrometer with a 60 G/cm gradient coil as mentioned previously in Chapter 2. A DOSY bipolar pulse pair, stimulated-echo pulse sequence was selected to measure the ^{1}H diffusion coefficient of both cation and ACN. The pulse-field-gradient (PFG) measurement of molecular translational motion involves two gradient pulses coupled to three rf pulses. The first one dephases the magnetization and labels initial positions of nuclei, followed by a delay Δ, then the magnetization is refocused via the second gradient pulse/rf pulse pair. Since the molecular motion between two gradient pulses will render the second pulse unable to fully restore the transverse magnetization before the first pulse, reduced signal intensity will be achieved due to molecular displacement. The distribution of the displacement can be described as a Gaussian function to represent the diffusion process[51]. The data is fit exponentially into Stejskal-Tanner equation[52,53] to derive D, diffusion coefficient,

$$I = I_0 * e^{-D(\gamma g \delta)^2\left(\Delta - \frac{\delta}{3}\right)} \tag{5.3}$$

Where I is relative signal strength, I_0 is the corresponding strength without gradient, γ is the gyromagnetic ratio of nucleus, g is the gradient strength and Δ is the diffusion delay described above.

5.2.3 Results and Discussion

One concern in diffusion experiments involving multiple proton-containing species is the overlap of proton signals. Although the diffusion experiment itself can help in separating signals originating from different molecules based on differences in diffusion values, the integration accuracy can be compromised if peaks are significant overlapping. This is exactly the case when a large amount of regular (undeuterated) ACN is involved. Fortunately, the vapor equilibration nature of the experiment design can efficiently prevent an overwhelming proton signal from ACN while revealing proton signals of organic cations at relatively low ACN content.

Figure 5.4 shows the raw proton diffusion data for Choline, $TMBA^+$ and TEA^+ form membranes. As mentioned in Chapter 2, the fluorinated nature of the PFSA rules out any signal from polymer backbone. Proton signals that remain relatively stagnant in response to gradient changes represent organic cations. Meanwhile, obvious signal attenuation, highlighted in the Figure 5.4, can be observed for the peak around 2 ppm. Based on the chemical shift and the fact that ACN is the only (relatively) mobile species within membrane, they can be assigned as the methyl protons of the ACN molecule. While the ACN diffusion values can be calculated, the molar ratio between ACN and organic cations can be obtained from the integration of respective peaks.

Considering the nature of vapor phase equilibrium and the fact that 100% uptake is extremely difficult to create (see Chapter 3), the purpose of this experiment is to make a reasonable prediction of ACN transport as it approaches a high uptake level, based on

the measured trajectory. By default, the diffusion of PFSA always refers to the diffusion of cation of the membrane. In a flow battery however, the diffusion of solvent within the separator or membrane is as crucial as cation diffusion, if not more so. The solvent transport within the membrane is directly related to the permeability. Chapter 6 will provide more details on this topic.

Unlike an aqueous system where the proton represents both cation and solvent dynamics, in a non-aqueous flow battery, the chemical information for cation and solvent can be potentially picked up separately by NMR. Thus, both quantitative composition and diffusion information can be derived from one set of experiment as shown in Figure 5.4. The diffusion coefficient of ACN within each membrane at different uptake level is plotted in Figure 5.5. The 100% uptake was defined as solvent uptake value reported in Chapter 2.

Although all three samples had similar equilibration times, the ACN uptake percentage based on respective full uptake were different. While the rate of the uptake in a setup like Figure 5.3 is not the topic of this work, it needs to be pointed out that the absolute uptake value among three samples were not far apart (between 0.3~1 ACN per cation, data not shown here). It is interesting to see more than 50% solvent uptake was achieved during this thought-to-be early-stage uptake experiment by Choline form PFSA. However, it would not be too surprising if relative uptake ability is compared among membranes of three cation type.

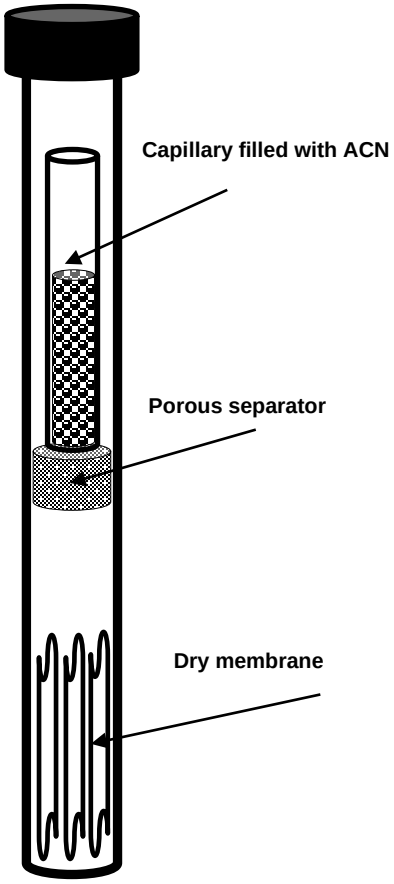

Figure 5. 4 Setup of *in-situ* NMR measurement.

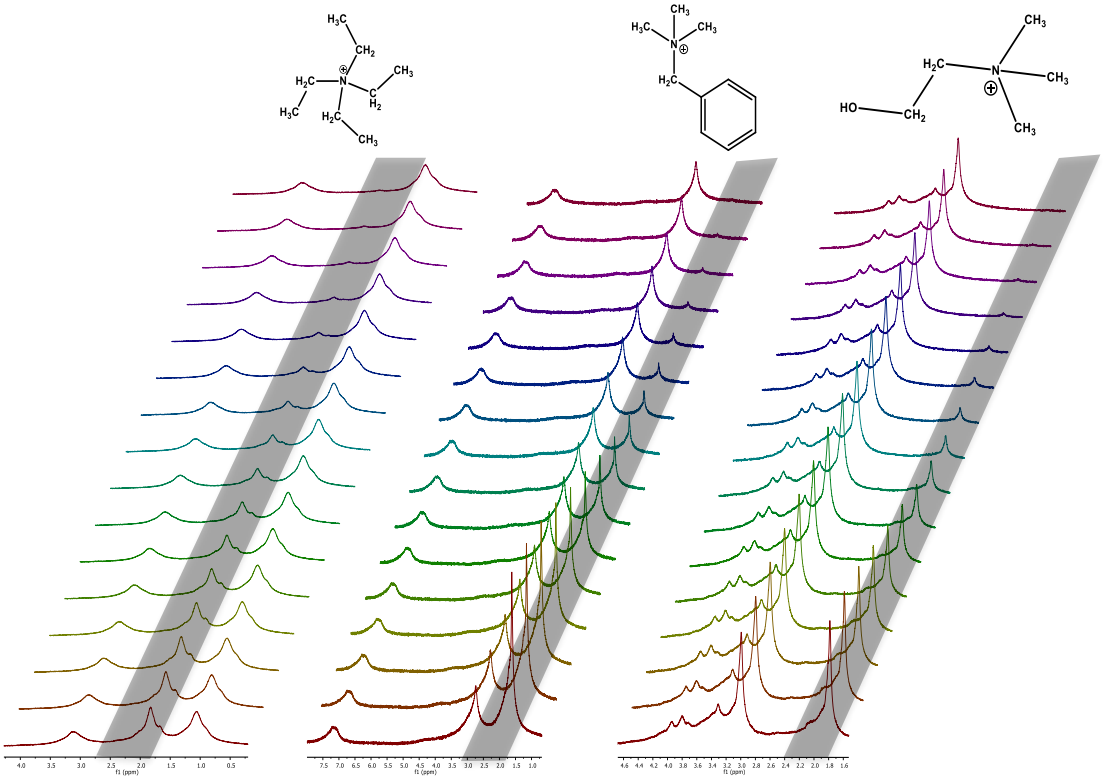

Figure 5. 5 Proton PFG-NMR raw data of TEA^+, $TMBA^+$ and Choline form PFSA equilibrated with vapor phase ACN.

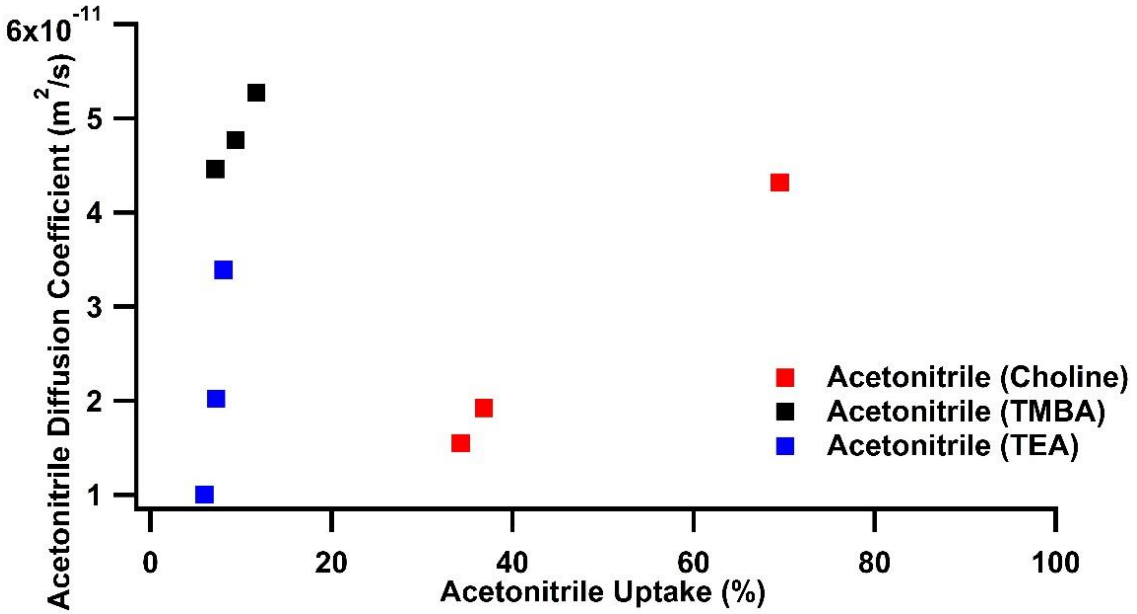

Figure 5. 6 Self-diffusion coefficient of ACN within membrane of Choline, TMBA and TEA form vs. respective maximum ACN uptake percentage.

Figure 5.6 lists a comparison of ACN uptake per membrane sulfonate group among different cation forms. We have mentioned the surprisingly high ACN uptake from tetraalkylammonium form PFSA compared to the alkali form in Chapter 2. TMBA and Choline form membranes, however, do not follow the trend of high ACN uptake as observed for the tetraalkylammonium form. The uptake levels of the two asymmetric cation-exchanged PFSAs are similar to Li^+ form. Combining the previous NMR results in Figure 5.4, it is obvious that the trajectory of ACN diffusion towards high uptake level is tied with the ceiling of uptake. The molar ratio between cation and ACN is a less impactful factor. Membranes with higher uptake provides a pathway that enables faster ACN transport. Density data of dry membranes provided results that indicated a similar perspective that organic cations could alter membrane microstructure to dictate solvent uptake. Thus, it is more of a reflection of the membrane property when different cations are exchanged into PFSA. Since the transport through membrane in a flow battery is impossible without the assistance of solvent molecules, the significance of solvent dynamics is closely related to the crossover/permeation that will be discussed in the following chapter.

NMR measurements in this work are time sensitive and higher gradient is preferred for cation diffusion measurement at low solvent level. While the nature of ACN makes it difficult to acquire both cation and solvent diffusion coefficient simultaneously, PC is a solvent with extremely low vapor pressure that can serve as a perfect solvent to fulfill this challenge.

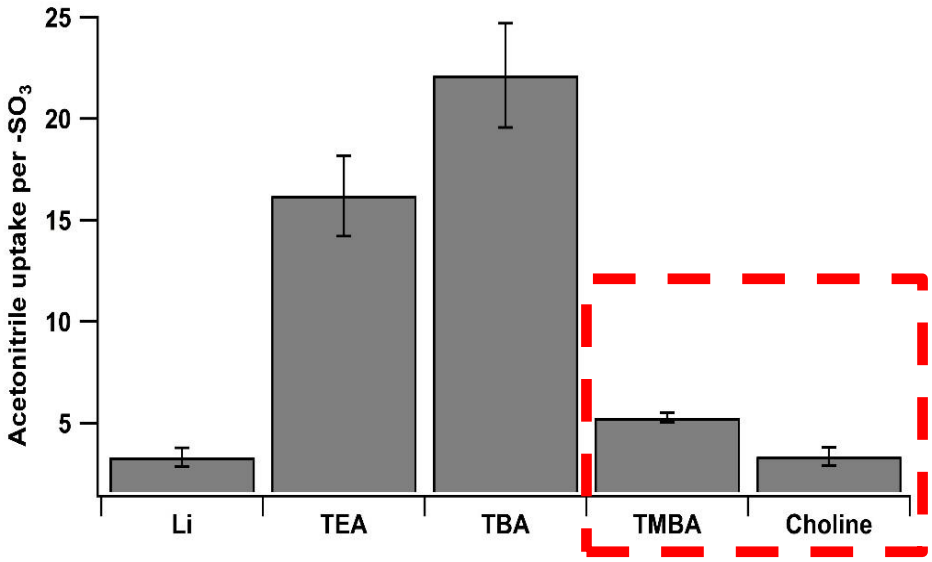

Figure 5. 7 ACN uptake of Li^+, TEA^+, TBA^+, $TMBA^+$ and Choline PFSA.

5.3 DIFFUSION OF PROPYLENE CARBONATE WITHIN PFSA

5.3.1 Introduction

The motivation for PC diffusion within membrane is similar to Chapter 5.2. PC is also an aprotic solvent that has a high dielectric constant (ε) of 64.9 (ε_{ACN}=35.99)[145]. While PC has a relative high viscosity (cP) of 2.5 (cP_{ACN}=0.37) for use as a solvent in a flow battery, it is a valuable complement to ACN in this fundamental study. As mentioned in the previous part, the volatility of ACN is a challenge for advanced NMR experiments that involve ACN content. The diffusion coefficient of cations at various ACN content was not measured due to this difficulty.

In this part, we take advantage of the extremely low volatility of PC and measure the corresponding cation diffusion coefficient along with PC diffusion. Although PC content management via vapor phase equilibration is not possible, we aim to present side-by-side dynamic data of cation and PC at various temperatures. The temperature-based activation energy investigation is a common way to expand conductivity/diffusion data in dynamic studies. However, most such measurements provide one piece of data per ‘sample’ in the sense that an average value representing the bulk material is presented. Thus, the derived activation information is usually compared with other samples with different features (concentration, materials). PFSA conductivity data measured in this classic method will be illustrated. We were able to precisely hand-pick diffusion data of ACN within PFSA. In this work, we were able to present the behavior comparison of PC and cation within the same membrane. The significance of this idea is again related to solvent diffusion that leads to membrane crossover/permeation.

5.3.2 Experiment and Methods

Membrane pre-treatment method was reported in previous chapters. In short, PFSA Membrane was exchanged to different cation form in respective hydroxide solutions. Then the membrane was washed with DI, followed by drying over P_2O_5 for at least two weeks in an Ar filled glove box. Membrane was pre-cut into small strips to be soaked in PC for three days. Membrane strips were then blotted dry carefully with Kimwipe after equilibration. Finally, membrane samples were loaded into a standard 5 mm NMR tube. The diffusion coefficient was measured in a Varian 500 NMR spectrometer with a 60 G/cm gradient coil as mentioned previously in Chapter 2. DOSY bipolar pulse pair stimulated echo pulse sequence was selected to measure the ^1H diffusion coefficient of both cation and ACN. The pulse-field-gradient (PFG) measurement of molecular translational motion involves two gradient pulses. The first one diphase the magnetization, followed by a delay Δ, then the magnetization is refocused. VT temperature control was set from 25 °C to 50 °C. At every temperature step, at least 15 minutes equilibration was allowed.

5.3.3 Results and Discussion

TMA^+, $TMBA^+$, TBA^+ and Choline form PFSA were chosen in this experiment. Arrhenius plots of PC and cation diffusion coefficients in respective samples are shown in Figure 5.9- Figure 5.12. The molecular structure of each cation is also shown in respective figures. Figure 5.9 schematically shows how TMA^+ and PC within TMA^+ PFSA can be separated in NMR diffusion measurement. Since both PFSA backbone and sulfonate group do not possess proton, only proton signals from organic cations and PC

are visible in the spectrum. While the signal of the cation (TMA^+ in Figure 5.9) may or may not be distinguishable based on chemical shift overlap, the peak between 3.5 - 4 ppm, which has lowest signa intensity decay rate, can easily assigned to TMA^+.

While the diffusion coefficient is the measured result, the focus of this work is on the comparison of transport behavior of cation and PC within the same membrane. For example, in a $TMBA^+$ PFSA (Figure 5.10) and TMA^+ PFSA (Figure 5.9), although the diffusion coefficients of ACN in both cases are similar, diffusion of $TMBA^+$ is faster than TMA^+. This is also evident if the relative diffusion of ACN is compared. While $TMBA^+$ is larger in size compared to TMA^+, its faster diffusion suggests the difference comes from the interaction with sulfonate group. As illustrated in Figure 5.7, positively charged cations are attracted to negatively charged sulfonate groups. In Chapter 3, we have learned that solvent molecules help dissociate cation from sulfonate group and the degree of dissociation is related to the solvent content. In this part, while the absolute diffusion coefficient might result from many factors, the relative activation energy (slope of Arrhenius plot) between PC and cation can describe the cation dissociation within the membrane. This also agrees with the IR data of S-O stretching in Chapter 6 where S-O stretching of $TMBA^+$ form membrane shifts to higher wavenumber. Another interesting observation is related to solvent uptake and crossover as discussed in Chapter 5.2. In Figure 5.11, both TBA^+ cation and PC within TBA^+ form membrane show very high diffusion coefficient values compared to other samples.

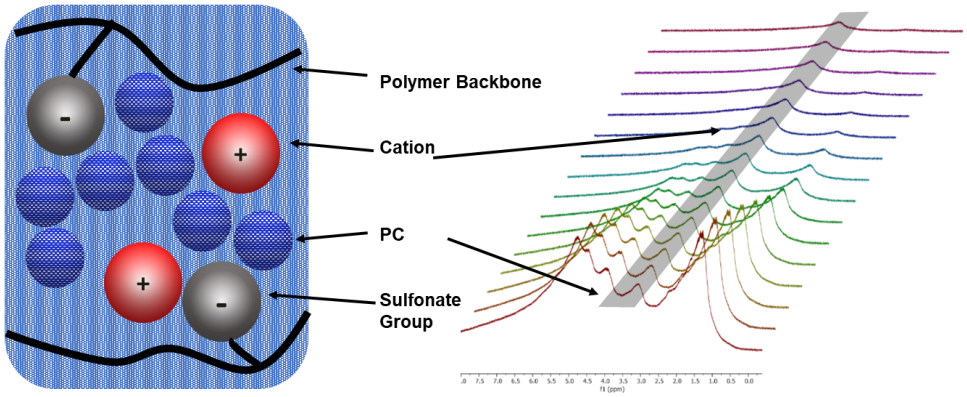

Figure 5. 8 Schematic illustration of diffusion measurement within PFSA membrane. NMR diffusion data of TMA^+ form PFSA equilibrated with PC at 25°C is shown on the right. The highlighted signal (slowest signal decay) represents the methyl proton of TMA^+.

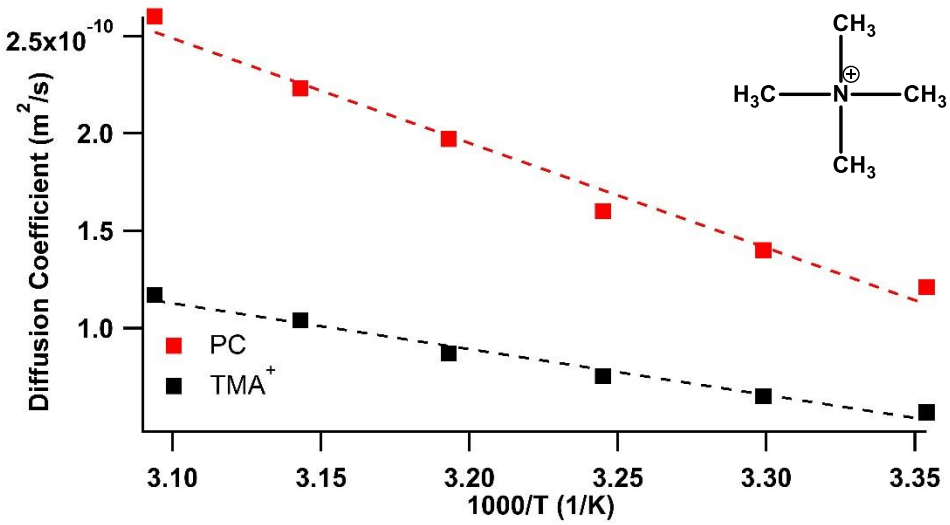

Figure 5. 9 Arrhenius plot of PC and TMA^+ diffusion coefficient within TMA^+ form PFSA equilibrated with PC.

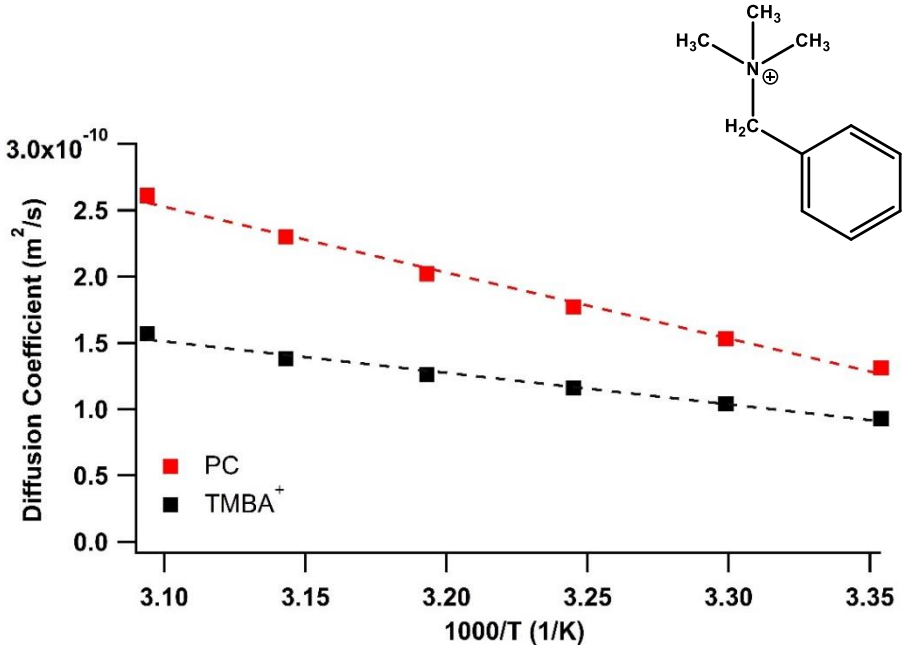

Figure 5. 10 Arrhenius plot of PC and TMBA+ diffusion coefficient within TMBA+ form PFSA equilibrated with PC.

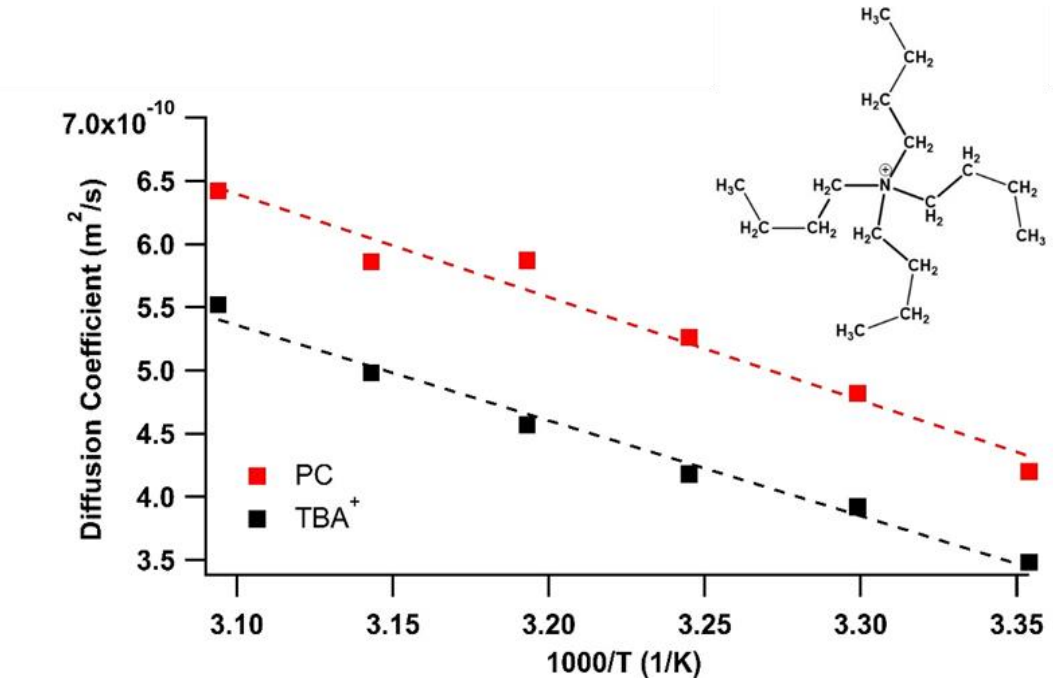

Figure 5. 11 Arrhenius plot of PC and TBA^+ diffusion coefficient within TBA^+ form PFSA equilibrated with PC.

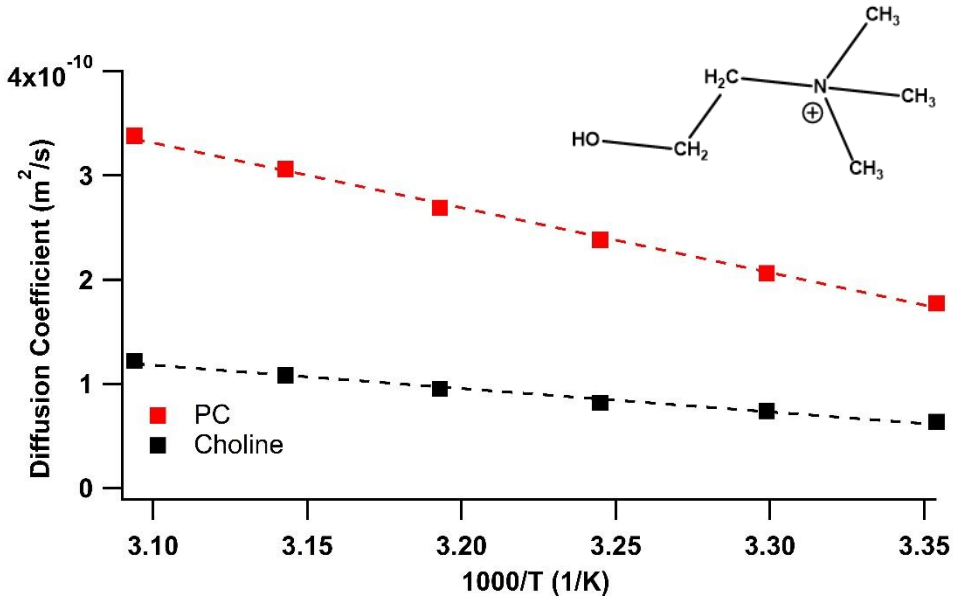

Figure 5. 12 Arrhenius plot of PC and Choline diffusion coefficient within Choline form PFSA equilibrated with PC.

We have seen the same phenomena in the case of ACN in Chapter 2, i.e., that the TBA^+-form PFSA has the highest conductivity among all cations mentioned in this work. However, more importantly, the activation energy of TBA^+ cation and PC are almost identical. We would only expect this kind of behavior in TBA^+-containing PC solution where there is no fixed sulfonate group to interact with TBA^+ cation. However, the PC uptake data has already given us some hint regarding this behavior. The amount of PC uptake in a swollen TBA^+ PFSA is large enough to consider the environment within the membrane as a tiny 'free solution' environment where little to no impact from the sulfonate group is available. Thus, the transport in this case is similar to that in a non-ion-exchange membrane such as porous separator. From a flow battery perspective, a huge flux of solvent molecules, together with redox species, can pass through the membrane and result in unwanted crossover. In the next chapter, more detailed discussion will be provided regarding this topic.

5.4 CONCLUSION

In this chapter, we designed NMR methods tailored for PFSA investigation in ACN and PC based on relaxation and diffusion techniques. The solvation information within the membrane was covered in Chapter 2 and Chapter 3 based on vibrational signal. However, interaction between organic tetraalkylammonium cations and ACN was not visible in FTIR even beyond cation solvation limit in solution (Chapter 3). This has encouraged the exploration of other analytical methods to reveal this important information. A novel experiment design based on Intermolecular dipole-dipole relaxation mechanism was proposed and concentration-dependent relaxation behavior was

presented. The second part of the chapter took advantage of the volatile nature of ACN and used a novel experimental design to enable measurement of ACN diffusion coefficients and corresponding ACN content. The result showed the trajectory of solvent dynamic towards high uptake level and provided insights that can lead to inform crossover behavior of these membranes in a flow battery setup.

The same mindset was also used in the experiment design in the following part where membranes were equilibrated with PC. The non-volatile solvent provided an opportunity to carry out a variable temperature diffusion experiment. The resulting relative diffusion behavior of cation and solvent (PC) provided an indication of cation-sulfonate group interaction information from a transport perspective. Extremely high diffusion was observed in TBA^+ form membrane and this can be related to its high solvent uptake. The observations in this part can also be linked to membrane crossover/permeation that will be discussed in Chapter 6.

CHAPTER 6 IMPROVING PFSA SELECTIVITY BY SEPARATING CONDUCTION AND SWELLING MECHANISM

6.1 INTRODUCTION

From aqueous to non-aqueous redox flow battery, the desired membrane properties are unchanged: electronically isolating anolyte and catholyte and allowing conductance through the membrane to keep electroneutrality. The translation of the sentence above into a flow battery point of view is low areal-specific ohmic resistance (ASR) and low crossover-deteriorated coulombic efficiency[146]. The performance of the membrane is also tightly connected to the cost[20]. A thinner membrane significantly lowers the cost and bolsters the electrical performance only if crossover issue can be solved[147]. So far, crossover-induced capacity fade remains one of the most challenging problems for non-aqueous flow battery[7,148].

Existing membranes for non-aqueous flow batteries inherit the natural disadvantage of non-hydrogen-bonding transport compared to all-vanadium redox systems, leaving the door wide open for redox species to pass through. Efforts have been made to address the issue by developing materials such as composite membranes[149,150], crosslinking[151,152] and size exclusion membranes[153–159]. The ideas behind synthesis of composite or crosslinked membrane are similar as they both seek to alleviate swelling by introducing 'filler' through chemical/physical methods. Size-exclusion is an intriguing approach. Generally, the approach can be categorized into a) pairing ultra large redox molecules or even polymerized redox species with regular separators or b) engineering membranes that specifically have small pore size. Size mismatch is the core idea behind both

approaches. However, transport and solubility issues arise simultaneously in the first case and cost associated with complicated membrane engineering almost renders its application to large-scale energy storage unlikely. More importantly, although the crossover issue has been acknowledged in many published works, the fundamentals of crossover issues have barely been addressed. In this chapter, the solvent-mediated crossover of redox species through PFSA in ACN will be presented from a fundamental perspective. This understanding is crucially necessary to shed light on membrane design exclusive for non-aqueous flow batteries and is the building block of the membrane strategy proposed in this chapter.

Before jumping into membranes for non-aqueous redox flow battery, Figure 6.1 provides a good overview of membrane development for aqueous vanadium flow battery. While the desired properties are low vanadium permeability and high proton conductivity, or high selectivity, which can be represented by the bottom-right region, almost all the existing membranes, regardless of polymer chemistry, all fall into a single trend curve. The trend is a good description of trade-off between conductivity and permeability. While conductivity is uptake dependent, permeability seems to follow the mechanism. Thus, the selectivity has always been an issue[160].

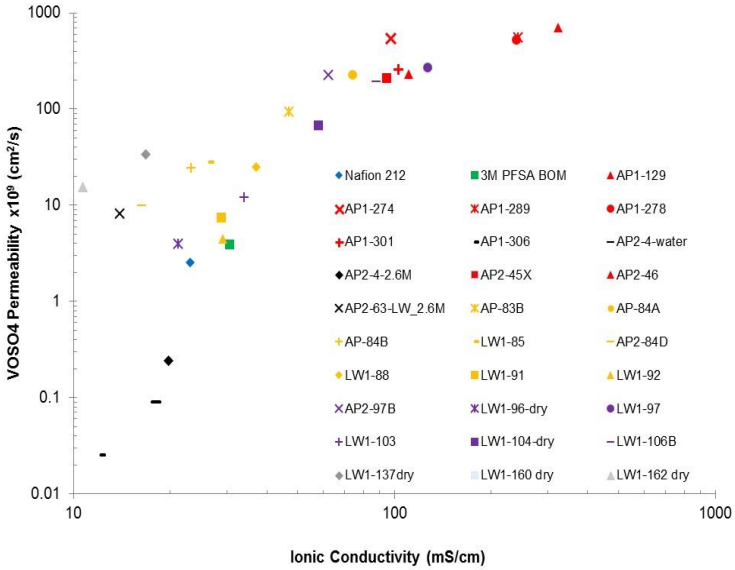

Figure 6. 1 $VOSO_4$ permeability versus ionic conductivity in aqueous system (Mike Perry, UTC)

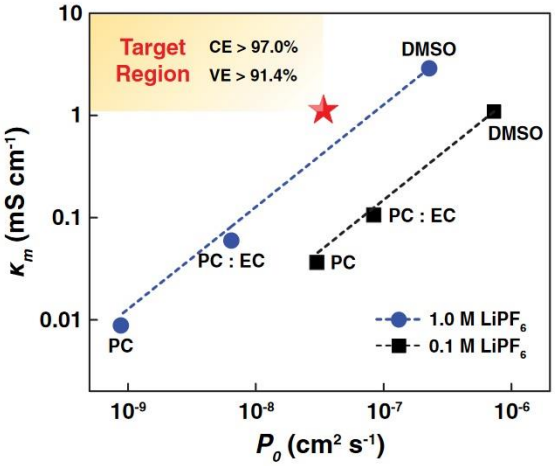

Figure 6. 2 Ferrocene permeability versus lithium ionic conductivity in different solvents of a Nafion 117 membrane [45].

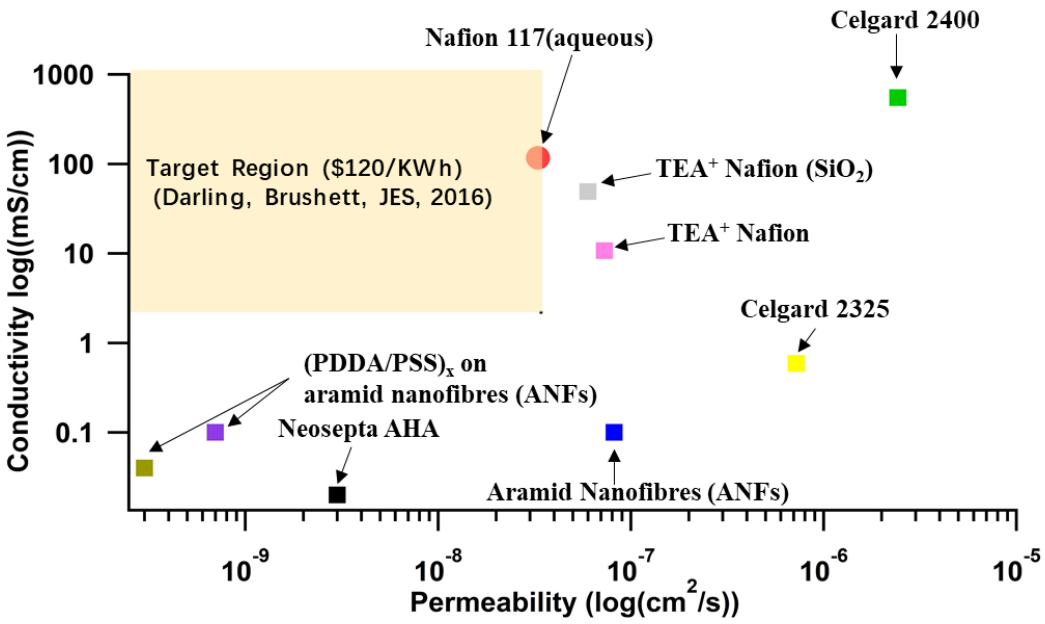

Figure 6. 3 Selected membrane conductivity versus $V(acac)_3$ permeability in ACN[27,29,157,161]

Unfortunately, the selectivity issue is probably worse in non-aqueous systems. We discussed the conductivity perspective in Chapter 2. In terms of crossover, there has been little coverage of this topic.

Figure 6.2 presents the selectivity of Li^+ Nafion 117 in different solvents with ferrocene as active material from a very informative work where a specific selectivity target for non-aqueous flow battery is proposed as well[45]. An ASR under 2.3 Ωcm^2 and crossover current less than 1% of discharge current are desirable to enable non-aqueous flow battery[20]. However, none of the results shown in Figure 6.2 fall into the highlighted target area that the authors deemed to be economically feasible to deploy non-aqueous flow battery. Interestingly, data points in Figure 6.2 follow a similar trade-off pattern as the aqueous system in Figure 6.1.

Apart from ferrocene, Vanadium(III) acetylacetonate ($V(acac)_3$) is the most studied redox couple so far in non-aqueous flow battery[26,47,162,163] and is actually selected as the model redox material in this work. Another reason behind this choice is that the advantage of 'all-vanadium' or symmetric redox system is the obvious receipt for success for aqueous all-vanadium redox flow battery. This strategy is very valuable to current development of non-aqueous flow batteries where the crossover issue is a huge threat. Thus, it is necessary to summarize the membrane performance in $V(acac)_3$ system. In Figure 6.3. conductivity and permeability in $V(acac)_3$/ACN system are shown for selected membranes. Nafion 117 in aqueous vanadium system was also included to give a comparison. Its performance satisfies the threshold and tops all other membranes in the

non-aqueous system. Note that Nafion was average in the aqueous system in terms of selectivity (Figure 6.1). Although some of the results summarized here involved supporting electrolyte, we believe it would only improve the membrane permeability as shown in Figure 6.2 and does not invalidate the point we make in this work.

Celgard (yellow and green, Figure 6.3) is a typical porous membrane used in non-aqueous solvents (lithium-ion battery). It shows good conductivity but very poor permeability because it lacks ion selectivity. In Chapter 5, we have demonstrated the diffusion pattern of PC within TBA^+ PFSA. Celgard shares a very similar mechanism in that ion-selectivity is almost nonexistent. On the other side of the map, nanofiber membranes show low permeability since the porosity is engineered to block active species[157]. However, as explained before, the pathway for solvent to mobilize the cation would also be limited, resulting in low conductivity. TEA^+ form Nafion, which is a benchmark membrane in non-aqueous systems so far, fell between porous membranes and nanofiber membranes. It does have ion-selectivity based on the diffusion pattern presented in Chapter 5; however, its ACN uptake is a lot higher than for Li^+ (Chapter 2).

The similar trend once again is observed in Figure 6.3 among membranes of totally different chemistry. The trade-off pattern is clear: tweaking conditions like solvent or salt concentration is not enough to fundamentally improve membrane selectivity. A true fundamental breakthrough is definitely needed. In Figure 6.2, of two parameters, conductivity poses a more severe problem and permeability under PC and PC/EC was respectable. We have already explained the reason behind the low ionic conductivity of

Li^+ PFSA in Chapter 2. However, the decent permeability of Li^+ form membrane is worth the attention and we have shown that Li^+ form PFSA has relatively low solvent uptake.

We have reported that tetraalkylammonium cations outperform Li^+ in ACN swollen membrane in terms of ionic conductivity due to an advantage in dissociation. However, a large volume of swelling is observed in our study and this is confirmed by the literature. In fact, our previous vibrational data in Chapter 4 suggested that only a small portion of the organic solvent in the membrane participates in the solvation of cations, leaving a substantial portion of the solvent molecules as potential carriers to dissolve and transport redox species across the membrane. In Chapter 5, we projected that the diffusion of ACN within the membrane can be very rapid at high uptake level. This is an extremely important phenomenon in a non-aqueous flow battery because diffusive transport is very likely the dominating mechanism due to low current density compared to vanadium aqueous system where migrative behavior takes over at relatively high current density[164]. Several types of organic-inorganic composite membranes based on a semi-interpenetrating polymer network were fabricated to investigate the relationship between porosity of membrane and current density/permeability in a $V(acac)_3$ non-aqueous flow battery[165]. The result showed that the high porosity enables the flow battery to be operated at a higher current density but at the cost of cross-contamination of redox species due to crossover. A theoretical model study on the effect of $V(acac)_3$, $[V(acac)]^+$, $[V(acac)]^-$ crossover indicated that the diffusion coefficient and proportion of all active species are both important factors regarding capacity fade[166].

Thus, a strategy was developed based on our previous findings, driven by the following question: Is there a way to capitalize on facile dissociation from sulfonate group, as for tetraalkylammonium, and low solvent uptake, as for Li^+ form membranes, at the same time? We thus propose in this work that asymmetric organic cations serve as charge carrier in PFSA. Trimethylbenzylammonium ($TMBA^+$) and Choline were selected.

6.2 EXPERIMENT AND METHODS

6.2.1 Membrane pre-treatment, conductivity, diffusion and uptake measurement

The membrane pre-treatment method followed same methods reported in previous chapters. Generally. membranes were treated at 85°C for an hour in 3% hydrogen peroxide, DI, 1M sulfuric acid and DI again to get rid of extra acid. Membranes were exchanged to tetraethylammonium (TEA^+), Trimethylbenzylammonium ($TMBA^+$) and Choline form by being soaked into respective hydroxide solutions (1 M). The ion exchange efficiency was confirmed by NMR and ICP in our previous work was > 98%[50]. Membranes were then dried over phosphorus pentoxide (P_2O_5) for at least 14 days prior to experiments. Membrane resistance was measured with a typical four-point Teflon conductivity cell soaked in ACN with a Bio-logic SP200 potentiostat from 200 KHz to 1 HZ in the Argon-filled glove box. The high frequency intercept of the Nyquist plot was taken to calculate the ionic conductivity based on Equation 2.1. For NMR diffusion, a dry membrane (> 50 mg) was inserted into a 5 mm NMR tube in the glove box. Deuterated ACN was added to ensure membranes were covered and soaked. A Varian 500 NMR spectrometer with a 60 G/cm gradient coil was the instrument used. DOSY bipolar pulse pair stimulated echo pulse sequence was selected to measure the ^1H diffusion coefficient

of organic cations. The pulse-field-gradient (PFG) measurement of molecular translational motion involves two gradient pulses, as described above. The first one dephases the magnetization, followed by a delay Δ, then the magnetization is refocused. The data is fit exponentially to the Stejskal-Tanner equation[52,53] to derive D, the diffusion coefficient. Figure 6.4 shows the raw data of a diffusion experiment of $TMBA^+$ form PFSA. For ACN uptake, a dry membrane was weighed in the glove box and then soaked in ACN for at least three days. The equilibrated membrane was taken out of the ACN solution, quickly blotted and weighed. ACN uptake, λ, is defined as molecular ratio of ACN to cation within the membrane.

$$\lambda = \frac{(m_{wet} - m_{dry}) \times \mathrm{EW}}{m_{dry} \times \mathrm{M}_{ACN}} \tag{6.1}$$

$$\mathrm{EW} = 825 - \mathrm{M}_{\mathrm{H}} + \mathrm{M}_{Cation} \tag{6.2}$$

6.2.2 Crossover measurement

An in-house designed glass crossover cell (Figure 6.6) (manufactured through PermGear) is the core of a standard crossover experiment. The cell consists of two symmetric compartments (10 mL). A membrane was sandwiched and clamped between two compartments of the glass cell. The two sides were internally connected to maintain the same pressure above solution. $V(acac)_3$ solution and pure ACN were loaded into each side to start the experiment. Both sides of the cell were continuously stirred to eliminate concentration gradients within the compartments while maintaining a constant gradient across the membrane. The setup was all put into a glove box to avoid side-reaction by oxygen and moisture.

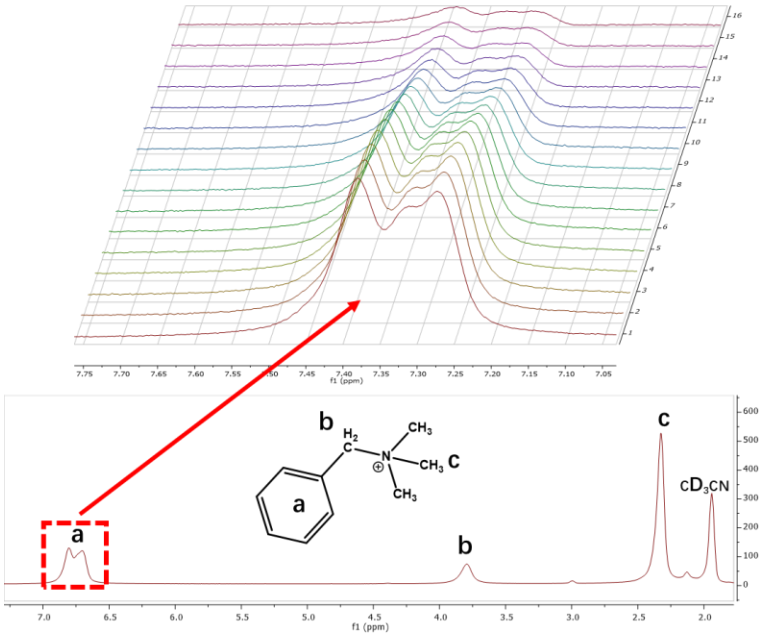

Figure 6. 4 ^{1}H NMR (bottom) and diffusion NMR (top) of $TMBA^{+}$ form PFSA. The diffusion was calculated based on proton signal from aromatic ring of the cation.

The crossover was measured by UV-Vis. Small aliquots of solution of receiving side were sampled to determine the $V(acac)_3$ concentration at given time. The permeability (P_0, cm^2/s) was calculated by the following equation[45]:

$$P_0 = \frac{v\alpha}{-2At} \ln [1 - 2x_{R(t)}] \quad (6.3)$$

Where α is membrane thickness, v is the volume of each side, A is the area of orifice (15mm), t is time (s) and $x_{R(t)}$ is the measured concentration at the receiving side at a given time normalized by the initial concentration at the giving side (0.1M).

An advanced *in situ* crossover experiment (Figure 6.5) was designed to improve accuracy of permeability experiments. The dramatic improvement from proposed asymmetric cation also requires measurements of better resolution. Each compartment was designed to have three ports. On each side, two ports were connected to a peristaltic pump with tubing to form a loop for solution cycling. At the receiving side, a UV-Vis cuvette with flow-through capability was inserted to enable *in situ* measurement.

6.3 RESULTS AND DISCUSSION

6.3.1 Crossover

The purpose of the crossover experiment is to properly measure membrane permeability (of the redox molecule) that is exclusively resulting from a concentration gradient. From a practical perspective, many non-aqueous solvents such as ACN have very high vapor pressure in ambient environment compared to water. This phenomenon naturally creates a situation in typical crossover measurements where the vapor pressure

of either concentration-rich or receiving side can be significantly different not only from each other but also from different time due to change in concentration. Our setup as shown in the Figure 6.5 has the headspaces of the two sides internally connected so that concentration gradient can be separated to be the sole crossover driver. The UV-Vis measurement of $V(acac)_3$ in the receiving compartment over time is shown in Figure 6.6. Images of the cells when the experiments were ended are also included. The crossover experiment of TEA^+ form membrane ended in 5 hours because the concentration in the receiving compartment was almost the same as concentration-rich compartment. The comparison of receiving compartment color is also a good indicator of permeability among PFSA of three cations. Compared to TEA^+ form, Choline and $TMBA^+$ form membranes have very low $V(acac)_3$ crossover. The conductivity and permeability ($V(acac)_3$) data of TEA^+, $TMBA^+$ and Choline form PFSA are plotted in Figure 6.7. Data from literatures in Figure 6.3 are also presented. It is exciting that both Choline and $TMBA^+$ have hit the techno-economic target from a membrane perspective and Choline has demonstrated even lower permeability. TEA^+ form PFSA shows a similar conductivity but its permeability is not satisfactory. The PFSA used in this work is made by 3M and we can see that its competitor Nafion (DuPont) of TEA^+ behaves similarly. The role of supporting electrolyte in terms of redox molecule permeability has been well documented in aqueous vanadium flow battery[167]. Similar to its aqueous counterpart, supporting electrolyte concentration also impacts membrane permeability in non-aqueous system as shown in Figure 6.2. However, we do not have a consensus formula or concentration range for non-aqueous supporting electrolyte yet. We measured the crossover without addition of supporting

electrolyte in order to describe the crossover behavior as simply as possible. In fact, the permeability of both $TMBA^+$ and Choline form PFSA are expected to be even lower in a battery electrolyte. While we were able to dramatically suppress the crossover of $V(acac)_3$, the relatively high ionic conductivity was largely retained. We will discuss detailed preparties of $TMBA^+$ and Choline form PFSA in this next part to explain the improved selectivity.

6.3.2 Asymmetric Cation

Choline and $TMBA^+$ are both derivatives of TMA^+ (Figure 6.6) as one of the hydrocarbon chains is replaced by another moiety to break the overall symmetry of TMA^+. They were chosen as representative asymmetric cations as their hydroxide form are commercially available. While the number of asymmetric cations can be unlimited beyond creativity, the corresponding cost has to be considered[20]. Choline is an extremely cheap cation that has been studied extensively in biochemistry[168]. It is also one of the most popular cations in deep eutectic solvent studies[169,170]. $TMAB^+$ has a similar pricing compared to other tetraalkylammonium salts. The measured ionic conductivity and diffusion coefficient by NMR of $TMBA^+$ and Choline form PFSA are compared with tetraalkylammonium form presented in Chapter 2 in Table 2.1. As mentioned above, the ionic conductivity and diffusion coefficient of the two asymmetric cation membrane are in the same ballpark of other organic cations. We have learned from Chapter 2 that the relatively high conductivity from tetraalkylammonium cation originates from their loose association from sulfonate group. Thus, it is worthwhile to revisit the FTIR work in Chapter 2 and map $TMBA^+$ and Choline form membrane for the same purpose.

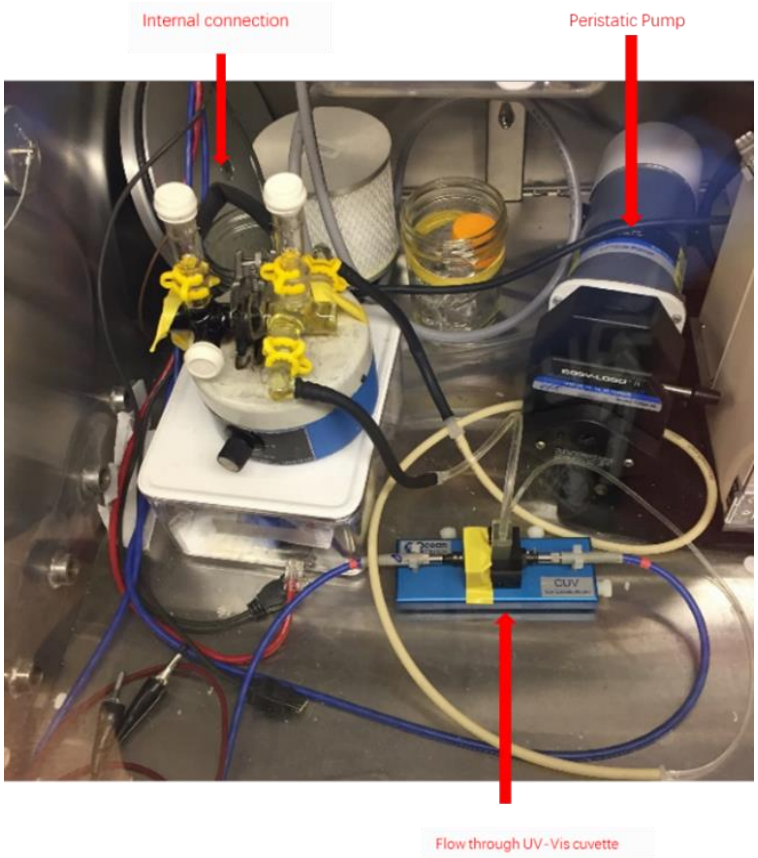

Figure 6. 5 Image of *in-situ* crossover experiment in glove box.

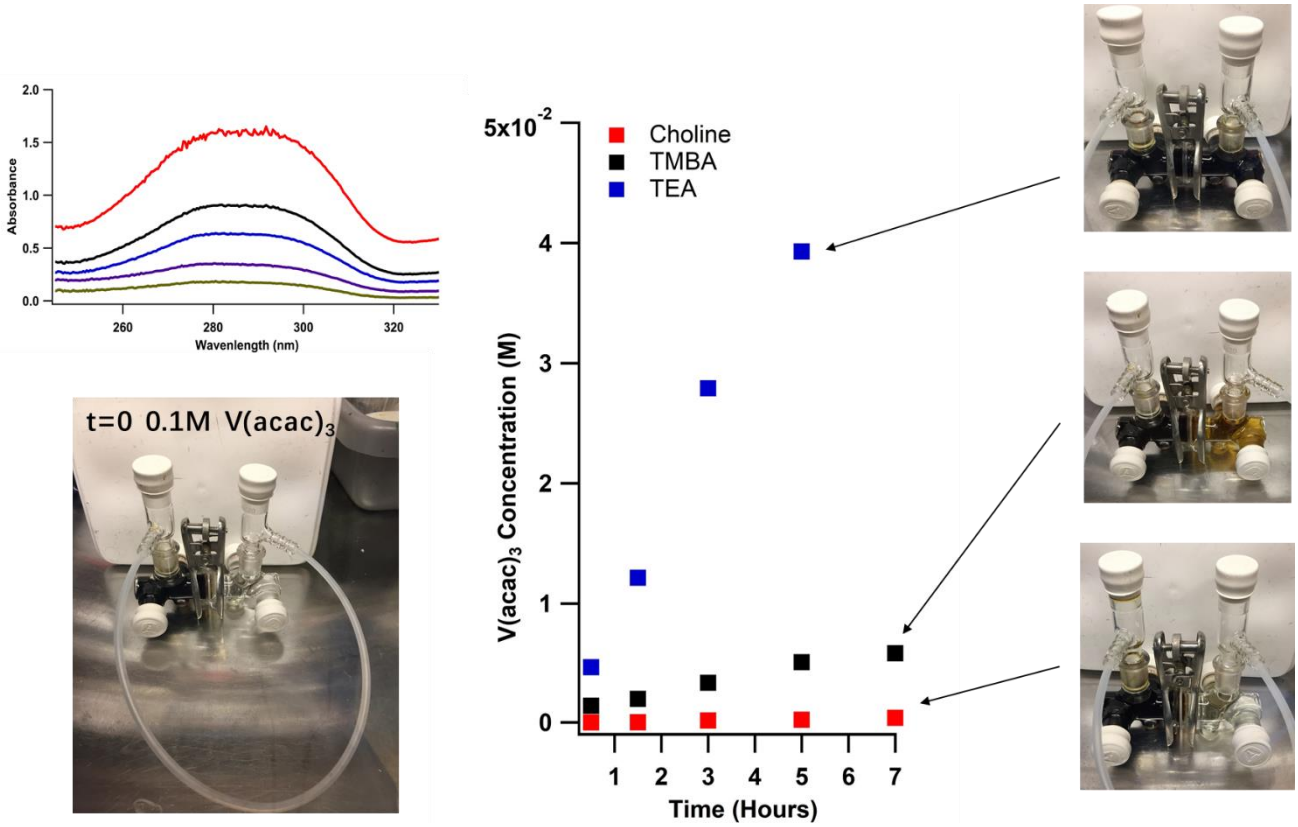

Figure 6. 6 UV-vis data of $V(acac)_3$ over time (top left). Image of crossover setup and starting point of the experiment (bottom left). The receiving side concentration measured by UV-Vis is plotted versus time (right) with corresponding images at the end of experiments.

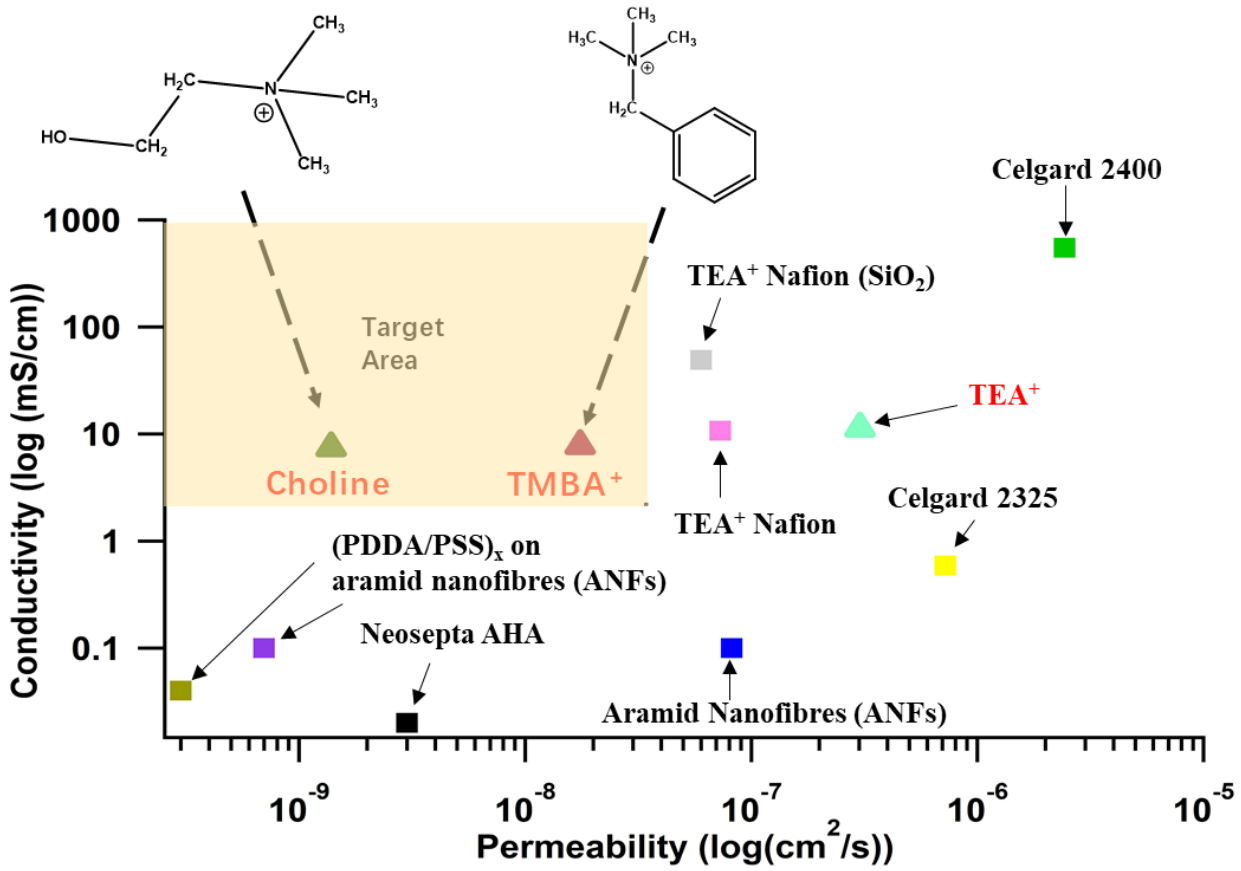

Figure 6. 7 Choline (green, triangle), $TMBA^+$ (red, triangle) and TEA^+ (blue, triangle) form PFSA selectivity ($V(acac)_3$) compared with selected membranes in Figure 6.3[27,29,157,161]

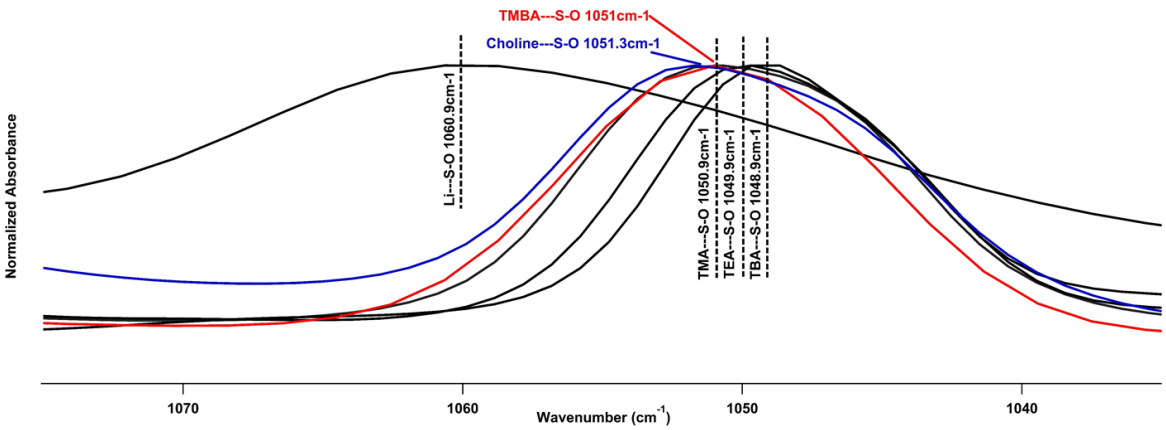

Figure 6. 8 FTIR spectrum of S-O stretching area of $TMBA^+$ (blue) and Choline (red) form PFSA. Li^+ and tetraalkylammonium form are also included for comparison.

Table 6. 1 Ionic conductivity and diffusion coefficient of $TMBA^+$ and Choline form PFSA in ACN compared with tetraalkylammonium form from Table 2.1.

Cation	Membrane	Ionic Conductivity (mS/cm)	Solvent	Diffusion Coefficient (m^2/S)
H^+	3M Ionomer 825EW	106	H_2O	
$TMBA^+$	3M Ionomer 825EW	**7.83**	ACN	**3.87×10^{-10}**
Choline	3M Ionomer 825EW	**7.47**	ACN	**7.98×10^{-11}**
TMA^+	3M Ionomer 825EW	2.43	ACN	2.38×10^{-11}
TEA^+	3M Ionomer 825EW	11.4	ACN	3.33×10^{-10}
TBA^+	3M Ionomer 825EW	18.1	ACN	3.54×10^{-10}

In Figure 6.8, S-O stretches in $TMBA^+$ and Choline form membrane have similar peak positions as for the tetraalkylammonium form even they both express polarity like Li^+. However, as mentioned above, $TMBA^+$ and Choline share the same low surface charge density with other tetraalkylammonium cations as the N is embedded within the molecular structure, resulting in weak interaction at molecular level. In fact, this phenomenon is expected seen in almost all organic cations. Interestingly, $TMBA^+$ and Choline do shift slightly to higher wavenumber. Thus, although $TMBA^+$ and Choline share similar polarity to Li^+, the electrostatic interaction with sulfonate group remains weak as organic cation. This feature explains the retention of high ionic conductivity. The relationship between conductivity and solvent uptake was established as well in Chapter 2 to elucidate the dynamics within PFSA. The density and uptake were measured for $TMBA^+$ and Choline form dry membrane to be compared to other cations form as shown in Figure 6.9.

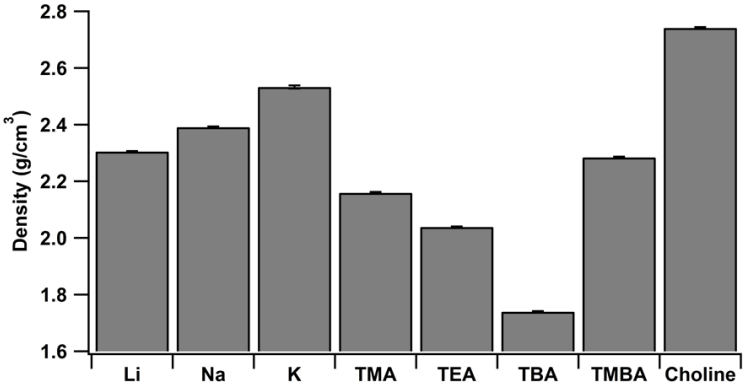

Figure 6. 9 Density of dry membrane incorporated with different cations.

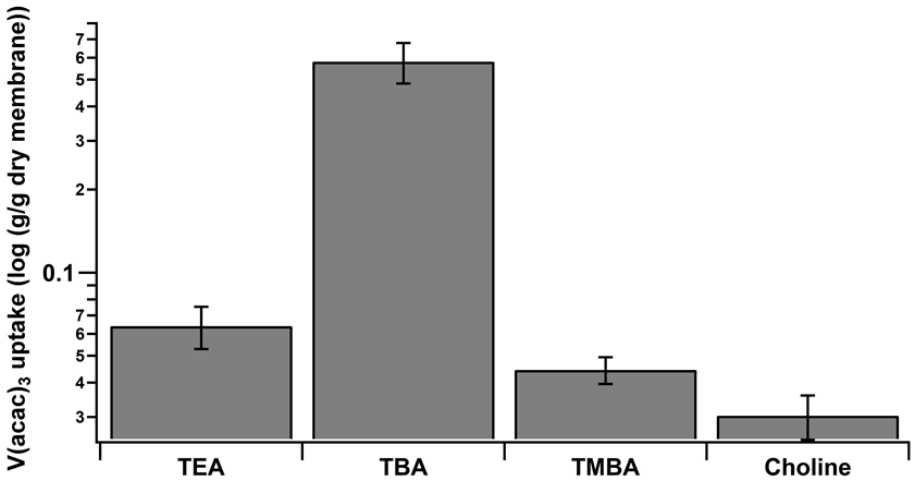

Figure 6. 10 ACN uptake of membranes with incorporated with different cations.

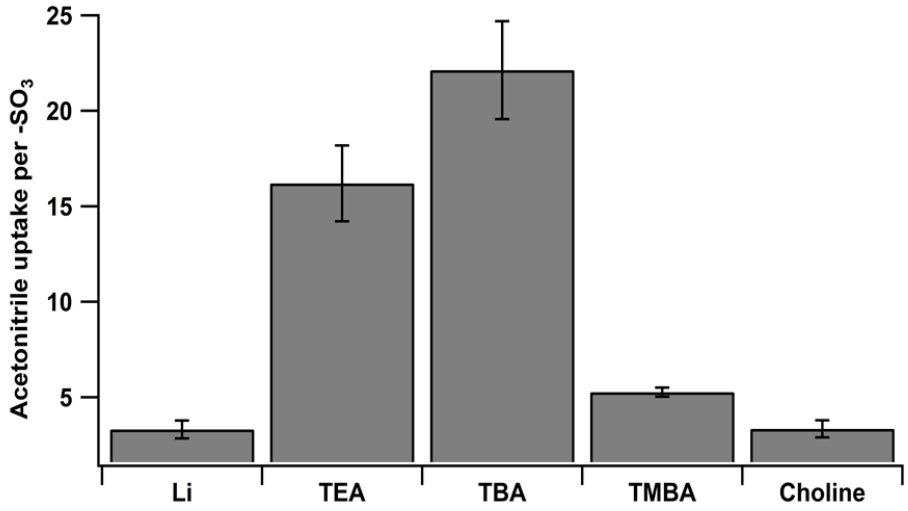

Figure 6. 11 $V(acac)_3$ uptake of membranes with incorporated with different cations in 0.1M $V(acac)_3$ ACN solution.

The cations listed in Figure 6.9 can be categorized into three types: alkali, tetraalkylammonium and asymmetric cations. From Li^+, Na^+ to K^+, the mass of cation goes up, resulting in higher density. We have reported the density pattern of dry tetraalkylammonium form PFSA in Chapter 2. However, the pattern is again overturned in terms of $TMBA^+$ and Choline form. It is interesting to note that the molar mass of TBA^+, $TMBA^+$ and Choline are 242.471g/mol, 167.252g/mol and 104.17g/mol, respectively.

The ACN uptake in Figure 6.10 again behaves reciprocally to the density value in Figure 6.9. Choline form PFSA takes up a similar amount of ACN to that of the Li^+ form. As was discussed beforehand, the density of dry membrane or porosity is an indication of potential uptake amount. However, this 'potential' is not guaranteed and should be discussed case by case. For example, the water uptake and ionic conductivity pattern among tetraalkylammonium form PFSA are the exact opposite of ACN. Combining the density results, it is important to point out that the microstructure change brought about by the cation and the subsequent solvent uptake should be separately discussed. The interesting pattern in dry membrane density is related to the surface charge density of cation. Alkali cations have very high charge density, and the ionic radius is the dominating factor. Tetraalkylammonium cations are bulky species compared to alkali cations. The charge distribution within a bulky cation leads to extremely low surface charge density that to a large extent determines the cation's electrostatic strength. In both Chapter 2 and 3, we have seen the electrostatic interaction of tetraalkylammonium with sulfonate is barely seen in FTIR data. Thus, the resulting ionic domain aggregation leads to morphological change of PFSA compared to alkali form[38,67]. The asymmetric cation

aggregation certainly behaves differently than tetraalkylammonium ones, though being a relatively polar cation,

In terms of ACN uptake, the neutrality of environment within tetraalkylammonium form membrane fully utilizes its low density/high porosity. The uptake of ACN is correlated to the strength of surface charge density. Note that the uptake of water is in reverse order and is due to the increased hydrophobicity from TMA^+ to TBA^+. In the case of asymmetric cations, the reason behind their low ACN uptake is probably due to their 'repulsive' nature of molecular structure. Technically speaking, the so called 'repulsive' nature is a combination of lack of attraction at the opposite side of charge center and dead volume created by their distorted charge distribution.

In Figure 6.11, the corresponding $V(acac)_3$ uptake is presented. The trend of its uptake agrees with ACN uptake shown in Figure 6.10. Thus, we have connected redox material uptake, solvent uptake, and dry membrane density/porosity together to form a rather complete picture of understanding permeability. The proposed asymmetric cation is based on the collection of all observations in this work. We were able to fundamentally break the limitation of conductivity-permeability trade-off by identifying and separating the conducting and swelling mechanism. Settling on choline as a likely component is a product of careful consideration of both fundamentals and bigger picture (the state of flow battery development).

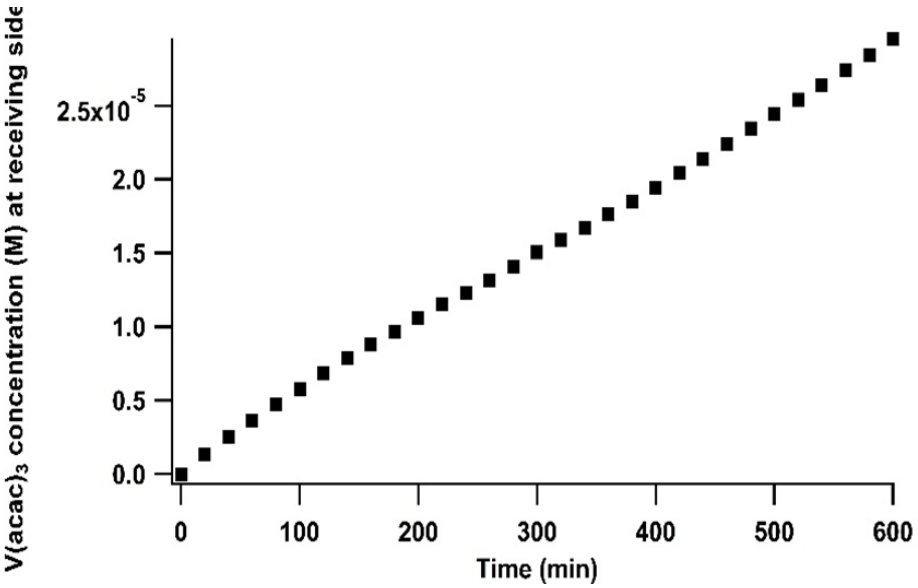

Figure 6. 12 Concentration of $V(acac)_3$ in receiving side of permeability experiment of Choline form PFSA over time. Starting concentration at concentration-rich side is 0.1M.

6.3.3 In-situ Permeation Measurement in Glove Box

To our best knowledge, most existing membranes that have decent ionic conductivity in non-aqueous environment experience significant crossover within 5 hours or less. The superior permeability of proposed asymmetric cation form PFSA also calls for crossover measurements with higher resolution. It is necessary to have more accurate ways of crossover measurement given the time scale. We answered this need by coupling the *in-situ* UV-Vis measurement with typical H-cell configuration in the glove box to give us an upgrade from manually-sampling. This allows us to accurately collect fast responses from any concentration change, especially at an early stage. The setup is shown in the photo in Figure 6.5. In Figure 6.12, a Choline-form PFSA crossover experiment data is illustrated. Compared to the scale of concentration range in Figure 6.6 (~10^{-2} M), the *in-situ* method is a huge upgrade in terms of accuracy and resolution. This setup is also extremely valuable for future study of flow battery operation in a glove box setup.

6.4 CONCLUSION

In this chapter, we reviewed the current membrane selectivity in $V(acac)_3$/ACN system and pointed out the bottleneck of the issue. We addressed the challenge by proposing using an asymmetric cation as charge carrier for PFSA. The proposed idea was a combination of comprehensive understanding of dynamics and interactions within the PFSA as reported in previous chapters. The cost evaluation of non-aqueous flow battery was also taken into consideration. Through crossover experiments, we revealed dramatic improvement in permeability with retention of high conductivity of tetraalkylammonium cation form membrane. Another run of deep analysis of vibrational

information, membrane density, solvent and redox material uptake following the methodology of Chapter explained the superior selectivity of asymmetric cation form PFSA. This chapter demonstrated a true fundamental breakthrough to facilitate membrane performance that has been urgently demanded.

CHAPTER 7 CONCLUSION

This storyline of this work started with the observation of unexpected high ionic conductivity and diffusion of bulky tetraalkylammonium form PFSA compared to the Li^+ form in Chapter 2. The vibrational information of S-O stretching of sulfonate group (membrane) explained the significance of dissociation/association between cation and sulfonate group in cation transport. While the relationship between solvent uptake and conductivity/diffusion remained true in non-aqueous solvents (ACN and PC), some discovered properties were the total opposite of that in the aqueous system. The density of dry membranes with different cation forms suggested the low density/high porosity brought by the bulky tetraalkylammonium cations could lead to high ACN swelling. However, the total opposite swelling behavior in water of tetraalkylammonium form PFSA indicated that it is a case-by-case scenario in terms of PFSA's swelling behavior in a certain solvent. In another word, the interactions among components (cation, solvent and sulfonate group) needs more attention.

This led to the design of a novel experimental design of *in situ* ATR-FTIR coupling with impedance measurement to probe the interactions within PFSA in a non-aqueous environment in Chapter 3. The motivation of the effort was to observe the behavior of ACN molecules and their impact once entering the PFSA, with an emphasis on early-stage uptake/low solvent content. The previous established interaction-based IR analysis was utilized. We were able to capture the evidence of Li^+ dissociation and the simultaneous solvation with ACN. The vibrational information was also accompanied by the real-time impedance measure so that the interactions were connected to the

dynamics. The TEA^+ form PFSA, however, exhibited no clear signal of either association with sulfonate group or solvation with ACN even during the early stage of the experiment when the population of TEA^+ dominated. The corresponding ionic conductivity showed that TEA^+ form PFSA had an order of magnitude higher conductivity than Li^+ form. The dissociation was again highlighted as the dominating factor between two cation form membranes. The naturally weak association between tetraalkylammonium cation and sulfonate group is a favorable advantage thermodynamically.

A revisit to the classic aqueous system was presented in the first part of Chapter 4. The motivation was built on the peak in the plot of conductivity/sulfuric acid concentration. While such a peak was not observable in the water content plot at the same concentration, attention was directed to O-H stretching signal by FTIR. The fitting of O-H stretching region separated the H-bonded and non-H-bonded areas. The subsequent integration of respective area showed that the composition of non-H-bonded O-H band population was a better description of the peak in the conductivity plot. The second part of the chapter investigated the solvation of Li^+ form membrane in PC. The C=O band exhibited a clear solvation signal between Li^+ and PC. The main idea behind this part of study, however, was to correlate the integrated unsolvated PC to the crossover/permeation issue that excess solvent uptake can contribute to unwanted crossover[148].

The interaction regarding tetraalkylammonium cations in previous chapters was kept in the consideration in the following chapter 5. We turned to the NMR relaxation technique to probe the local interaction of tetraalkylammonium cations. Intramolecular dipole-dipole

is a common relaxation mechanism behind relaxation of ^{13}C when protons are attached or in spatial proximity. We tried to extend the mechanism to an intermolecular level to address the local interactions. The experimental feasibility was enabled in a way that the fluorinated PFSA, together with the use of deuterated ACN, yielded a unique environment where the only proton source left was the hydrocarbon protons from the TEA^+ when a TEA^+ form PFSA was interacting with deuterated ACN. While efforts in previous chapters have all but failed to clearly observe the interactions involving tetraalkylammonium cations, the relaxation (T_1) of ^{13}C of C≡N decreased with the increasing population of TEA^+ cations. The TEA^+ concentration-dependency of ^{13}C of C≡N was an indication of spatial proximity between two species (cation and solvent). The second part of Chapter 5 focused on the measurement of solvent diffusion by NMR. The design also adopted an *in-situ* method where ACN was allowed to evaporate within the NMR tube and to be absorbed by dry PFSA seated at the bottom of the tube. The relationship between solvent diffusion and its content within the membrane was plotted. Although this setup also presented a low solvent uptake scenario, the trajectory of ACN transport towards high solvent content among various cations showed that the solvent dynamics can be related to the crossover issue as well. In addition, the diffusion analysis with membrane soaked in PC was also discussed. The non-volatile nature of PC enabled the measurement of diffusion coefficient in a temperature-dependent manner, yielding the activation energy related transport phenomena. Also, the diffusion coefficient of both cation and PC can be effectively separated within the same membrane. The comparison of transport behavior of the cation and PC was an expression of ion-selectivity. The relative diffusion described

the association/dissociation of cation and tortuosity within membrane at the same time. This piece of information provided valuable input regarding the crossover and permeability, which would be covered in the final chapter.

Chapter 6 was a combination of techniques, observations and fundamental understandings in all previous chapters. Asymmetric cations (Choline and $TMBA^+$) were proposed and showed dramatically improved permeability while retaining relatively high ionic conductivity. This was attributed to the successful decoupling of conducting and swelling mechanism by the asymmetric cations. The association of asymmetric cations from sulfonate group was as weak as tetraalkylammonium cations. However, we observed that the density and swelling behavior of asymmetric cation PFSAs were different from the symmetric tetraalkylammonium cation form PFSAs. This was due to the distortion of charge distribution of asymmetric cations. Both Choline and $TMBA^+$ form PFSA showed very low solvent and redox material ($V(acac)_3$) uptake. To improve the accuracy of the permeation experiment, a crossover cell coupled with *in-situ* UV-Vis capability was also designed in the glove box.

LIST OF REFERENCES

1. Dunn, B., Kamath, H. & Tarascon, J.-M. Electrical Energy Storage for the Grid: A Battery of Choices. *Science* **334**, 928–935 (2011).
2. Li, B. & Liu, J. Progress and Directions in Low-cost Redox Flow Batteries for Large-scale Energy Storage. *Natl. Sci. Rev.*
3. Prifti, H., Parasuraman, A., Winardi, S., Lim, T. M. & Skyllas-Kazacos, M. Membranes for Redox Flow Battery Applications. *Membranes* **2**, 275–306 (2012).
4. Li, X., Zhang, H., Mai, Z., Zhang, H. & Vankelecom, I. Ion Exchange Membranes for Vanadium Redox Flow Battery (VRB) Applications. *Energy Environ. Sci.* **4**, 1147–1160 (2011).
5. Winsberg, J., Hagemann, T., Janoschka, T., Hager, M. D. & Schubert, U. S. Redox‐Flow Batteries: From Metals to Organic Redox‐Active Materials. *Angew. Chem. Int. Ed Engl.* **56**, 686–711 (2017).
6. Soloveichik, G. L. Flow Batteries: Current Status and Trends. *Chem. Rev.* **115**, 11533–11558 (2015).
7. Chen, H., Cong, G. & Lu, Y.-C. Recent Progress in Organic Redox Flow Batteries: Active Materials, Electrolytes and Membranes. *J. Energy Chem.* (2018).
8. Kowalski, J. A., Su, L., Milshtein, J. D. & Brushett, F. R. Recent Advances in Molecular Engineering of Redox Active Organic Molecules for Nonaqueous Flow Batteries. *Curr. Opin. Chem. Eng.* **13**, 45–52 (2016).
9. Pan, F. & Wang, Q. Redox Species of Redox Flow Batteries: A Review. *Molecules* **20**, 20499–20517 (2015).

10. Huang, Y., Gu, S., Yan, Y. & Li, S. F. Y. Nonaqueous Redox-flow Batteries: Features, Challenges, and Prospects. *Curr. Opin. Chem. Eng.* **8**, 105–113 (2015).
11. Ponce de Leon, C., Frias-Ferrer, A., Gonzalez-Garcia, J., Szanto, D. A. & Walsh, F. C. Redox Flow Cells for Energy Conversion. *J. Power Sources* **160**, 716–732 (2006).
12. Thaller, L. H. Electrically Rechargeable REDOX Flow Cell. (1976).
13. Fisher, M., Apt, J. & Whitacre, J. F. Can Flow Batteries Scale in the Behind-the-meter Commercial and Industrial Market? A Techno-Economic Comparison of Storage Technologies in California. *J. Power Sources* **420**, 1–8 (2019).
14. Alotto, P., Guarnieri, M. & Moro, F. Redox Flow Batteries for the Storage of Renewable Energy: A Review. *Renew. Sustain. Energy Rev.* **29**, 325–335 (2014).
15. Skyllas-Kazacos, M., Rychick, M. & Robins, R. All-vanadium Redox Battery. (1988).
16. Fisher, S. L. Non-Aqueous Redox Flow Batteries: Active Species Stability and Cost Saving Design Concepts. *PhD Thesis* (2017).
17. Escalante García, I. L. Fundamental and Flow Battery Studies for Non-Aqueous Redox Systems. (Case Western Reserve University, 2015).
18. Schwenzer, B. *et al.* Membrane Development for Vanadium Redox Flow Batteries. *ChemSusChem* **4**, 1388–1406 (2011).
19. Perry, M. L. & Weber, A. Z. Advanced Redox-Flow Batteries: A Perspective. *J. Electrochem. Soc.* **163**, A5064–A5067 (2016).

20. Darling, R. M., Gallagher, K. G., Kowalski, J. A., Ha, S. & Brushett, F. R. Pathways to Low-cost Electrochemical Energy Storage: A Comparison of Aqueous and Nonaqueous Flow Batteries. *Energy Environ. Sci.* **7**, 3459–3477 (2014).
21. Odom, S. Preventing Crossover in Redox Flow Batteries through Active Material Oligomerization. *ACS Cent. Sci.* **4**, 140–141 (2018).
22. Liang, Z. *et al.* Screening Membranes and Electrolytes for High Performance Nonaqueous Flow Cells. *Meet. Abstr.* **MA2019-01**, 457–457 (2019).
23. Ruther, R. E. *et al.* Mechanically Robust, Sodium-Ion Conducting Membranes for Nonaqueous Redox Flow Batteries. *ACS Energy Lett.* **3**, 1640–1647 (2018).
24. Doyle, M., Lewittes, M. E., Roelofs, M. G. & Perusich, S. A. Ionic Conductivity of Nonaqueous Solvent-Swollen Ionomer Membranes Based on Fluorosulfonate, Fluorocarboxylate, and Sulfonate Fixed Ion Groups. *J. Phys. Chem. B* **105**, 9387–9394 (2001).
25. Doyle, M., Lewittes, M. E., Roelofs, M. G., Perusich, S. A. & Lowrey, R. E. Relationship Between Ionic Conductivity of Perfluorinated Ionomeric Membranes and Nonaqueous Solvent Properties. *J. Membr. Sci.* **184**, 257–273 (2001).
26. Escalante-García, I. L., Wainright, J. S., Thompson, L. T. & Savinell, R. F. Performance of a Non-Aqueous Vanadium Acetylacetonate Prototype Redox Flow Battery: Examination of Separators and Capacity Decay. *J. Electrochem. Soc.* **162**, A363–A372 (2015).
27. Bamgbopa, M. O. & Almheiri, S. Influence of Solvents on Species Crossover and Capacity Decay in Non-aqueous Vanadium Redox Flow Batteries: Characterization

of Acetonitrile and 1, 3 Dioxolane Solvent Mixture. *J. Power Sources* **342**, 371–381 (2017).

28. Tang, Z. *et al.* Composition and Conductivity of Membranes Equilibrated with Solutions of Sulfuric Acid and Vanadyl Sulfate. *J. Electrochem. Soc.* **160**, F1040–F1047 (2013).
29. Bang, H. S., Kim, D., Hwang, S. S. & Won, J. Surface-modified Porous Membranes with Electrospun Nafion/PVA Fibres for Non-aqueous Redox Flow Battery. *J. Membr. Sci.* **514**, 186–194 (2016).
30. Darling, R. M., Weber, A. Z., Tucker, M. C. & Perry, M. L. The Influence of Electric Field on Crossover in Redox-Flow Batteries. *J. Electrochem. Soc.* **163**, A5014–A5022 (2016).
31. Nemani, V. P. & Smith, K. C. Analysis of Crossover-Induced Capacity Fade in Redox Flow Batteries with Non-Selective Separators. *J. Electrochem. Soc.* **165**, A3144–A3155 (2018).
32. Cappillino, P. J. *et al.* Application of Redox Non-Innocent Ligands to Non-Aqueous Flow Battery Electrolytes. *Adv. Energy Mater.* **4**, 1300566 (2014).
33. Kim, H. *et al.* Increase of Both Solubility and Working Voltge by Acetyl Substitution on Ferrocene for Non-aqueous Flow Battery. *Electrochem. Commun.* **69**, 72–75 (2016).
34. Sun, C.-N., Mench, M. M. & Zawodzinski, T. A. High Performance Redox Flow Batteries: An Analysis of the Upper Performance Limits of Flow Batteries Using Non-aqueous Solvents. *Electrochimica Acta* **237**, 199–206 (2017).

35. Tang, Z. *et al.* Proton Exchange Membrane Performance Characterization in VRFB. *ECS Trans.* **41**, 25–34 (2012).
36. Kusoglu, A. & Weber, A. Z. New Insights into Perfluorinated Sulfonic-Acid Ionomers. *Chem. Rev.* **117**, 987–1104 (2017).
37. Shi, S., Weber, A. Z. & Kusoglu, A. Structure-Transport Relationship Of Perfluorosulfonic-Acid Membranes In Different Cationic Forms. *Electrochimica Acta* **220**, 517–528 (2016).
38. Mauritz, K. A. & Moore, R. B. State of Understanding of Nafion. *Chem. Rev.* **104**, 4535–4586 (2004).
39. Hickner, M. A. Water-mediated Transport in Ion-containing Polymers. *J. Polym. Sci. Part B Polym. Phys.* **50**, 9–20 (2012).
40. Hudak, N. S., Small, L. J., Pratt, H. D. & Anderson, T. M. Through-Plane Conductivities of Membranes for Nonaqueous Redox Flow Batteries. *J. Electrochem. Soc.* **162**, A2188–A2194 (2015).
41. Gong, K., Fang, Q., Gu, S., Li, S. F. Y. & Yan, Y. Nonaqueous Redox-flow Batteries: Organic Solvents, Supporting Electrolytes, and Redox Pairs. *Energy Environ. Sci.* **8**, 3515–3530 (2015).
42. Bamgbopa, M. O., Pour, N., Shao-Horn, Y. & Almheiri, S. Systematic Selection of Solvent Mixtures for Non-aqueous Redox Flow Batteries – Vanadium Acetylacetonate as a Model System. *Electrochimica Acta* **223**, 115–123 (2017).
43. Gebel, G., Aldebert, P. & Pineri, M. Swelling Study of Perfluorosulphonated Ionomer Membranes. *Polymer* **34**, 333–339 (1993).

44. Guglielmi, M., Aldebert, P. & Pineri, M. Ionic conductivity of perfluorinated ionomer solutions and gels. *J. Appl. Electrochem.* **19**, 167–173 (1989).
45. Su, L. *et al.* An Investigation of the Ionic Conductivity and Species Crossover of Lithiated Nafion 117 in Nonaqueous Electrolytes. *J. Electrochem. Soc.* **163**, A5253–A5262 (2016).
46. Young, S. K., Trevino, S. F. & Tan, N. C. B. Small-angle Neutron Scattering Investigation of Structural Changes in Nafion Membranes Induced by Swelling with Various Solvents. *J. Polym. Sci. Part B Polym. Phys.* **40**, 387–400 (2002).
47. Shinkle, A. A., Pomaville, T. J., Sleightholme, A. E. S., Thompson, L. T. & Monroe, C. W. Solvents and Supporting Electrolytes for Vanadium Acetylacetonate Flow Batteries. *J. Power Sources* **248**, 1299–1305 (2014).
48. Sleightholme, A. E. S. *et al.* Non-aqueous Manganese Acetylacetonate Electrolyte for Redox Flow Batteries. *J. Power Sources* **196**, 5742–5745 (2011).
49. Peng, J. & Zawodzinski, T. A. Describing Ion Exchange Membrane-Electrolyte Interactions for High Electrolyte Concentrations Used in Electrochemical Reactors. *J. Membr. Sci.* 117340 (2019).
50. Peng, J., Lou, K., Goenaga, G. & Zawodzinski, T. Transport Properties of Perfluorosulfonate Membranes Ion Exchanged with Cations. *ACS Appl. Mater. Interfaces* **10**, 38418–38430 (2018).
51. Harmon, J. *et al.* Determination of Molecular Self-Diffusion Coefficients Using Pulsed-Field-Gradient NMR: An Experiment for Undergraduate Physical Chemistry Laboratory. *J. Chem. Educ.* **89**, 780–783 (2012).

52. Stejskal, E. O. & Tanner, J. E. Spin Diffusion Measurements: Spin Echoes in the Presence of a Time‐Dependent Field Gradient. *J. Chem. Phys.* **42**, 288–292 (1965).
53. Peng, J. & Zawodzinski, T. A. Ion Transport in Phase-separated Single Ion Conductors. *J. Membr. Sci.* **555**, 38–44 (2018).
54. Sanders, E. H. *et al.* Characterization of Electrosprayed Nafion Films. *J. Power Sources* **129**, 55–61 (2004).
55. Zawodzinski, T. A. *et al.* Water Uptake by and Transport Through Nafion® 117 Membranes. *J. Electrochem. Soc.* **140**, 1041–1047 (1993).
56. Ochi, S., Kamishima, O., Mizusaki, J. & Kawamura, J. Investigation of Proton Diffusion in Nafion®117 Membrane by Electrical Conductivity and NMR. *Solid State Ion.* **180**, 580–584 (2009).
57. Ue, M. Mobility and Ionic Association of Lithium and Quaternary Ammonium Salts in Propylene Carbonate and γ‐Butyrolactone. *J. Electrochem. Soc.* **141**, 3336 (1994).
58. Zawodzinski, T. A., Neeman, M., Sillerud, L. O. & Gottesfeld, S. Determination of Water Diffusion Coefficients in Perfluorosulfonate Ionomeric Membranes. *J. Phys. Chem.* **95**, 6040–6044 (1991).
59. Bagno, A., Rastrelli, F. & Saielli, G. NMR Techniques for the Investigation of Solvation Phenomena and Non-covalent Interactions. *Prog. Nucl. Magn. Reson. Spectrosc.* **47**, 41–93 (2005).

60. Lowry, S. R. & Mauritz, K. A. An investigation of ionic hydration effects in perfluorosulfonate ionomers by Fourier transform infrared spectroscopy. *J. Am. Chem. Soc.* **102**, 4665–4667 (1980).
61. Cable, K. M., Mauritz, K. A. & Moore, R. B. Effects of Hydrophilic and Hydrophobic Counterions on the Coulombic Interactions in Perfluorosulfonate Ionomers. *J. Polym. Sci. Part B Polym. Phys.* **33**, 1065–1072 (1995).
62. Barthel, J., Buchner, R. & Wismeth, E. FTIR Spectroscopy of Ion Solvation of LiClO4 and LiSCN in Acetonitrile, Benzonitrile, and Propylene Carbonate. *J. Solut. Chem.* **29**, 937–954 (2000).
63. Barthel, J. & Deser, R. FTIR Study of Ion Solvation and Ion-pair Formation in Alkaline and Alkaline Earth Metal Salt Solutions in Acetonitrile. *J. Solut. Chem.* **23**, 1133–1146 (1994).
64. Mollner, A. K. *et al.* Ion−Solvent Interactions in Acetonitrile Solutions of Lithium Iodide and Tetrabutylammonium Iodide. *J. Phys. Chem. A* **108**, 3344–3349 (2004).
65. Loring, J. S. & Fawcett, W. R. Ion−Solvent Interactions in Acetonitrile Solutions of Lithium, Sodium, and Tetraethylammonium Perchlorate Using Attenuated Total Reflectance FTIR Spectroscopy. *J. Phys. Chem. A* **103**, 3608–3617 (1999).
66. Moore, R. B., Cable, K. M. & Croley, T. L. Barriers to Flow in Semicrystalline Ionomers. A procedure for Preparing Melt-processed Perfluorosulfonate Ionomer Films and Membranes. *J. Membr. Sci.* **75**, 7–14 (1992).

67. Page, K. A., Landis, F. A., Phillips, A. K. & Moore, R. B. SAXS Analysis of the Thermal Relaxation of Anisotropic Morphologies in Oriented Nafion Membranes. *Macromolecules* **39**, 3939–3946 (2006).
68. Rubatat, L. & Diat, O. Stretching Effect on Nafion Fibrillar Nanostructure. *Macromolecules* **40**, 9455–9462 (2007).
69. Osborn, S. J. Morphological and Mechanical Properties of Dispersion-Cast and Extruded Nafion Membranes Subjected to Thermal and Chemical Treatments. (2009).
70. Mochizuki, T. *et al.* Temperature- and Humidity-Controlled SAXS Analysis of Proton-Conductive Ionomer Membranes for Fuel Cells. *ChemSusChem* **7**, 729–733 (2014).
71. Jalani, N. H. & Datta, R. The Effect of Equivalent Weight, Temperature, Cationic Forms, Sorbates, and Nanoinorganic Aditives on the Sorption Behavior of Nafion®. *J. Membr. Sci.* **264**, 167–175 (2005).
72. Paddison, S. J. & Zawodzinski Jr, T. A. Molecular Modeling of the Pendant Chain in Nafion®. *Solid State Ion.* **113–115**, 333–340 (1998).
73. Ito, H., Maeda, T., Nakano, A. & Takenaka, H. Properties of Nafion Membranes under PEM Water Electrolysis Conditions. *Int. J. Hydrog. Energy* **36**, 10527–10540 (2011).
74. Hsu, W. Y. & Gierke, T. D. Ion Transport and Clustering in Nafion Perfluorinated Membranes. *J. Membr. Sci.* **13**, 307–326 (1983).

75. Gierke, T. D., Munn, G. E. & Wilson, F. C. The Morphology in Nafion Perfluorinated Membrane Products, as Determined by Wide- and Small-angle X-ray Studies. *J. Polym. Sci. Polym. Phys. Ed.* **19**, 1687–1704 (1981).
76. Lowry, S. R. & Mauritz, K. A. An Investigation of Ionic Hydration Effects in Perfluorosulfonate Ionomers by Fourier Transform Infrared Spectroscopy. *J. Am. Chem. Soc.* **102**, 4665–4667 (1980).
77. Doyle, M., Lewittes, M. E., Roelofs, M. G., Perusich, S. A. & Lowrey, R. E. Relationship Between Ionic Conductivity of Perfluorinated Ionomeric Membranes and Nonaqueous Solvent Properties. *J. Membr. Sci.* **184**, 257–273 (2001).
78. McCormack, P. M., Luo, H., Geise, G. M. & Koenig, G. M. Conductivity, Permeability, and Stability Properties of Chemically Tailored Poly(phenylene oxide) Membranes for Li+ Conductive Non-aqueous Redox Flow Battery Separators. *J. Power Sources* **460**, 228107 (2020).
79. Jia, C. *et al.* High–energy Density Nonaqueous all Redox Flow Lithium Battery Enabled with a Polymeric Membrane. *Sci. Adv.* **1**, e1500886 (2015).
80. O. Bamgbopa, M., Shao-Horn, Y. & Almheiri, S. The Potential of Non-aqueous Redox Flow Batteries as Fast-charging Capable Energy Storage Solutions: Demonstration with an Iron–chromium Acetylacetonate Chemistry. *J. Mater. Chem. A* **5**, 13457–13468 (2017).
81. Hallinan, D. T. & Elabd, Y. A. Diffusion and Sorption of Methanol and Water in Nafion Using Time-Resolved Fourier Transform Infrared−Attenuated Total Reflectance Spectroscopy. *J. Phys. Chem. B* **111**, 13221–13230 (2007).

82. Hallinan, D. T. & Elabd, Y. A. Diffusion of Water in Nafion Using Time-Resolved Fourier Transform Infrared−Attenuated Total Reflectance Spectroscopy. *J. Phys. Chem. B* **113**, 4257–4266 (2009).
83. Kunimatsu, K., Bae, B., Miyatake, K., Uchida, H. & Watanabe, M. ATR-FTIR Study of Water in Nafion Membrane Combined with Proton Conductivity Measurements during Hydration/Dehydration Cycle. *J. Phys. Chem. B* **115**, 4315–4321 (2011).
84. Kunimatsu, K., Yoda, T., Tryk, D. A., Uchida, H. & Watanabe, M. In Situ ATR-FTIR Study of Oxygen Reduction at the Pt/Nafion Interface. *Phys. Chem. Chem. Phys.* **12**, 621–629 (2009).
85. Liang, Z. *et al.* FT-IR study of the microstructure of Nafion® membrane. *J. Membr. Sci.* **233**, 39–44 (2004).
86. Ludvigsson, M., Lindgren, J. & Tegenfeldt, J. FTIR Study of Water in Cast Nafion Films. *Electrochimica Acta* **45**, 2267–2271 (2000).
87. Blanchard, R. M. & Nuzzo, R. G. An Infrared Study of the Effects of Hydration on Cation-loaded Nafion Thin Films. *J. Polym. Sci. Part B Polym. Phys.* **38**, 1512–1520.
88. Quezado, S., Kwak, J. C. T. & Falk, M. An Infrared Study of Water–ion Interactions in Perfluorosulfonate (Nafion) Membranes. *Can. J. Chem.* **62**, 958–966 (1984).
89. Ostrowska, J. & Narebska, A. Infrared Study of Hydration and Association of Functional Groups in a Perfluorinated Nafion Membrane, Part 1. *Colloid Polym. Sci.* **261**, 93–98 (1983).
90. Iwamoto, R., Oguro, K., Sato, M. & Iseki, Y. Water in Perfluorinated Sulfonic Acid Nafion Membranes. *J. Phys. Chem. B* **106**, 6973–6979 (2002).

91. Laporta, M., Pegoraro, M. & Zanderighi, L. Perfluorosulfonated Membrane (Nafion): FT-IR Study of the State of Water with Increasing Humidity. *Phys. Chem. Chem. Phys.* **1**, 4619–4628 (1999).
92. Xie, G., Okada, T. & Arimura, T. Fourier Transform Infrared Spectroscopy Study of Fully Hydrated Nation Membranes of Various Cation Forms. *Z. Für Phys. Chem.* **205**, 113–125 (1998).
93. Fawcett, W. R., Brooksby, P., Verbovy, D., Bakó, I. & Pálinkás, G. Studies of Anion Solvation in Polar Aprotic Solvents. *J. Mol. Liq.* **118**, 171–178 (2005).
94. Danilczuk, M., Lin, L., Schlick, S., Hamrock, S. J. & Schaberg, M. S. Understanding the Fingerprint Region in the Infra-red Spectra of Perfluorinated Ionomer Membranes and Corresponding Model Compounds: Experiments and Theoretical Calculations. *J. Power Sources* **196**, 8216–8224 (2011).
95. Erkabaev, A. M., Yaroslavtseva, T. V., Reznitskikh, O. G. & Bushkova, O. V. Solvation of Anions in Acetonitrile Solutions: FTIR and Quantum Chemical Study for Br−, ClO4−, AsF6−, and CF3SO3−. *Spectrochim. Acta. A. Mol. Biomol. Spectrosc.* **229**, 117873 (2020).
96. Lawton, J. S., Tiano, S. M., Donnelly, D. J., Flanagan, S. P. & Arruda, T. M. The Effect of Sulfuric Acid Concentration on the Physical and Electrochemical Properties of Vanadyl Solutions. *Batteries* **4**, 40 (2018).
97. Tang, Z. *et al.* Characterization of Sulfonated Diels-Alder Poly(phenylene) Membranes for Electrolyte Separators in Vanadium Redox Flow Batteries. *J. Electrochem. Soc.* **161**, A1860–A1868 (2014).

98. Sun, C.-N., Tang, Z., Belcher, C., Zawodzinski, T. A. & Fujimoto, C. Evaluation of Diels–Alder poly(phenylene) anion exchange membranes in all-vanadium redox flow batteries. *Electrochem. Commun.* **43**, 63–66 (2014).

99. Pezeshki, A. M. *et al.* Full Cell Study of Diels Alder Poly(phenylene) Anion and Cation Exchange Membranes in Vanadium Redox Flow Batteries. *J. Electrochem. Soc.* **163**, A5154–A5162 (2016).

100. Lawton, J. S. *et al.* Characterization of Vanadium Ion Uptake in Sulfonated Diels Alder Poly(phenylene) Membranes. *J. Electrochem. Soc.* **163**, A5229–A5235 (2016).

101. Larsen, R. W., Zielke, P. & Suhm, M. A. Hydrogen-bonded OH Stretching Modes of Methanol Clusters: A Combined IR and Raman Isotopomer Study. *J. Chem. Phys.* **126**, 194307 (2007).

102. Rekik, N., Ghalla, H. & Hanna, G. Explaining the Structure of the OH Stretching Band in the IR Spectra of Strongly Hydrogen-Bonded Dimers of Phosphinic Acid and Their Deuterated Analogs in the Gas Phase: A Computational Study. *J. Phys. Chem. A* **116**, 4495–4509 (2012).

103. Cazzanelli, E., Croce, F., Appetecchi, G. B., Benevelli, F. & Mustarelli, P. Li+ Solvation in Ethylene Carbonate–Propylene Carbonate Concentrated Solutions: A Comprehensive Model. *J. Chem. Phys.* **107**, 5740–5747 (1997).

104. Fish, D. & Smid, J. Solvation of Lithium Ions in Mixtures of Tetraethylene Glycol Dimethyl Ether and Propylene Carbonate. *Electrochimica Acta* **37**, 2043–2049 (1992).

105. Matsubara, K., Kaneuchi, R. & Maekita, N. 13 C NMR Estimation of Preferential Solvation of Lithium Ions in Non-aqueous Mixed Solvents. *J. Chem. Soc. Faraday Trans.* **94**, 3601–3605 (1998).

106. Seo, D. M. *et al.* Role of Mixed Solvation and Ion Pairing in the Solution Structure of Lithium Ion Battery Electrolytes. *J. Phys. Chem. C* **119**, 14038–14046 (2015).

107. Volkov, V. I. & Marinin, A. A. NMR Methods for Studying Ion and Molecular Transport in Polymer Electrolytes. *Russ. Chem. Rev.* **82**, 248 (2013).

108. Ando, I. & Webb, G. A. Some Quantum Chemical Aspects of Solvent Effects on NMR Parameters. *Org. Magn. Reson.* **15**, 111–130 (1981).

109. Zhong, G. *et al.* The States of Methanol within Nafion and Sulfonated Poly(phenylene ether ether sulfone) Membranes. *J. Membr. Sci.* **428**, 212–217 (2013).

110. Boros, S., Gáspári, Z. & Batta, G. Chapter One - Accurate NMR Determinations of Proton–Proton Distances. in *Annual Reports on NMR Spectroscopy* (ed. Webb, G. A.) vol. 94 1–39 (Academic Press, 2018).

111. Holz, M. New Developments in NMR of Simple Electrolyte Solutions. *Prog. Nucl. Magn. Reson. Spectrosc.* **18**, 327–403 (1986).

112. Komoroski, R. A. A Multinuclear Fourier Transform NMR Study of Perfluorosulfonate Ionomers. in *Ions in Polymers* vol. 187 155–168 (1980).

113. Komoroski, R. A. & Mauritz, K. A. A Sodium-23 Nuclear Magnetic Resonance Study of Ionic Mobility and Contact Ion Pairing in a Perfluorosulfonate Ionomer. *J. Am. Chem. Soc.* **100**, 7487–7489 (1978).

114. Komoroski, R. A. & Mauritz, K. A. Nuclear Magnetic Resonance Studies and the Theory of Ion Pairing in Perfluorosulfonate Ionomers. in *Perfluorinated Ionomer Membranes* vol. 180 113–138 (1982).

115. Bagno, A., Rastrelli, F. & Scorrano, G. Detecting Intermolecular NOEs by Means of a Novel DPFGSE Pulse Sequence. Application to the Solvation of Carbohydrates in Binary Mixtures. *J. Magn. Reson.* **167**, 31–35 (2004).

116. Kaiser, R. Intermolecular Nuclear Overhauser Effect in Liquid Solutions. *J. Chem. Phys.* **42**, 1838–1839 (1965).

117. Neuhaus, D. & Williamson, M. P. *The Nuclear Overhauser Effect in Structural and Conformational Analysis*. (VCH, 1989).

118. Otting, G., Liepinsh, E. & Wüthrich, K. Polypeptide Hydration in Mixed Solvents at Low Temperatures. in *NMR in Structural Biology* vol. Volume 5 639–641 (WORLD SCIENTIFIC, 1995).

119. Bagno, A. Probing the Solvation Shell of Organic Molecules by Intermolecular 1H NOESY. *J. Phys. Org. Chem.* **15**, 790–795 (2002).

120. Oza, Y. V., MacFarlane, D. R., Forsyth, M. & O'Dell, L. A. Characterisation of Ion Transport in Sulfonate Based Ionomer Systems Containing Lithium and Quaternary Ammonium Cations. *Electrochimica Acta* **175**, 80–86 (2015).

121. Han, J. H. *et al.* 1H Nuclear Magnetic Resonance Study of Hydrated Water Dynamics in Perfluorosulfonic Acid Ionomer Nafion. *Appl. Phys. Lett.* **106**, 023104 (2015).

122. Grüne M. *et al.* 7Li NMR Spin‐Lattice Relaxation and Ionic Diffusion in Lithium Thioborate Glasses. *Berichte Bunsenges. Für Phys. Chem.* **93**, 1313–1317 (2010).

123. Levy, G. C. Carbon-13 spin–lattice Relaxation and Solvation of Organic Ions: N-butylamine and N-butylammonium Ion. *J. Chem. Soc. Chem. Commun.* **0**, 768–769 (1972).

124. Breitmaier, E., Spohn, K.-H. & Berger, S. 13C Spin‐Lattice Relaxation Times and the Mobility of Organic Molecules in Solution. *Angew. Chem. Int. Ed. Engl.* **14**, 144–159 (1975).

125. Bopp, T. T. Magnetic Resonance Studies of Anisotropic Molecular Rotation in Liquid Acetonitrile‐d3. *J. Chem. Phys.* **47**, 3621–3626 (1967).

126. Woessner, D. E., Jr, B. S. S. & Strom, E. T. A Study of Molecular Re-orientation in Liquid Acetonitrile by Nuclear Spin-lattice Relaxation. *Mol. Phys.* **14**, 265–273 (1968).

127. Leipert, T. K., Noggle, J. H. & Gillen, K. T. Carbon-13 Spin-lattice Relaxation in Acetonitrile. *J. Magn. Reson. 1969* **13**, 158–166 (1974).

128. von Goldammer, E., Lüdemann, H. ‐D. & Müller, A. 13C‐spin‐lattice Relaxation Behavior of Acetonitrile and Acetone. *J. Chem. Phys.* **60**, 4590–4594 (1974).

129. Dando, N. R., Dybowski, Cecil. & Gold, H. S. Carbon-13 Nuclear Magnetic Resonance Spectrometric Investigation of Acetonitrile-tetraalkylammonium Salt Interactions. *Anal. Chem.* **54**, 1101–1104 (1982).

130. Dando, N. R., Gold, H. S. & Dyboski, C. Use of Concentration-dependent Relaxation Rates for Carbon-13 Chemical Shift Assignment of Symmetric Tetraalkylammonium Salts in Acetonitrile. *Org. Magn. Reson.* **21**, 467–469 (1983).

131. Sai, T., Sugiura, M., Takao, N. & Fujiwara, H. 13 C Spin-lattice Relaxation Times of Piperidines. Molecular Motions and Interactions with Solvents. *J. Chem. Soc. Perkin Trans. 2* **0**, 523–525 (1989).

132. Singh Gill, D. Evaluation of Solvated Radii of Ions in Non-aqueous Solvents. *Electrochimica Acta* **24**, 701–703 (1979).

133. Everaert, J. & Persoons, A. Dissociation Mechanism of Tetrabutylammonium Picrate Ion Pairs in Media of Low Polarity. 1. A Sphere-in-continuum Approach. *J. Phys. Chem.* **85**, 3930–3937 (1981).

134. Dando, N. R., Gold, H. S. & Dybowski, C. Solute 13C Nuclear Magnetic Resonance Spectrometric Investigation of Acetonitrile-Tetraalkylammonium Salt Interactions: *Appl. Spectrosc.* **37**, 29–31 (1983).

135. Dando, N. R., Dybowski, C. & Gold, H. S. Segmental Motions and Interactions of Symmetric Tetraalkylammonium Salts in Acetonitrile. *J. Phys. Chem.* **87**, 3094–3095 (1983).

136. Masuda, Y. & Muramoto, A. Solvent Effect on Rotational Correlation Times of Symmetric Tetraalkylammonium Ions. *J. Solut. Chem.* **33**, 811–825 (2004).

137. Lang, E. W., Bradl, S., Kunz, W. & Turq, P. NMR Relaxation Study of Tetrapentylammonium Ions in Acetonitrile Solutions. *J. Phys. Chem.* **95**, 10576–10582 (1991).

138. Evans, R., Dal Poggetto, G., Nilsson, M. & Morris, G. A. Improving the Interpretation of Small Molecule Diffusion Coefficients. *Anal. Chem.* **90**, 3987–3994 (2018).

139. Volkov, V. I., Korotchkova, S. A., Ohya, H. & Guo, Q. Self-diffusion of Water-ethanol Mixtures in Polyacrylic Acid-polysulfone Composite Membranes Obtained by Pulsed-field Gradient Nuclear Magnetic Resonance Spectroscopy. *J. Membr. Sci.* **100**, 273–286 (1995).

140. Every, H. A., Hickner, M. A., McGrath, J. E. & Zawodzinski, T. A. An NMR Study of Methanol Diffusion in Polymer Electrolyte Fuel Cell Membranes. *J. Membr. Sci.* **250**, 183–188 (2005).

141. Duan, Q., Ge, S. & Wang, C.-Y. Water uptake, ionic conductivity and swelling properties of anion-exchange membrane. *J. Power Sources* **243**, 773–778 (2013).

142. Sorte, E. G. *et al.* Impact of Hydration and Sulfonation on the Morphology and Ionic Conductivity of Sulfonated Poly(phenylene) Proton Exchange Membranes. *Macromolecules* **52**, 857–876 (2019).

143. Cappadonia, M., Erning, J. W., Niaki, S. M. S. & Stimming, U. Conductance of Nafion 117 Membranes as a Function of Temperature and Water Content. *Solid State Ion.* **77**, 65–69 (1995).

144. Andrada, H. E., Franzoni, M. B., Carreras, A. C. & Chávez, F. V. Dynamics and Spatial Distribution of Water in Nafion 117 Membrane Investigated by NMR Spin-spin Relaxation. *Int. J. Hydrog. Energy* **43**, 8936–8943 (2018).

145. Moumouzias, G. & Ritzoulis, G. Electrolytic Conductances of Tetrabutylammonium Tetraphenylborate in Propylene Carbonate + Acetonitrile Mixtures at (25, 30, and 35) °C. *J. Chem. Eng. Data* **41**, 326–330 (1996).

146. Darling, R., Gallagher, K., Xie, W., Su, L. & Brushett, F. Transport Property Requirements for Flow Battery Separators. *J. Electrochem. Soc.* **163**, A5029–A5040 (2016).

147. Reed, D. *et al.* Performance of Nafion® N115, Nafion® NR-212, and Nafion® NR-211 in a 1 kW Class all Vanadium Mixed Acid Redox Flow Battery. *J. Power Sources* **285**, 425–430 (2015).

148. Small, L. J., Pratt, H. D. & Anderson, T. M. Crossover in Membranes for Aqueous Soluble Organic Redox Flow Batteries. *J. Electrochem. Soc.* **166**, A2536–A2542 (2019).

149. Kim, J.-H. *et al.* Fabrication of a Composite Anion Exchange Membrane with Aligned Ion Channels for a High-performance Non-aqueous Vanadium Redox Flow Battery. *RSC Adv.* **10**, 5010–5025 (2020).

150. Jung, J., Won, J. & Hwang, S. S. Highly Selective Composite Membranes using Ladder-like Structured Polysilsesquioxane for a Non-aqueous Redox Flow Battery. *J. Membr. Sci.* **595**, 117520 (2020).

151. Li, Y. *et al.* Crosslinked Anion Exchange Membranes Prepared from Poly(phenylene oxide) (PPO) for Non-aqueous Redox Flow Batteries. *J. Power Sources* **378**, 338–344 (2018).

152. Kwon, H.-G., Bae, I. & Choi, S.-H. Crosslinked Poly(arylene ether ketone) Membrane with High Anion Conductivity and Selectivity for Non-aqueous Redox Flow Batteries. *J. Membr. Sci.* **620**, 118928 (2021).

153. Iyer, V. A. *et al.* Assessing the Impact of Electrolyte Conductivity and Viscosity on the Reactor Cost and Pressure Drop of Redox-active Polymer Flow Batteries. *J. Power Sources* **361**, 334–344 (2017).

154. Kushner, D. I., Tucker, M. C., Kusoglu, A. & Weber, A. Z. Probing the Size-Exclusion Properties of Redox Flow Battery Separator Membranes Using Metal-Ligand Complexes. *Meet. Abstr.* **MA2018-01**, 195–195 (2018).

155. Hendriks, K. H. *et al.* High-Performance Oligomeric Catholytes for Effective Macromolecular Separation in Nonaqueous Redox Flow Batteries. *ACS Cent. Sci.* **4**, 189–196 (2018).

156. Gigli, M. *et al.* Investigating the Factors that Influence Resistance Rise of PIM-1 Membranes in Nonaqueous Electrolytes. *Electrochem. Commun.* **107**, 106530 (2019).

157. Tung, S. on, Fisher, S. L., Kotov, N. A. & Thompson, L. T. Nanoporous Aramid Nanofibre Separators for Nonaqueous Redox Flow Batteries. *Nat. Commun.* **9**, 4193 (2018).

158. Winsberg, J. *et al.* Poly(boron-dipyrromethene)—A Redox-Active Polymer Class for Polymer Redox-Flow Batteries. *Chem. Mater.* **28**, 3401–3405 (2016).

159. Janoschka, T. *et al.* An Aqueous, Polymer-based Redox-flow Battery Using Non-corrosive, Safe, and Low-cost Materials. *Nature* **527**, 78–81 (2015).

160. Palanisamy, G. *et al.* Tuning the Ion Selectivity and Chemical Stability of a Biocellulose Membrane by PFSA Ionomer Reinforcement for Vanadium Redox Flow Battery Applications. *ACS Sustain. Chem. Eng.* **8**, 2040–2051 (2020).

161. Trogadas, P., Pinot, E. & Fuller, T. F. Composite, Solvent-Casted Nafion Membranes for Vanadium Redox Flow Batteries. *Electrochem. Solid-State Lett.* **15**, A5–A8 (2011).

162. Shinkle, A. A. Non-Aqueous Single-Metal Redox Flow Batteries. (2013).

163. Saraidaridis, J. D., Bartlett, B. M. & Monroe, C. W. Spectroelectrochemistry of Vanadium Acetylacetonate and Chromium Acetylacetonate for Symmetric Nonaqueous Flow Batteries. *J. Electrochem. Soc.* **163**, A1239–A1246 (2016).

164. Gubler, L. Membranes and Separators for Redox Flow Batteries. *Curr. Opin. Electrochem.* **18**, 31–36 (2019).

165. Shin, S.-H., Kim, Y., Yun, S.-H., Maurya, S. & Moon, S.-H. Influence of Membrane Structure on the Operating Current Densities of Non-aqueous Redox Flow Batteries: Organic–inorganic Composite Membranes Based on a Semi-interpenetrating Polymer Network. *J. Power Sources* **296**, 245–254 (2015).

166. Lee, D., Ryu, S., Shin, S.-H., Kim, J.-H. & Moon, S.-H. A Model Study on Effects of Vanadium Ion Diffusion Through Ion Exchange Membranes in a Non-aqueous Redox Flow Battery. *J. Renew. Sustain. Energy* **11**, 034701 (2019).

167. Lawton, J. S., Jones, A. & Zawodzinski, T. Concentration Dependence of VO2+ Crossover of Nafion for Vanadium Redox Flow Batteries. *J. Electrochem. Soc.* **160**, A697–A702 (2013).

168. Lockman, P. R. & Allen, D. D. The Transport of Choline. *Drug Dev. Ind. Pharm.* **28**, 749–771 (2002).

169. Bahadori, L. *et al.* Investigation of Ammonium- and Phosphonium-Based Deep Eutectic Solvents as Electrolytes for a Non-Aqueous All-Vanadium Redox Cell. *J. Electrochem. Soc.* **163**, A632–A638 (2016).

170. Rengstl, D. Choline as a Cation for the Design of Low-toxic and Biocompatible Ionic Liquids, Surfactants, and Deep Eutectic Solvents. (2014).

VITA

Kun Lou graduated from Tongji University, Shanghai, China with a B.E. degree in Materials Science and Engineering. He later earned a M.S. degree in Chemical Engineering from University at Buffalo, the State University of New York. He joined The Bredesen Center for Interdisciplinary Research and Graduate Education, a joint program between the University of Tennessee, Knoxville and Oak Ridge National Laboratory (ORNL), in 2014. He worked in Energy Storage Group of Chemical Science Division under the supervision of Dr. Thomas Zawodzinski.